Event-Based Non-Intrusive Home Current Measurement using Sensor Array

by

Juncheng Wang

A thesis submitted in partial fulfillment of the requirements for the degree of

Master of Science

in

Energy Systems

Department of Electrical and Computer Engineering

University of Alberta

ABSTRACT

Home current measurement provides basic but vital information for advanced home energy monitoring and management, which is a critical enabling technology for smart homes. Accurate and easy-to-implement home current measurement can enable various smart home applications such as non-intrusive load monitoring (NILM), home energy management and demand response management. Current sensing technologies featured by low-cost wide-range current sensors are applied to various industrial applications. Yet, there are still open issues which require extensive research in non-intrusive current measurement using sensor array.

This thesis presents a novel method for non-intrusive home current measurement using an array of magnetic field sensors. It is specifically designed for measuring the real-time currents on three wires, including two hot wires and one neutral wire, enclosed in the electric conduits of North American homes. The key idea is to extract information from appliance state changing events captured by sensor measurement changes. Since each detected event only corresponds to two wires between which the state-changing appliance is connected, the events can be clustered according to the wire connections. Wire position identification is formulated as a nonlinear least square (NLLS) problem and is efficiently solved. Then, real-time current measurement is achieved by using the trans-impedance matrix built based on the solved wire positions and the sensor parameters obtained from the manufacturing process. The proposed method is evaluated by extensive laboratory and field tests.

ACKNOWLEDGEMENTS

Contents

List of Tables

List of Figures

Nomenclature

Set and Dimention

$\mathbb{S}_S, n_s$	Magnetic sensors
$\mathbb{S}_C, n_c$	Wires
$\mathbb{S}_E, n_e$	Detected events
$\mathbb{S}_{E_k}, n_{e_k}$	Events clustered as type k
$\mathbb{S}_T, n_t$	Types of events
$\mathbb{S}_U, n_u$	Events used to solve the NLLS problem

Parameters

x_s, y_s	Sensor coordinates
g_s	Sensor amplification factor
θ_s	Sensor Sensing direction
V_s	Sensor measurement
r_c	Electric conduit radius

Variables

x_c, y_c	Wire coordinates
I_c	Wire current
$g_k^{e_k}$	Current unbalance ratio for type k event

Chapter 1

Introduction

In recent years, with the advent of smart grid and smart home, advanced energy monitoring and management become more significant [1]. The need to monitor home energy use by home owners has motivated the research on measuring currents in three wires enclosed in a plastic conduit [2]. Accurate and easy-to-implement home current measurement can provide basic but vital information for smart homes and enable various smart home applications such as non-intrusive load monitoring (NILM) [27], home energy management [4] and demand response management [5].

Current sensing technology featured by low-cost wide-range current sensors is one of the basic measurement techniques for modern power systems, ranging from residential, industrial to utility practices [6]. Since it is not safe to install current measurement devices inside a home service panel, existing approaches rely on the measurements on incoming wires which are commonly above the service panel and enclosed in a plastic electric conduit. How to measure currents in a bundle of inaccessible, enclosed wires has been a challenging problem but with many potential applications.

In this introductory chapter, the background information regarding existing current sensing technologies and recent research works is provided. Then, the technical challenges of non-intrusive current measurement, for example, the inaccessibility of enclosed wires, the coupled magnetic field generated by multi-wire system, the unknown sensor parameters and so on are also identified. Finally, the thesis scope and outline are presented.

1.1 Overview of Current Sensing Technology

Current sensing technology using low-cost wide-range current sensors is playing a crucial role in modern power systems [6]. Current sensor performance comparison and application hints are shown in Table 1.1 and Table 1.2, respectively. Various apparatus and methods have been designed, proposed and used for residential, industrial and utility applications. How to achieve non-intrusive, accurate and easy-to-implement current measurement in a bundle of wires enclosed in a structure has been a challenging task but with tremendous potential applications. For example, Romex cable has two or three wires enclosed in a plastic cover. Without isolating the wires first, it has been a tough job to measure the currents of these wires. A method to estimate currents for such cables using external sensors was first patented in [7]. Contactless measurement of overhead line currents encouters similar challenges. In this case, magnetic fields measured by an array of sensors are used to estimate currents of distribution feeders [8].

Table 1.1: Current sensor performance comparison [6].

	Bandwidth	DC Capable	Accuracy	Thermal drift [ppm/K]	Isolated	Range	Power Loss
Shunt Resistor • Coaxial • SMD	MHz kHz-MHz	Yes	$0.1\% - 2\%$	$25 - 300$	No	kA mA $-$ A	W $-$ kW mW $-$ W
Copper Trace[1]	kHz	Yes	$0.5\% - 5\%$	$50 - 200$	No	A $-$ kA	mW
Current Transformer	kHz-MHz	No	$0.1\% - 1\%$	< 100	Yes	A $-$ kA	mW
Rogowski Coil	kHz-MHz	No	$0.2\% - 5\%$	$50 - 300$	Yes	A $-$ MA	mW
Hall Effect [1] (open-loop / closed-loop)	kHz	Yes	$0.5\% - 5\%$	$50 - 1000$	Yes	A $-$ kA	mW
Fluxgate	kHz	Yes	$0.001\% - 0.5\%$	< 50	Yes	mA $-$ kA	mW $-$ W
AMR Effect[1] (closed-loop, core-less)	kHz	Yes	$0.5\% - 2\%$	$100 - 200$	Yes	A	mW
Core-less open-loop (GMR, AMR, Hall Effect)[1]	kHz	Yes	$1\% - 10\%$	$200 - 1000$	Yes	mA $-$ kA	mW
Fiber-Optic Current Sensor[1]	kHz-MHz	Yes	$0.1\% - 1\%$	< 100	Yes	kA $-$ MA	W

[1] Using temperature compensation electronics

Magnetic field sensors [9], like coil sensors [10, 11], and Hall effect based sensors [12, 13], were utilized to capture magnetic fields and identify currents. Approaches based on sensor array were developed in order to make use of spatial difference and measurement redundancy of multiple sensors to achieve better measurement performance [14]. Reference [7] formulates the contactless

current measurement problem as an optimization problem using a high number of sensors to determine the current values, which is infeasible to be deployed on a sensing device with limited physical size. Coil sensors [11] as shown in Fig. 1.1 and Hall effect sensors [12, 13] as shown in Fig. 1.2 and Fig. 1.3 can be deployed around a single wire to detect the magnetic fields generated and measure the current inside. However, it is more complicated to measure the currents of a multi-wire system since the sensed magnetic fields are cross-coupled.

Table 1.2: Current sensor application hints [6].

	Cost[3] [USD]	Size [mm^3]	Limitations
Shunt Resistor[1]	> 0.5	> 25	An overcurrent can permanently damage the shunt resistor. High power losses make it difficult to measure high currents. In high voltage applications the missing electrical isolation is a problem.
Copper Trace[1,2]	> 0.5	> 25	The accuracy is degraded by noise due to the high amplification. The bandwidth may be limited by the gain-bandwidth product of the amplifier. Measuring the trace temperature might be difficult in some applications. No electrical isolation.
Current Transformer	> 0.5	> 500	A DC offset may saturate core material. For high currents a large core cross sectional area is required to avoid saturation. In high voltage applications the winding isolation becomes crucial. A high winding ratio leads to increased parasitic capacitance, which reduces the measurement bandwidth and common mode noise rejection.
Rogowski Coil	> 1	> 1000	The accuracy depends on the conductor position. Difficult to measure small currents due to poor sensitivity. A high number of turns reduces the measurement bandwidth.
Hall Effect (open-loop / closed-loop)	> 4	> 1000	AC currents with high frequency can overheat the core material. An overcurrent incident does introduce a magnetic offset that can only be eliminated with a degaussing cycle. Distinct thermal drift that has to be compensated.
Fluxgate	> 10	> 1000	Some variants induce notable voltage noise into the primary winding. Complicated control electronics. A high number of turns reduces the measurement bandwidth.
AMR Effect (closed-loop, core-less)	> 5	> 1000	Not practical for very high currents since the current has to flow through the sensor housing. Susceptible to external magnetic stray fields. Bandwidth limited to <1 MHz.
Core-less open-loop (GMR, AMR, Hall Effect)	> 2	> 25	Highly susceptible to external magnetic fields. If the sensor is close to the current carrying conductor, the skin effect may limit the frequency response.
Fiber-Optic Current Sensor	> 1k	> 10^6	Due to high complexity not suitable to measure small currents. Bending stress of the fiber-optic cable deteriorates the accuracy.

[1] Including amplification.
[2] Including temperature sensor.
[3] In high volume applications.
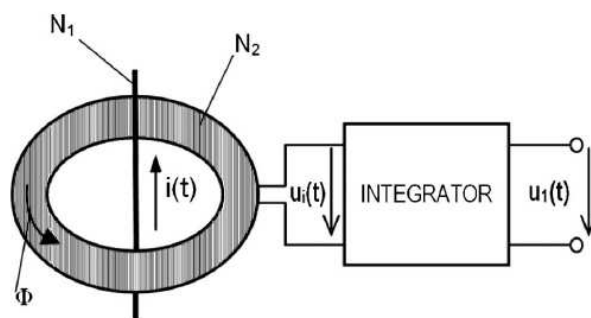
Figure 1.1: Rogowski coil with an integrator [11].
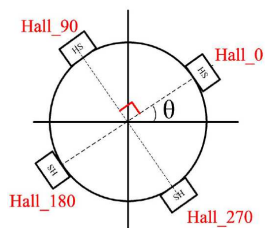
Figure 1.2: Arrangement of four Hall sensors [12].
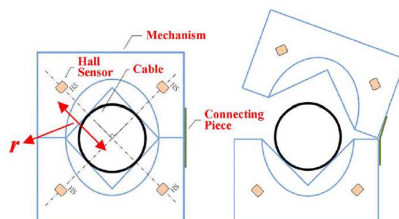
Figure 1.3: Configuration of the electronic current transformer (ECT) mechanism [13].

An approach to decouple the cross-coupled magnetic fields by building the relationship between sensor measurements and wire currents with known geometries of wires and locations of detectors is provided in reference [15]. An apparatus is designed in [16] as shown in Fig. 1.4 to measure two-wire currents with partly known wire positions. However, such measurement is not accurate enough to measure enclosed wires with unknown geometric information. Reference [17] and [18] implemented current measurement for two or three conductors based on the pre-assumed conductor geometric information from user selected Romex cable specification, which leads to large measuring errors and withdrawn products.
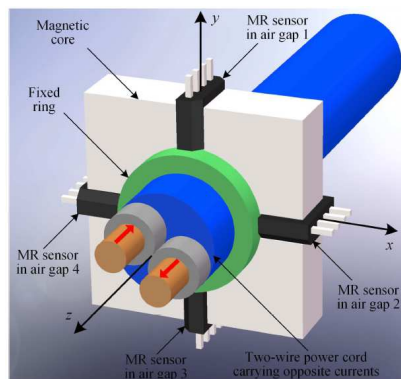
Figure 1.4: Schematic of proposed current sensor [16].

Evolutionary computation method is used in [19] to measure three phase currents with ten sensors as shown in Fig. 1.5. The evolutionary computation method using ten sensors has high computational complexity and could lead to non-convergence situation. A non-intrusive home current measurement problem is investigated in [20]. The proposed approach uses a dedicated on-site calibrator as shown in Fig. 1.6 to establish the relationship between wire currents and magnetic fields. The calibration device draws currents from the wires downstream of the sensing point. Yet, how to eliminate the use of on-site calibrator, reduce the number of sensors and develop an efficient solving algorithm are still open issues, which require extensive research. The objective of this thesis is to present an improved method to solve the aforementioned problems.
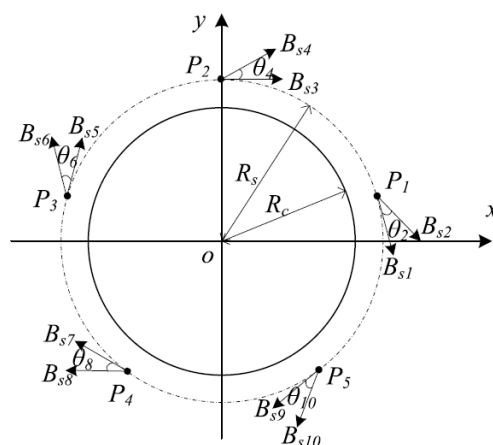
Figure 1.5: Layout of magnetic sensors in simulation study [19].
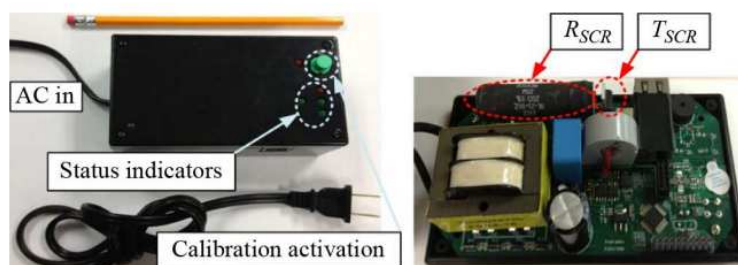
Figure 1.6: The prototype of the sensor calibrator [20].

1.2 Technical Challenges of Non-Intrusive Current Measurement

Many research works have been done to solve some of the technical challenges of non-intrusive current measurement. This section discusses some of the solved and remaining technical challenges of non-intrusive current measurement.

An electric current generates magnetic field surrounding it and the magnetic field at a point in space relates to the current magnitude, current direction, current length, and distance between the point and the electric current according to Biot-Savart law. A point P in space will sense a magnetic field B_1 generated by the current I_1 flows through $wire_1$. Due to the fact that Maxwell's equations are linear, electric fields satisfy the superposition principle. As an illustration shown in Fig. 1.7, if B_1, B_2,...,B_N at a point P in space are the magnetic fields resulting from currents I_1, I_2,...,I_N flow through $wire_1$, $wire_2$,...,$wire_N$, the overall magnetic field B at a point P in space is the sum of B_1, B_2,...,B_N, namely $B = \sum_{i=1}^{N} B_i$.
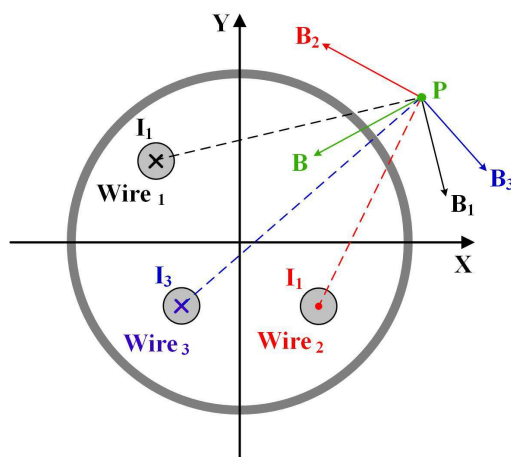
Figure 1.7: Cross-coupled magnetic field generated by wires.

The magnetic field sensed by a current sensor of a sensing device is a cross-coupled one of all the magnetic fields generated by the enclosed wires. In order to separately measure the currents of the enclosed wires (rather than the overall equivalent current), the first technical challenge is how to decouple the current

sensor sensed cross-coupled magnetic field generated by all the enclosed wires. The cross-coupled magnetic field can be decoupled if the physical positions of the wires and the detectors are known [15].

The problem of measuring currents of enclosed multi-wire system using current sensor array is illustrated using Fig. 1.8. In this figure, a set of magnetic field sensors are deployed around the conduit with the wires enclosed. The goal is to determine the wire currents inside the conduit using sensor measurement data only. Due to the fact that the Biot-Savart law only applies to a point in space, the current sensor used to sense the magnetic field should be small enough. For existing sensing devices, the sensor electrical and geometric parameters are assumed with reference values. The small physical size of the current sensor as shown in Fig. 1.9 makes it difficult to accurately acquire these parameters. The accuracy of these parameters have strong impact on the current measurement accuracy. Another technical challenge is how to accurately acquire the sensor electrical and geometric parameters of a sensing device. The sensor parameters could be acquired through the manufacturing process.
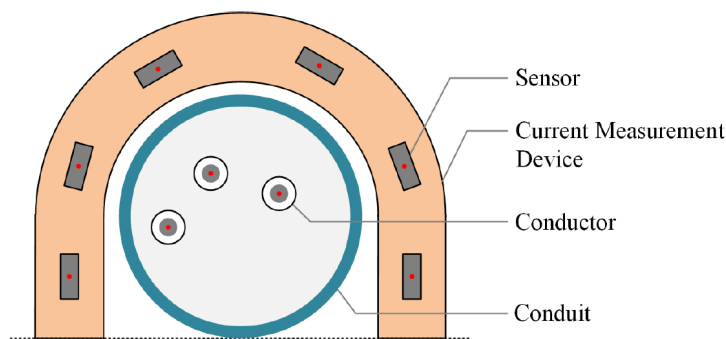
Figure 1.8: System scheme of sensor array for enclosed multi-wire system.

Figure 1.9: Small physical size of coil sensor.

The research works and potential applications of non-intrusive current measurement for enclosed multi-wire system, i.e., electric cable, electric wires enclosed in conduit, overhead lines and so on share a common characteristic, namely measuring the currents on conductors that cannot be accessed individually as shown in Fig. 1.10. In other words, the currents flow through the enclosed multi-wire systems can not be measured one by one. Besides, whether or not there are currents flowing in all of the enclosed wires is unknown.

The objective of non-intrusive current measurement is to find the currents (and positions) of the wires based only on the measured magnetic field data acquired from the sensing device. Relying on the assumption of wire configuration or physical positions is considered to have strong impact on the current measurement accuracy. The wire configuration or physical positions are actually inaccessible unknown parameters. An approach that does not rely on any assumption of wire configuration or physical positions is needed. Therefore, the major technical challenge of non-intrusive current measurement of enclosed multi-wire system has been identified as the inaccessibility of individual wires with unknown physical positions and unknown currents. Evolutionary computation method with ten sensors is proposed in [19] to solve the wire positions. An dedicated on-site calibrator is used in [20] to acquire the trans-impedance matrix consists of wire and sensor geometrical information.

Figure 1.10: Inaccessibility of individual wires enclosed in conduit.

Despite all the existing research works, there are still some of the technical challenges and open issues that require extensive research. Solving the currents in a multi-wire system using a large number of current sensors have several drawbacks. First, it increases the cost of sensing device. Although the current

sensors are usually cheap, each current sensor needs an end amplifying circuit to amplify the sensed magnetic field strength and convert it to voltage output. It requires high stability of the sensing device with a large number of sensors installed. Besides, a large number of current sensors increase the requirement of data acquisition system used to capture and record the sensor measurements because a large number of channels are needed. Moreover, the computational complexity of solving algorithm also increases with the number of sensors, which in turn causes longer computation time and even non-convergence. As discussed above, some of the remaining non-intrusive current measurement technical challenges are:

- Reducing the number of sensors used in the sensing device and eliminate the use of on-site calibrator.

- Design and implementation of low-cost, easy-to-implement sensing device.

- Implementing an accurate and efficient solving algorithm with less computational complexity.

For some specific applications of non-intrusive current monitoring (e.g., North American home current measurement), dedicated and accurate models of the whole measurement environment and system are needed. A North American home power supply system consists of distribution system, service transformer, service entrance, service panel and home appliances . Dedicated and accurate mathematical modelings are necessary to achieve accurate home current measurement. A lack of consideration of any underlying impact (e.g., the existence of small grounding current), could result in inaccurate measurement results, Therefore, another challenge of non-intrusive home current measurement is:

- Dedicated and accurate modelings of entire home power supply system (including the grounding system).

1.3   Thesis Contributions and Organization

The overall objective of this thesis is to solve the remaining but critical technical challenges regarding to non-intrusive home current measurement as discussed in Section 1.2. The main contributions of this thesis work are as follows:

- A novel event-based current measurement method based on an unique observation of North American homes is proposed to simplify the current measurement problem, which in turn reduces the number of sensors and the computational complexity.

- A low-cost and easy-to-implement sensing device is designed and implemented to achieve real time home current measurement without the on-site calibrator.

- The unknown wire position solving task is formulated as a nonlinear least square (NLLS) optimization problem and is effectively solved using the state-of-art nonlinear programming (NLP) algorithm.

- The whole North American home power supply system (especially the grounding system) and the sensing system are accurately modeled and validated. The proposed method and sensing system are validated through extensive laboratory and field tests.

The remainder of the thesis is organized as follows:

Chapter 2 presents the studies of North American home power supply system including the home service entrance method, service panel and home appliance wiring. The design, implementation and manufacturing process of the sensing device are presented. The detailed models of sensed magnetic field for single wire and multi-wire system and the magnetic field decoupling method are also discussed.

Chapter 3 presents a novel event-based non-intrusive home current measurement method based on unique observations of North American homes. The current measurement problem is simplified by using extracted appliance state changing events. The event detection method using sensor measurements and event clustering method using Cosine Similarity are also shown. The unknown wire positions solving task is formulated as a NLLS optimization problem and

is effectively solved using the NLP algorithm. Then real-time current measurement is achieved by building the trans-impedance matrix using the solved wire positions and sensor parameters acquired through the manufacturing process and the sensor measurements.

Chapter 4 shows the laboratory and field tests results. The laboratory experiment consists of two types of tests including aluminum bar test and electric service wire test. The sensing system is also tested in a real residential house. Measurement results and system installation processes are presented.

Chapter 5 further studies the home underground service entrance point measurement. The measurement results of the most commonly used USEB cable using the proposed method is presented. Due to the special configuration of the USEB cable, equivalent single-conductor and two-conductor models for the USEB cable neutral strands are investigated and built. The USEB cable neutral current solving algorithms using the equivalent models are built and the laboratory test results are shown.

Chapter 6 presents the main thesis conclusions, contributions and suggestions for future studies and improvements.

Chapter 2

Non-Intrusive Home Current Measurement System Model

2.1 Overview

This chapter presents the studies and modelings of North American homes and sensing system. A study of North American home power supply system including service entrance methods, home service panel and home appliance wiring is introduced in Section 2.2. The sensing device design, implementation and manufacturing process are presented in Section 2.3. Mathematical models of sensed magnetic field generated by single wire, multi-wire system and the magnetic field decoupling method are shown in Section 2.4. Finally, a brief summary of this chapter is given in Section 2.5.

2.2 North American Home Wiring

The National Electrical Code (NEC) [22] gives the standard for the safe installation of electrical wiring and equipment in the United States. It is typically followed in North America to standardize the safe electrical practices. Cities adopt and enforce building codes that specify standards and practices for electrical systems for protection. The NEC has become the standard of electrical requirements. An electrician in North America will spend years to study the NEC requirements to obtain the license.

Article 230 of the NEC [22], which consists of seven parts, provides the installation requirements for service conductors and equipments. Parts II Overhead Service Conductors, III Underground Service Conductors, and IV Service Entrance Conductors address conductors. The requirements for equipments are covered in Parts I General, V Service Equipment, VI Disconnecting Means, and VII Overcurrent Protection.

The standards, requirements and definitions of North American home service are given in National Electrical Code [22] and further explained in reference [23]. This section provides the studies and investigations of North American home power supply system.

2.2.1 Service Entrance

The service entrance includes all the wires, devices and fitting that carry electricity from transformer of the power company to the consumer [23]. All the electrical energy supplied to home appliances must first pass through the service entrance equipment. The service components protect, meter and distribute the power to homes.

NEC article 230 gives the definition of the technical terms regarding home service entrance as follows:

- Service entrance: all of the wires, devices, and fittings that carry electricity from the power company's transformer to consumer.

- Service drop: overhead wires brought to the building that are run overhead from the utility pole to the service point.

- Service lateral: underground wires brought to the building that are routed underground, from either a pole of transformer pad to the service point.

- Service point: the point of connection between the facility of the servicing utility and the premises wiring.

The service entrance consists of the following parts:

- Wires from the utility pole or transformer to the dwelling service point.

- Service entrance conductors.

- Meter socket, pan, or enclosure.

- Service entrance panel with breakers or fuses and a main disconnecting means.

- Grounding system.

- Fittings, fasteners, and other hardware necessary to install the service equipment.

The structure of service transformer used to decrease the high voltage of the primary side to $240V$ voltage of the secondary side and its wiring are shown in Fig. 2.1. The most common residential service is a three-wire, single-phase system, which consists of two ungrounded conductors and one grounded conductors as shown in Fig. 2.2. One ungrounded hot conductor is usually black and the other red, while the grounded neutral is usually yellow. This system can provide $120V$ and $240V$ to home appliances.
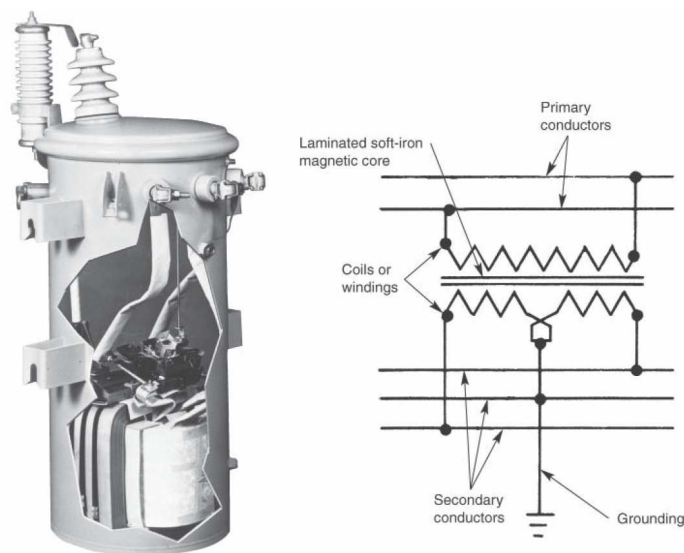
Figure 2.1: Service transformer and its wiring [23].
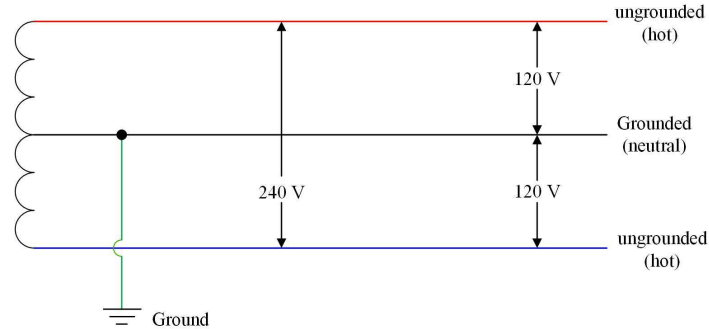
Figure 2.2: Single-phase, three-wire system.

Service conductors are those conductors from the service point to the service disconnecting means (service equipment, rather than meter). Service conductors include service entrance conductors for both overhead (service drop) and underground (service lateral).

One of the service entrance methods is overhead service entrance, i.e., overhead service entrance conductors (service drop) are connected to utility company secondary lines as shown in Fig. 2.3. The overhead service conductors then go through the service heads, which are used to keep water from entering the conduit leading to the meter enclosure. The service conductors should extend through the head for approximately 3' to provide a drip loop. A drip loop is to prevent water from entering the service head. The overhead service entrance conductors are then connected to the electric meter through the service drop mast, which is a rigid conduit that contains the service entrance cable and is mounted between the service head and the meter.
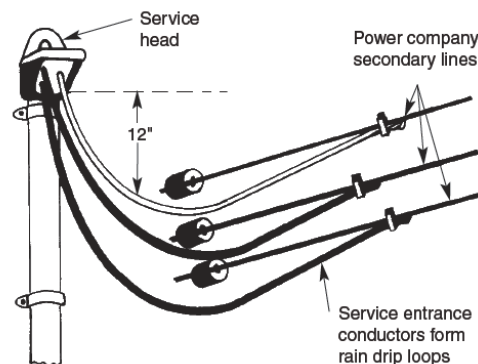
Figure 2.3: Service drop connected with utility company secondary lines [23].

A typical overhead service drop and service entrance method is shown in Fig. 2.4. The service entrance conductors lead power to the home service panel after connected to the electric meter. The service panel distributes power to different electric sockets at different localities supplying power to home used appliances. Grounding the service entrance is vital to the safety of the entire home power supply system. Grounding the service entrance involves connecting the neutral conductor with the earth through the grounding conductor.
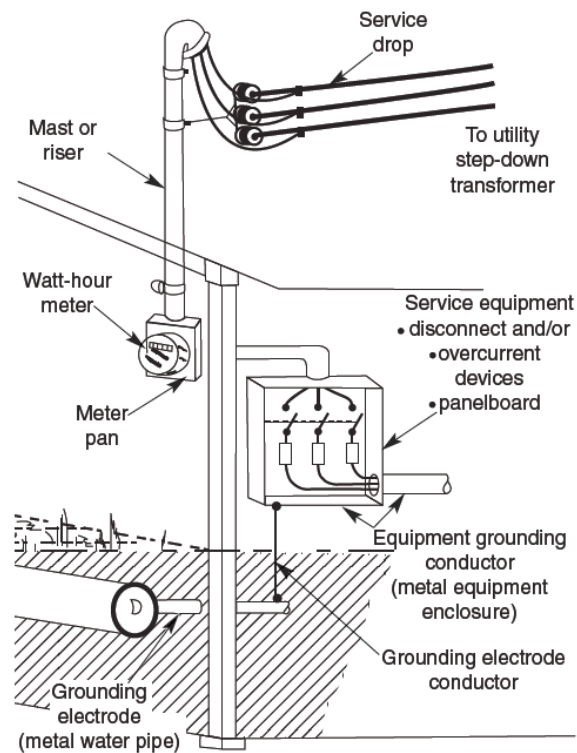
Figure 2.4: Typical overhead service drop and service entrance [23].

Another service entrance method is underground service entrance, which uses underground service entrance conductors that are routed underground (service lateral), from the transformer pad to the service point. A typical underground service entrance is shown in Fig. 2.5. Underground service entrance conductors, whether enclosed in conduit or cable, should be installed in a straight path to make finding the buried conductors easier.
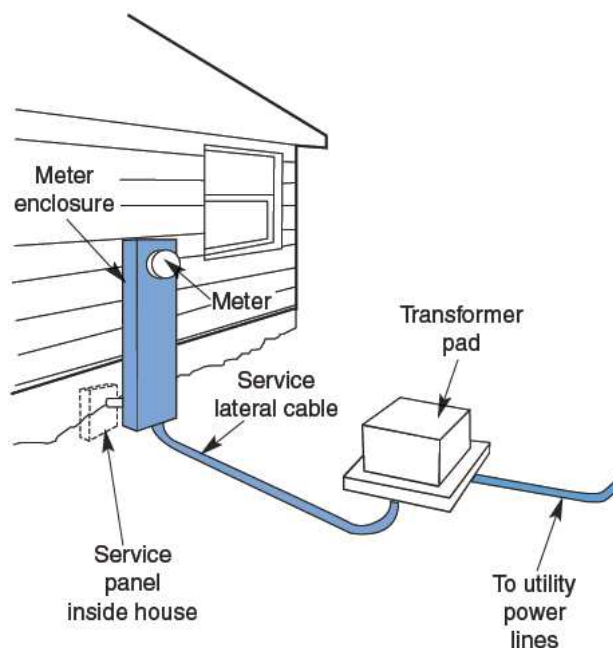
Figure 2.5: Typical underground installation for a service entrance [23].

The major difference between overhead service entrance and underground service entrance is whether the service entrance conductors that connect the service point and the utility power lines are through overhead (service drop) or underground (service lateral).

Service entrance conductors may be type THW, THWW, XHHW, RHH or RHW. Service entrance conductors can be run through a conduit or a service entrance cable (SEC) as shown in Fig. 2.6. The service entrance cable commonly consists of two conductors as hot wires and one stranded bare neutral wrapper. The neutral strands are twisted into one conductor before being connected. Most service drops in North American homes use triplex cable as shown in Fig. 2.7. The triplex cable consists of a bare neutral wire around which two insulated wires are loosely wrapped. NEC 230.43 Wiring Methods explains the methods [22] that are permitted to wire the service conductors. There may exist metal conduit, intermediate metal conduit and metal covering cable for home service entrance, which could bring magnetic field shielding problem and affect the magnetic field. Off all the methods listed, triplex cable and service entrance cable are most commonly used in North American house dwellings for overhead and underground service entrance separately.
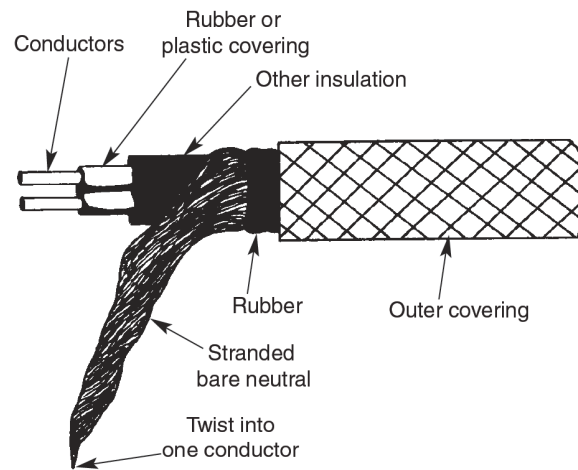
Figure 2.6: Typical service entrance cable used in underground service entrance [23].
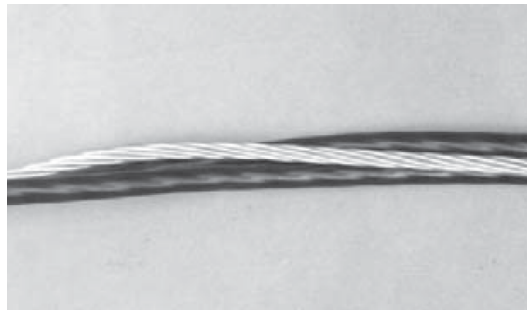
Figure 2.7: Typical triplex cable used in overhead service entrance [23].

The right size of service entrance conductors is also fundamental in home service entrance. The NEC gives the instructions on proper sizes, types and allowable ampacities of insulation of conductors for single-phase, three-wire service entrance as shown in Table 2.1. For new single-family dwellings, at least $100A$ service is required by the NEC. Services with $150A$ or $200A$ rating are preferred for homes with electrical heating systems or potential future expansion. However, to make sure of the service is sized properly for a home, the total load should be calculated based on various home appliances. Aluminum service entrance conductors with at least AWG 3 size are commonly used.

Table 2.1: Service entrance conductor sizes specified by the NEC [22].

Table 310.15(B)(7) Conductor Types and Sizes for 120/240-Volt, 3-Wire, Single-Phase Dwelling Services and Feeders. Conductor Types RHH, RHW, RHW-2, THHN, THHW, THW, THW-2, THWN, THWN-2, XHHW, XHHW-2, SE, USE, USE-2

Service or Feeder Rating (Amperes)	Conductor (AWG or kcmil)	
	Copper	Aluminum or Copper-Clad Aluminum
100	4	2
110	3	1
125	2	1/0
150	1	2/0
175	1/0	3/0
200	2/0	4/0
225	3/0	250
250	4/0	300
300	250	350
350	350	500
400	400	600

2.2.2   Home Service Panel

The home service panel is used to distribute the power supplied by utility companies to different sockets at different localities in home. Some homes may have more than one service panel (a main panel and a subpanel) to distribute the power supply. A typical North American home service panel wiring is shown in Fig. 2.8. As shown in Subsection 2.2.1, the service transformer supplies $120V$ and $240V$ power to homes through the single-phase, three-wire system. The service transformer neutral is grounded at the secondary side of the transformer at the pole. The grounding system of the service entrance is vital to the safety of the home power supply system. NEC article 250 [22] gives detailed specifications and requirements for grounding and bonding.

The NEC requires that all the service entrance should be grounded through the neutral-ground bond at the service panel, i.e., the neutral wire and ground wire are connected at the service panel using the neutral-ground bond. The grounding wire is then connected to the grounding conductor (metal water pipe). The metal shell of some high power home appliances are usually grounded. The appliance will work normally without the ground wire since it is not one part of the conducting path that supplies power to the appliance.
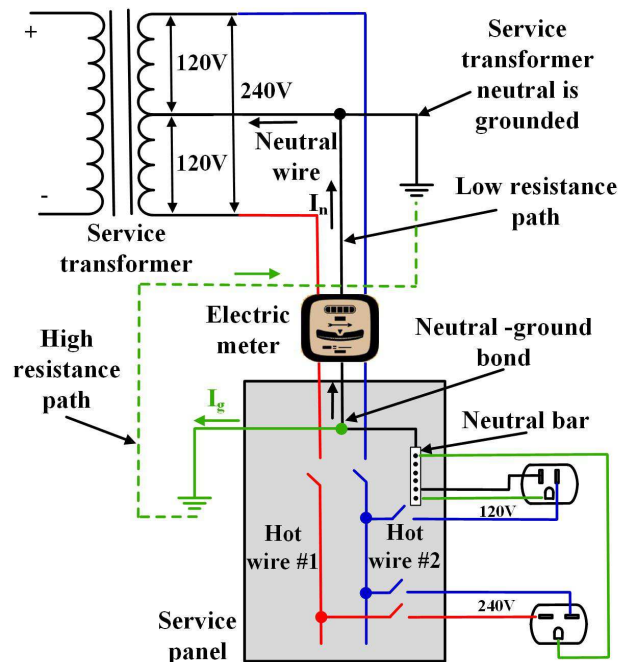
Figure 2.8: Typical home service panel wiring.

One role of the ground wire is to force the breaker to trip by supplying a path to ground if a hot wire contacts with the metal case of an appliance by accident. It brings dangerous high voltage to the case of an appliance if an electrical fault happens. In this case, the circuit breaker is expected to trip immediately to remove the hazard. However, only connecting the ground wire to the ground conductor connected to the earth is not usually sufficient to trip the circuit breaker. Thus the NEC article 250 requires that the ground wires be tied to the neutral wire at the service panel. In this way, if a line-to-case fault happens in accident, the fault current will flow through the appliance ground wire to the service panel and then flow to the neutral path back to the service transformer. Then, the fault current becomes one part of the overall flow, which in turn produces a high enough fault current to trip the circuit breaker of the transformer. The process of tying the ground wire and neutral wire is called bonding. For electrical safety of home, the system needs to be both grounded and bonded.
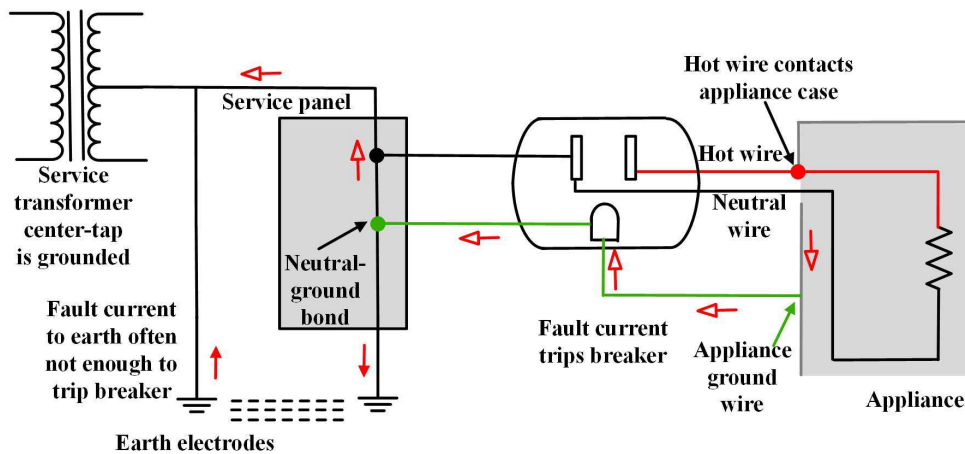
Figure 2.9: Neutral-ground bond at service panel to clear ground fault.

2.2.3 Home Appliance Wiring and Grounding

The typical North American home power supply network is shown in Fig. 2.10. The service transformer supplies $120V$ and $240V$ power through the single-phase three-wire system to customers. The transformer neutral is grounded at the pole and the service entrance neutral conductor are bonded to the ground through the neutral-ground bond at the home service panel. Some appliances are connected between either one of the two hot wires and the neutral wire for $120V$ power supply. And some appliances like kitchen stove, air conditioner, refrigerator and so on are connected between the two hot wires for $240V$ power supply. The two hot wires and the neutral wire are named as A, B and N in this thesis for simplification. The currents at the two hot wires and the neutral wire are named as I_a, I_b and I_n respectively. The unbalanced current which is caused by the unbalanced loads between AN and BN is named as I_u. And the grounding current is named as I_g.

Due to the neutral-ground bond at the service panel, one part of the unbalanced current I_u will flow through the ground wire (I_g) to the ground, and then, to the service transformer ground back to the service transformer. Another part of the unbalanced current I_u will flow back to the service transformer through the service neutral conductor (I_n).

The ground current I_g flows through the grounding resistance R_G at the customer location will generate the neutral-to-earth voltage (NEV), which is the main cause of stray voltage problem [24]. The NEV at a customer site can be determined as shown in (2.1).

$$NEV = V_n = R_G \times I_g = R_G \times (I_u - I_n). \tag{2.1}$$
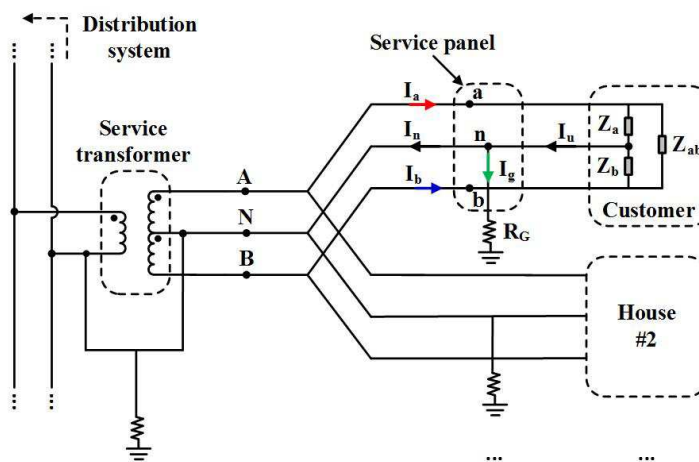
Figure 2.10: Typical North American home power supply network.

A new concept called the current return ratio (K) used to determine the relative contributions of the customer and external causes of the NEW is first proposed in reference [24]. The unbalanced current I_u caused by the unbalanced customer loads returns to the service transformer either through the service neutral conductor (I_n) or through the ground (I_g). The external factors that is unrelated to the customer side is defined as I_{ne} and the following relationship as shown in (2.2) holds. The current return ratio K could be understood as the percentage of the unbalanced current I_u that returns to the service transformer through the service entrance neutral conductor.

$$I_n = K \times I_u - I_{ne}. \tag{2.2}$$

It is also shown in reference [24] that the current return ratio K is only determined by the circuit and grounding impedances and typical values of K are estimated as from 0.85 to 0.95. A measurement-based method to calculate the current return ratio K using measured home currents is investigated in [25]. Using a dedicated device or a power quality monitor as shown in Fig. 2.11 to sense the currents I_a, I_b, and I_u at the service entrance point, the K ratio, the external and customer contributions to NEV could be calculated.
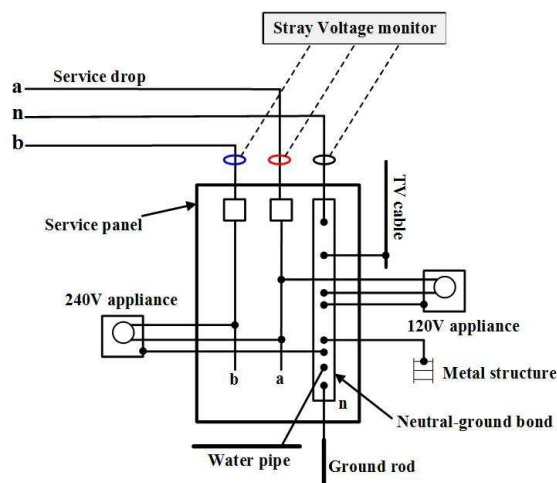
Figure 2.11: Layout of service panel with stray voltage monitor.

The relationship among K, I_n, I_u, and I_{ne} is shown in (2.2) and is applied to two sets of current measurement data, extracted from consecutive instants of time in order to determine the K ratio, as follows:

$$I_{n1} = K \times I_{u1} - I_{ne1}, at\ instant\ t_1. \tag{2.3}$$

$$I_{n2} = K \times I_{u2} - I_{ne2}, at\ instant\ t_2. \tag{2.4}$$

Subtracting (2.4) from (2.3) yields:

$$\begin{aligned} I_{n2} - I_{n1} &= K \times (I_{u2} - I_{u1}) - (I_{ne2} - I_{ne1}) \\ &\to \Delta I_n = K \times \Delta I_u - \Delta I_{ne}. \end{aligned} \tag{2.5}$$

To calculate the K ratio from (2.5), the external current variation ΔI_{ne} should be small compared to the variation of unbalanced current ΔI_u. Thus, two conditions should be fulfilled in order to accurately estimate K ratio:

- The unbalanced current I_u should change between two collected data sets, i.e., $\Delta I_u \neq 0$.

- The interval between two data sets should be small to minimize the probability of changes in the external system, i.e., $\Delta I_{ne} \approx 0$.

If the above two conditions are fulfilled, the current return ratio K can be obtained using equation (2.6). In practice, the K ratio is obtained from a large amount of current change snapshots selected over a measurement period of several hours to even days.

$$K = \frac{\Delta I_n}{\Delta I_u}.$$

(2.6)

Both neutral current I_n and ground current I_g can be divided into two components as presented in (2.7) and (2.8). I_{nc} and I_{ne} are, respectively, the customer and external components of the neutral current, while I_{gc} and I_{ge} are, respectively, the customer and external components of the ground current.

$$I_n = I_{nc} - I_{ne}.$$

(2.7)

$$I_g = I_{gc} + I_{ge}.$$

(2.8)

By comparing (2.5) to (2.7), customer contribution to the neutral current is given by

$$I_{nc} = K \times I_u = K \times (I_a + I_b).$$

(2.9)

Part of the unbalanced load current I_u returns to the external site through the service entrance neutral conductor (I_{nc}) and the remaining current returns through the customer grounding point (I_{gc}). Therefore, $I_u = I_{nc} + I_{gc}$, and the customer contribution to ground current is given by:

$$I_{gc} = I_u - I_{nc} = (1 - K) \times I_u = (1 - K) \times (I_a + I_b).$$

(2.10)

The external ground current contribution (I_{ge}) can be determined as follows:

$$I_{ge} = I_g - I_{gc} = I_u - I_n - I_{gc} = K \times (I_a + I_b) - I_n. \qquad (2.11)$$

Therefore, after estimating the current return ratio K using the home measured currents, the external and customer contributions of ground current and neutral current can be calculated and then the relative contributions to the NEV could also be estimated. Three residential houses at Edmonton, AB, Canada are installed with stray voltage contribution monitor as shown in Fig. 2.12 and monitored separately over one month.
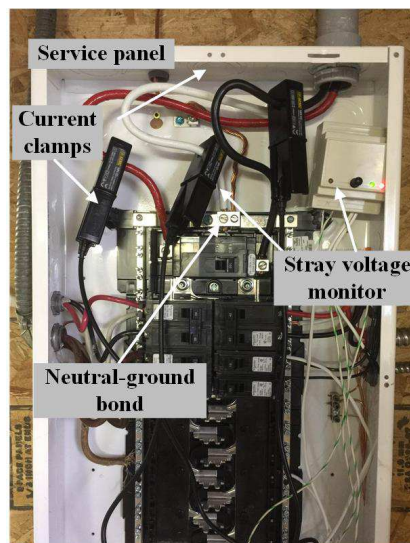
Figure 2.12: Stray voltage contribution monitor installed at a residential house.

Fig. 2.13 shows the ground current magnitudes of three residential houses at three example days. Fig. 2.14 shows the ground current percentages ($\frac{I_g(t)}{max(I_a(t), I_b(t))} \times 100\%$) of three residential houses at example days. We could see that residential house 1 and 2 have relatively small ground current magnitudes and percentages compared with residential house 3.
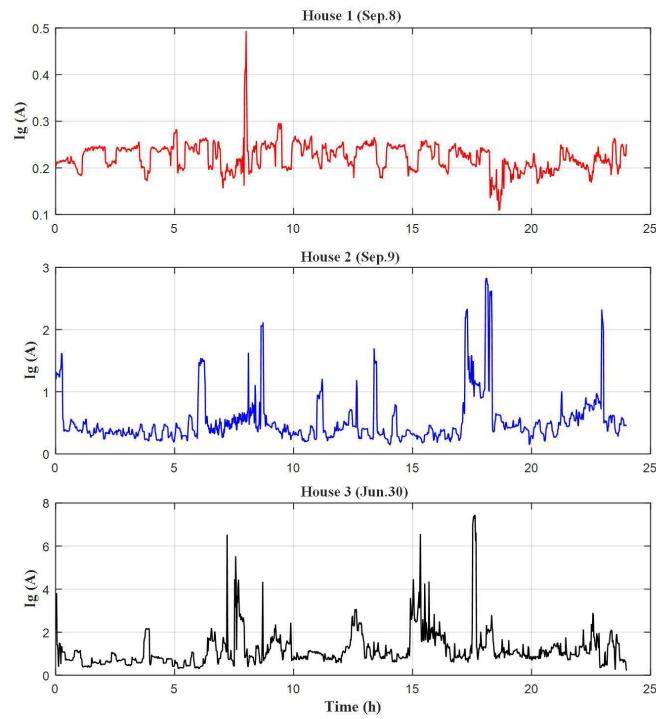
Figure 2.13: Ground currents of three residential houses.
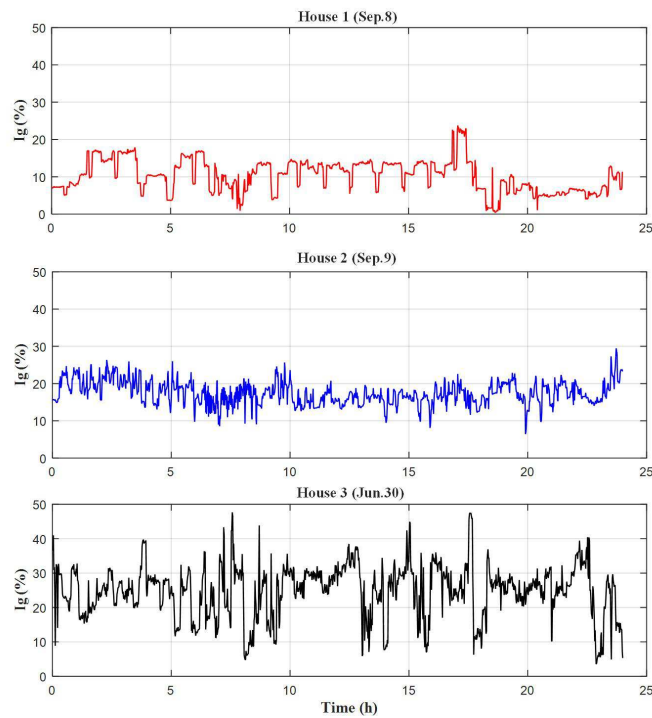
Figure 2.14: Ground current percentages of three residential houses.

The current return ratio behaviors of the three residential houses are calculated at ten separate days and are shown in Fig. 2.15 with absolute values around 0.98, 0.95, and 0.44 respectively. The absolute values of K of the three residential houses over time are shown in Fig. 2.16. The current return ratios of three residential houses are generally constant with small variations.
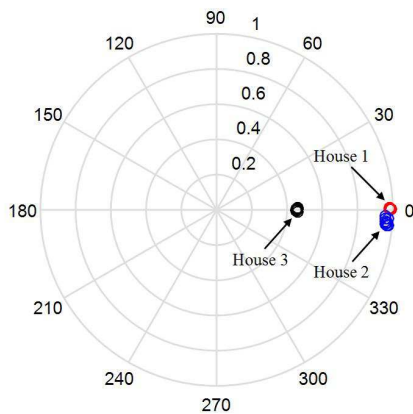
Figure 2.15: Current return ratio behaviors of three houses.
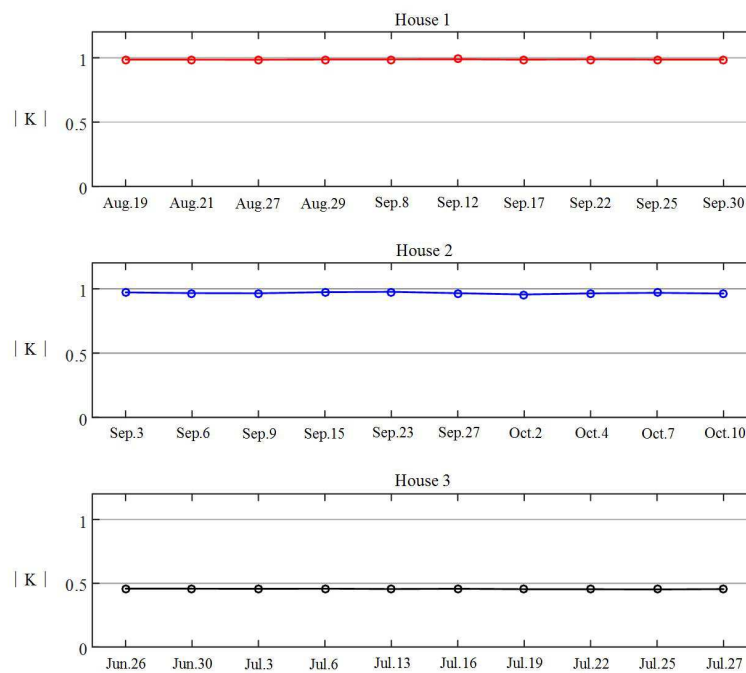
Figure 2.16: Current return ratio behaviors of three houses over time.

2.3 Sensing Device

2.3.1 Design and Implementation

A typical North American home service panel is shown in Fig. 2.17, which leads $120V$ and $240V$ power from service transformer to home appliances. Three wires are enclosed in the incoming conduit including two hot wires and one neutral wire carry $+120V$, $-120V$ and $0V$ voltages, respectively. The neutral wire is grounded through neutral-ground bond at the service panel for ground fault protection. The designed sensing device can be deployed at the service entrance conduit to detect the mixed magnetic fields generated by the three wires enclosed in the conduit.
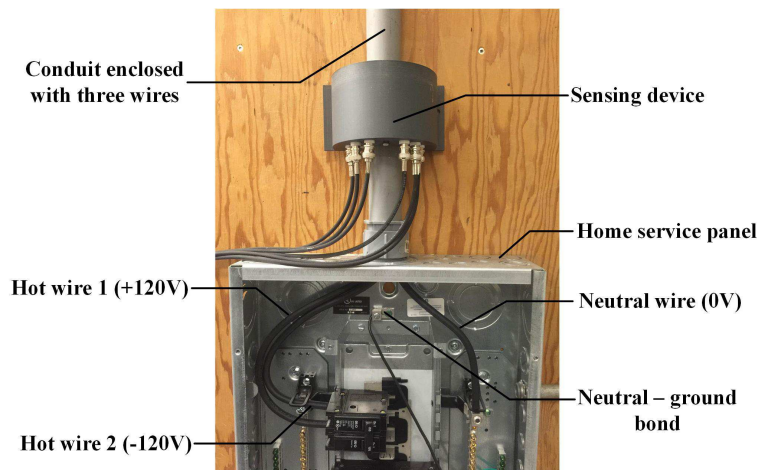
Figure 2.17: The sensing device deployed at service entrance conduit.

The sensing device is designed with a U-shape shell that could be easily clamped on the service entrance conduit. The magnetic field sensors measuring the magnetic fields surrounding the conduit are shown in Fig. 2.18. A total number of six coil sensors are placed with approximately equal intervals in the device to fully utilize the space diversity. The sensing device is connected to the NI data acquisition (DAQ) system for data recording. A PC is used to process the recorded data and calculate the currents. The current measurement results can be further uploaded and displayed on an Internet website for end users to access through electronic devices.
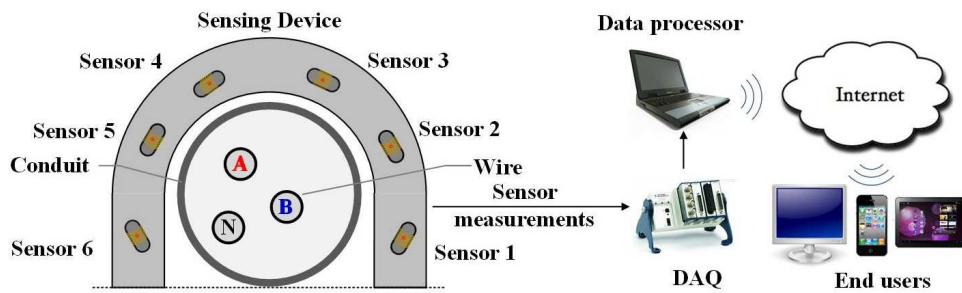
Figure 2.18: The sensing device layout.

The designed and implemented sensing device prototype is shown in Fig. 2.19. The coils sensors are deployed in a 3D printed non-magnetic bar and fixed in the sensing device. A total number of six coil sensors are used to sense the mixed magnetic fields and connected to the operational circuits which consist of low-pass filters and analog amplifiers. A 16-bit simultaneous analog-to-digital converter (ADC) is used and the circuit outputs are connected to Bayonet Neill-Concelman (BNC) connectors. The coil sensors and operational circuits are fixed in the U-shape 3D printed shell. The sensing device is powered by a power supply circuit and the sensor measurements can be recorded using NI DAQ system. The ADC modules used are within $\pm 9V$ range. The minimum recognizable signal step is therefore $\frac{2 \times 10V}{2^{16}} = 0.27mV$, which leads to maximum $\frac{1}{2^{16}} = 1.53\%$ relative error of acquired sensor measurements.
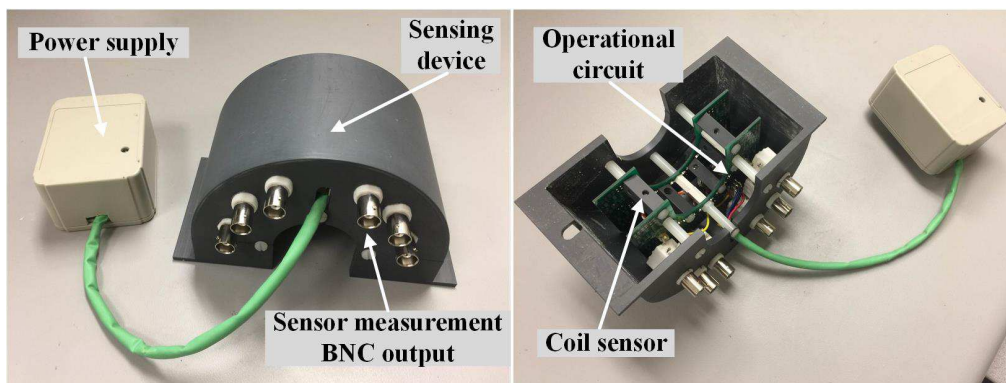
Figure 2.19: The designed and implemented sensing device prototype.

2.3.2 Manufacturing Process

The problem of non-intrusive current measurement can be described as: To solve for the wire currents with measured magnetic fields. Such a problem is unsolvable since both sensor and wire positions are unknown, namely, there are more unknowns than available equations. Increasing the number of sensors can establish more equations but it also introduces more unknown sensor positions. The sensor parameters are recognized to be independent of wire configurations. It is, therefore, sensible to acquire the sensor positions and sensing orientations w.r.t. a reference point. Once the sensor parameters are obtained, the problem of measuring wire currents then becomes solvable.

The sensor parameters are, unfortunately, not easy to determine. Due to the small size of the coil sensor, it is very difficult and even impossible to install sensors at precise positions and with desired sensing orientations. It is even more difficult to measure sensor positions and sensing orientations using mechanical methods. Secondly, each sensor has an operational circuit to filter and amplify the sensor signals, whose gain factor should be established as well. Otherwise, additional unknown variables are introduced by the sensor geometrical and electrical parameters.

A manufacturing process is used to accurately acquire the sensor parameters including sensor positions (x_s, y_s), sensing orientation (θ_s) and gain factor (g_s) of operational circuit. Table 2.2 shows the sensor geometrical and electrical parameters obtained through the manufacturing process and are taken as known parameters in the whole thesis. The acquired sensor parameters are further shown in Fig. 2.20.

Table 2.2: Sensor parameters.

Sensors	$x_s(mm)$	$y_s(mm)$	g_s	$\theta_s(rad)$
1	27.69	−14.78	3.08	0.068
2	27.15	9.55	3.11	−0.020
3	15.24	24.07	3.17	−0.062
4	−13.16	24.71	3.03	0.121
5	−25.63	10.76	2.93	0.097
6	−27.97	−12.13	2.85	−0.144
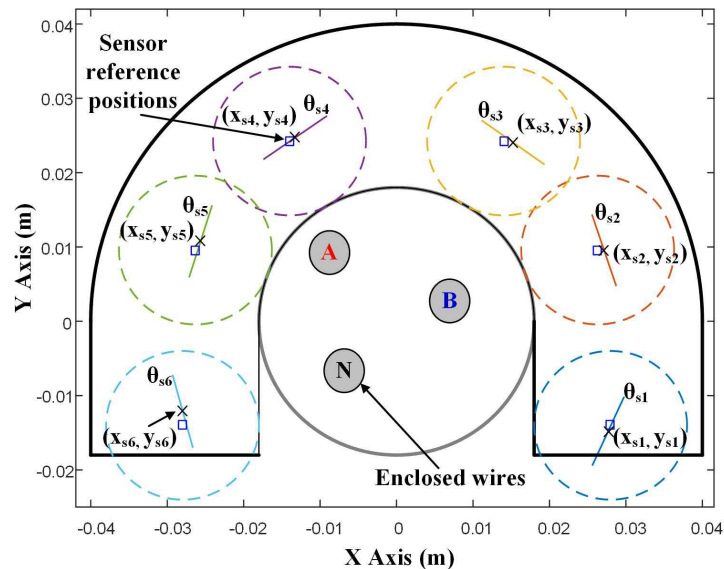
Figure 2.20: Sensor parameters acquired from manufacturing process.

2.4 Model of Sensed Magnetic Field

2.4.1 Magnetic Field Generated by Single Wire

The mathematical model of sensor sensed magnetic field generated by single wire current is derived in this subsection. As mentioned in previous subsection, the sensor geometrical and electrical parameters of the i-th one including sensor positions (x_{si}, y_{si}), sensing direction θ_{si} and gain factor of operational circuit g_{si} are acquired through a manufacturing process and are taken as known parameters.

An ideal long and straight wire with AC current produces an magnetic field around it, which can be captured by magnetic sensors like coil sensors. The magnetic field generated by a single current at a point can be obtained using Biot-savart law. The magnetic field generated by current I_a in wire A of position (x_a, y_a) at the sensing position S_i as shown in Fig. 2.21 can be expressed as:

$$B_{ai} = \frac{\mu_0}{2\pi L_{ia}} I_a. \tag{2.12}$$
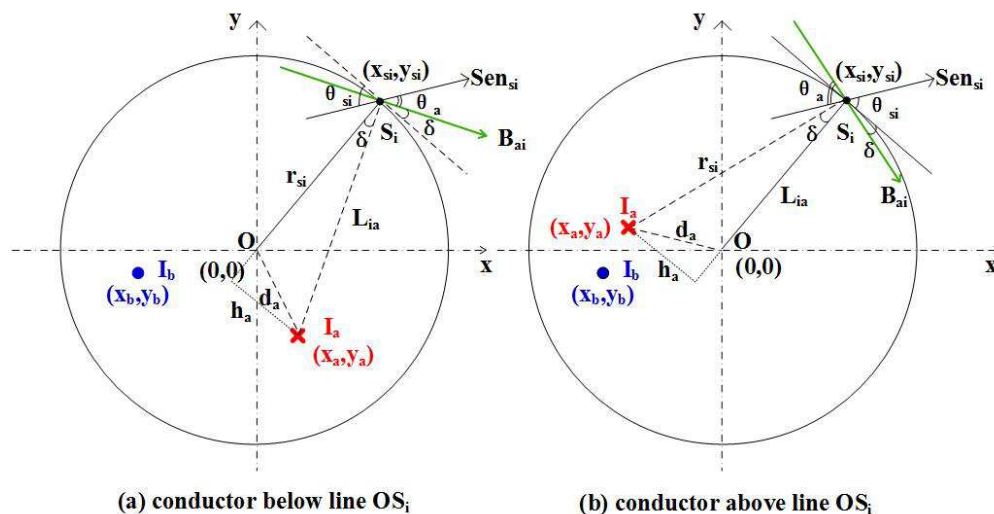
Figure 2.21: Sensed magnetic field generated by a single wire.

An induced voltage is generated on the coil sensor by the projection of the magnetic field onto the sensing direction Sen_{si}. This voltage signal is filtered and amplified by the operational circuit with gain factor g_s and output voltage V_s. The output signal is then digitalized by the ADC and finally recorded for analysis. The voltage output of the i th sensor generated by a single wire current I_a at position (x_a, y_a) is expressed as:

$$V_{si} = g_{si} \frac{\mu_0 \cos \theta_a}{2\pi L_{ia}} I_a. \tag{2.13}$$

From Fig. 2.21 (a), for the cases that the wire is below line OS_i, we have:

$$r_{si} = \sqrt{x_{si}^2 + y_{si}^2}. \tag{2.14}$$

$$d_a = \sqrt{x_a^2 + y_a^2}. \tag{2.15}$$

$$L_{ia} = \sqrt{(x_{si} - x_a)^2 + (y_{si} - y_a)^2}. \tag{2.16}$$

Using the law of cosine, and substituting (2.14), (2.15) and (2.16), we have:

$$\cos \delta = \frac{r_{si}^2 + L_{ia}^2 - d_a^2}{2r_{si}L_{ia}} = \frac{x_{si}^2 + y_{si}^2 - x_{si}x_a - y_{si}y_a}{\sqrt{x_{si}^2 + y_{si}^2} \cdot \sqrt{(x_{si} - x_a)^2 + (y_{si} - y_a)^2}}. \qquad (2.17)$$

And,

$$\cos \theta_a = \cos(\theta_{si} - \delta) = \cos \theta_{si} \cdot \cos \delta + \sin \theta_{si} \cdot \sin \delta. \qquad (2.18)$$

The line OS_i could be represented as:

$$y_{si} \cdot x - x_{si} \cdot y = 0. \qquad (2.19)$$

Then the distance from wire at (x_a, y_a) to line OS_i is:

$$h_a = \frac{|y_{si} \cdot x_a - x_{si} \cdot y_a|}{\sqrt{x_{si}^2 + y_{si}^2}}. \qquad (2.20)$$

Since wire position (x_a, y_a) is below the line OS_i, we could get $y_{si} \cdot x_a - x_{si} \cdot y_a > 0$, then (2.20) becomes:

$$h_a = \frac{y_{si} \cdot x_a - x_{si} \cdot y_a}{\sqrt{x_{si}^2 + y_{si}^2}}. \qquad (2.21)$$

Then, we could express $\sin \delta$ as:

$$\sin \delta = \frac{h_a}{L_{ia}} = \frac{y_{si} \cdot x_a - x_{si} \cdot y_a}{\sqrt{x_{si}^2 + y_{si}^2} \cdot \sqrt{(x_{si} - x_a)^2 + (y_{si} - y_a)^2}}. \qquad (2.22)$$

Substituting (2.17), (2.22) into (2.18), we could get:

$$\cos \theta_a = \frac{(x_{si}^2 + y_{si}^2 - x_{si}x_a - y_{si}y_a) \cdot \cos \theta_{si} + (y_{si} \cdot x_a - x_{si} \cdot y_a) \cdot \sin \theta_{si}}{\sqrt{x_{si}^2 + y_{si}^2} \cdot \sqrt{(x_{si} - x_a)^2 + (y_{si} - y_a)^2}}. \qquad (2.23)$$

By substituting (2.23) and (2.16) into (2.13) the voltage output of the i th sensor caused by the current I_a at position (x_a, y_a) can be expressed as:

$$V_{si} = g_{si} \cdot \frac{\mu_0}{2\pi} \cdot \frac{(x_{si}^2 + y_{si}^2 - x_{si}x_a - y_{si}y_a) \cdot \cos \theta_{si} + (y_{si} \cdot x_a - x_{si} \cdot y_a) \cdot \sin \theta_{si}}{\sqrt{x_{si}^2 + y_{si}^2} \cdot (x_{si} - x_a)^2 + (y_{si} - y_a)^2} \cdot I_a. \qquad (2.24)$$

The following equation holds:

$$(x_{si}^2 + y_{si}^2) \cdot \cos\theta_{si} = (x_{si}\cos\theta_{si} - y_{si}\sin\theta_{si}) \cdot x_{si} + (y_{si}\cos\theta_{si} + x_{si}\sin\theta_{si}) \cdot y_{si}. \tag{2.25}$$

Substituting (2.25) into (2.24) and reorganize we could get:

$$V_{si} = g_{si} \cdot \frac{\mu_0}{2\pi} \cdot I_a \cdot$$
$$\frac{(x_{si}\cos\theta_{si} - y_{si}\sin\theta_{si})(x_{si} - x_a) + (y_{si}\cos\theta_{si} + x_{si}\sin\theta_{si}) \cdot (y_{si} - y_a)}{\sqrt{x_{si}^2 + y_{si}^2} \cdot (x_{si} - x_a)^2 + (y_{si} - y_a)^2}. \tag{2.26}$$

For the case that the conductor is above line OS_i:

$$\cos\theta_a = \cos(\theta_{si} + \delta) = \cos\theta_{si} \cdot \cos\delta - \sin\theta_{si} \cdot \sin\delta. \tag{2.27}$$

Since point (x_a, y_a) is above the line, we have $y_{si} \cdot x_a - x_{si} \cdot y_a < 0$, then (2.20) becomes:

$$h_a = -\frac{y_{si} \cdot x_a - x_{si} \cdot y_a}{\sqrt{x_{si}^2 + y_{si}^2}}. \tag{2.28}$$

We could then express $\sin\delta$ as:

$$\sin\delta = \frac{h_a}{L_{ia}} = -\frac{y_{si} \cdot x_a - x_{si} \cdot y_a}{\sqrt{x_{si}^2 + y_{si}^2} \cdot \sqrt{(x_{si} - x_a)^2 + (y_{si} - y_a)^2}}. \tag{2.29}$$

Substituting (2.17), (2.29) into (2.18), we could get the same result as (2.23), which means (2.26) is a general expression of the magnetic field generated by a single current and detected by the i th sensor. The mathematical model of sensor output related to single wire current I_a at position (x_a, y_a) generated magnetic field could be expressed as:

$$V_{si} = g_{si} \cdot \frac{\mu_0}{2\pi r_{si}} \cdot \frac{p_i \cdot (x_{si} - x_a) + q_i \cdot (y_{si} - y_a)}{(x_{si} - x_a)^2 + (y_{si} - y_a)^2} \cdot I_a. \tag{2.30}$$

where, $p_i = x_{si}\cos\theta_{si} - y_{si}\sin\theta_{si}$, $q_i = y_{si}\cos\theta_{si} + x_{si}\sin\theta_{si}$ and $r_{si} = \sqrt{x_{si}^2 + y_{si}^2}$ are known parameters that can be calculated using known $x_{si}, y_{si}, \theta_{si}$. Thus, as shown in (2.30), the equation has three unknown variables x_a, y_a, I_a.

2.4.2 Magnetic Field Generated by Multi-Wire System

An *AC* current in a long straight wire generates a magnetic field around it according to the Biot-Savart law. The resultant magnetic field at the sensing position is proportional to the current magnitude and inversely proportional to the distance between the sensing point and wire position, on condition that the distance is much smaller than the wire length. The mixed magnetic field at a sensing point generated by multiple wires follows the superposition theory. The sensor parameters in terms of physical sensing position (x_{si}, y_{si}), measurement direction θ_{si} and gain factor of operation circuit g_{si} of the $i-$th sensor are known parameters. The relationship between sensor output voltages and wire currents can be expressed in matrix forms as follows:

$$\left[V_{si}\right]_{n_s \times 1} = \left[Z_{ij}\right]_{n_s \times 3} \times \left[I_{cj}\right]_{3 \times 1}. \tag{2.31}$$

In (2.31), the trans-impedance matrix $\left[Z_{ij}\right]_{n_s \times 3}$ is the key of current measurement, where the element Z_{ij} for the i-th sensor and j-th wire can be obtained based on sensor and wire geometrical parameters as shown in (2.32).

$$Z_{ij} = g_{si} \frac{\mu_0}{2\pi r_{si}} \frac{p_i \cdot (x_{si} - x_{cj}) + q_i \cdot (y_{si} - y_{cj})}{(x_{si} - x_{cj})^2 + (y_{si} - y_{cj})^2} \quad \forall i \in \mathbb{S}_s, \forall j \in \mathbb{S}_c. \tag{2.32}$$

where, $p_i = x_{si} \cos\theta_{si} - y_{si} \sin\theta_{si}$, $q_i = y_{si} \cos\theta_{si} + x_{si} \sin\theta_{si}$ and $r_{si} = \sqrt{x_{si}^2 + y_{si}^2}$. Then, the i-th sensor measurement is given by:

$$V_{si} = \sum_{j \in \mathbb{S}_c} Z_{ij} I_{cj}, \quad \forall i \in \mathbb{S}_s. \tag{2.33}$$

The equation shown in (2.31) is a high order nonlinear equation system with unknown variables $x_{cj}, y_{cj}, I_{cj}, \forall j \in \mathbb{S}_c$ to be solved and known sensor parameters $x_{si}, y_{si}, \theta_{si}, g_{si}, \forall i \in \mathbb{S}_s$. To solved the nonlinear equation system, the number of equations should be no less than the number of unknown variables as shown in (2.34). For the system that consists of three wires A, B and N, at least nine coil sensors are needed to solve (2.31).

$$n_s \geq 3 \times n_c. \tag{2.34}$$

2.4.3 Mixed Magnetic Field Decoupling

The trans-impedance matrix $\left[Z_{ij}\right]_{n_s\times3}$ is the key to build the relationship between sensor measurements and wire currents. The element Z_{ij} is only related to the sensor parameters $x_{si}, y_{si}, \theta_{si}, g_{si}$ and the wire geometrical positions x_{cj}, y_{cj}. The $i-$th sensor sensed mixed magnetic field V_{si} generated by the multiple wires is the sum of the magnetic field generated by the single wire (V_{sij}) as shown in (2.33).

Without solving the unknown wire positions x_{cj}, j_{cj}, the mixed magnetic field cannot be decoupled. And the wire currents also cannot be measured using the sensor measurements. After solving the wire positions from the nonlinear equation system, the trans-impedance matrix $\left[Z_{ij}\right]_{n_s\times3}$ can be built based on the identified wire positions and known sensor parameters. Real-time current measurement can then be achieved as:

$$\left[I_{cj}\right]_{3\times1} = \left[Z_{ij}\right]_{n_s\times3}^{-1} \times \left[V_{si}\right]_{n_s\times1} \tag{2.35}$$

where $\left[Z_{ij}\right]_{n_s\times3}^{-1}$ is the pseudo inverse of matrix $\left[Z_{ij}\right]_{n_s\times3}$.

As the trans-impedance matrix $\left[Z_{ij}\right]_{n_s\times3}$ depends only on the solved wire positions and known sensor parameters, it does not change unless the wire positions are changed or the sensing device is moved. After installing the sensing device and solving the unknown wire positions, the trans-impedance matrix can be built and taken as constant. The wire currents can be easily solved using the trans-impedance matrix as shown in (2.35). The mixed magnetic field can then be decoupled using the solved wire currents and the trans-impedance matrix as shown in (2.33). The key to measure the wire currents using the sensor measurements is to solve the unknown wire positions from the nonlinear equation system as shown in (2.31).

2.5 Summery

In this chapter, the North American home wiring including service entrance, home service panel, home appliance wiring and grounding system is investigated. There are two service entrance methods, overhead service entrance and underground service entrance. The service entrance conductor type, sizing, electric conduit, single-phase three-wire system, service transformer wiring and so on are presented in details. The whole North American home power supply system is modeled and the home grounding system is further investigated. The existence of home grounding current may lead to NEV problem, which is the main cause of stray voltage problem. The current return ratios of three residential homes are calculated using stray voltage monitor equipment. The sensing device design and implementation are presented. A manufacturing process is used to acquire the sensor electrical and geometrical parameters. The detailed model of sensed magnetic field generated by single wire current is derived. The model of mixed magnetic field generated by multiple wire currents can be expressed as a high-order nonlinear equation system. The trans-impedance matrix related to the wire positions and sensor parameters is the key to build the relationship between sensor measurements and wire currents. The trans-impedance matrix can be built using the solved wire positions, measure the wire currents through simple matrix operation and decouple the mixed magnetic field.

Chapter 3

Event-Based Current Measurement Method

3.1 Overview

This chapter presents a novel method for non-intrusive home current measurement using an array of magnetic field sensors. It is specifically designed for measuring the real-time currents on three wires, including two hot wires and one neutral wire, enclosed in the electric conduits of North American homes. The key idea is to extract information from appliance state changing events captured by sensor measurement changes. Since each detected event only corresponds to two wires between which the state-changing appliance is connected, the events can be clustered according to the wire connections. Wire position identification is formulated as an NLLS problem and is efficiently solved. Then, real-time current measurement is achieved by using the trans-impedance matrix built based on the solved wire positions and the sensor parameters obtained from the manufacturing process. The proposed method is evaluated by extensive laboratory and field tests.

Distinguished from the existing approaches, this work is particularly based on a unique observation of the service panels of North American homes, that is, among the three wires (i.e., two hot wires with $\pm 120V$ and the neutral wire), significant current changes caused by the state changes (i.e., turning on/off or varying operation modes) of individual appliances only occur on

two out of the three wires. This property enables us to extract the sensor measurements associated with each pair of two wires rather than all three wires, which greatly simplifies the non-intrusive home current measurement problem. Since the unbalanced load current returns to the service transformer through both neutral and ground wires via the neutral-ground bond at the service panel, the current unbalance ratio derived from the current return ratio concept in [24] is used to model the unequal current changes in two wires, when an appliance state changing event happens. Based on this model, we can detect the appliance state changing events through sensor measurement changes, and subsequently, cluster the events according to their wire connections by using cosine similarity as a distance index. Then, the positions of the three wires can be identified by formulating a NLLS problem, which is efficiently solved by the state-of-the-art NLP algorithm. For real-time measurement, the currents on the wires are calculated using the trans-impedance matrix established based on the wire position information and sensor parameters. Extensive mathematical analysis and experimental results indicate that, six sensors are sufficient for the proposed event-based non-intrusive home current measurement method, without the requirement of a dedicated on-site calibrator.

The flow chart of the proposed event-based non-intrusive home current measurement method is shown in Fig. 3.1. Appliance state changing events are detected to extract sensor measurements generated by the changed currents. The extracted events are further clustered using cosine similarity as difference index according to the different vector patterns of extracted sensor measurements, which correspond to different wire connections of the state changing appliances. In particular, a total of three types of events (E_{an}, E_{bn}, E_{ab}) can be clustered because appliances are connected between either $A - N$, $B - N$ or $A - B$. Unknown wire positions are solved based on NLLS optimization. After building trans-impedance matrix using the solved wire positions and calibrated sensor information to build the relationship between sensor measurements and wire currents, real-time current measurement is achieved by matrix computations.

This chapter is organized as follows. Section 3.2 describes the proposed event-based problem simplification idea using home appliance state changing events. The event detection and clustering methods using sensor measure-

ments are presented in Section 3.3. The wire position identification process formulated as a nonlinear least square based optimization method is shown in Section 3.4. Then real-time current measurement could be achieved by building the trans-impedance matrix. And finally Section 3.5 gives a summary of the whole chapter.
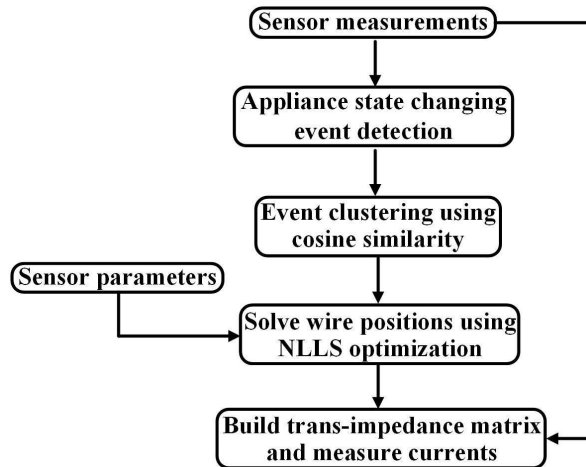
Figure 3.1: Flow chart of the proposed event-based non-intrusive home current measurement method.

3.2 Event-Based Problem Simplification

3.2.1 Home Appliance State Changing Events

Most of the home appliances like microwave oven, induction cooker, fan, electric kettle and so on are connected through electric sockets to $120V$ voltage source. Some high-power appliances like kitchen stove, air conditioner, refrigerator and so on need $240V$ voltage to operate. An $120V$ voltage powered appliance is connected between either $A - N$ or $B - N$, while a $240V$ powered appliance is connected between $A - B$. Due to the neutral-ground bond at the service panel, the unbalanced load current I_u returns to the service transformer through either the neutral wire (with current I_n) or the grounding branch (with current I_g). A current return ratio $K = \Delta I_n / \Delta I_u$ is defined in [24] as shown in Subsection 2.2.3 and can be used to characterize the difference between neutral and load currents. Since K is a function of the network

impedance parameters and could vary if the impedance parameters change, a general variable called current unbalance ratio ($g_k^{e_k}$) is used to represent the inequality of the changed two wire currents when an appliance state change happens.

If the operating state of an appliance changes while the states of other appliances stay unchanged, only the currents of the two wires between which the appliance is connected can change, while the current of the remaining wire keeps constant. For example, as shown in Fig. 3.2, if the electric kettle connected between $A - N$ is turned on, I_a and I_n change by ΔI_{an} and $-\Delta I_{an} + \Delta I_g$, respectively, while I_b stays unchanged ($\Delta I_b = 0$). Similarly, if the fan connected between $B - N$ is turned on, I_b and I_n change by ΔI_{bn} and $-\Delta I_{bn} + \Delta I_g$, respectively, while I_a stays unchanged ($\Delta I_a = 0$). On the other hand, for the state change of an appliance connected between $A - B$, the changed currents are equal in magnitudes ($\Delta I_a = -\Delta I_b = \Delta I_{ab}$) while the neutral current stays unchanged $\Delta I_n = 0$.
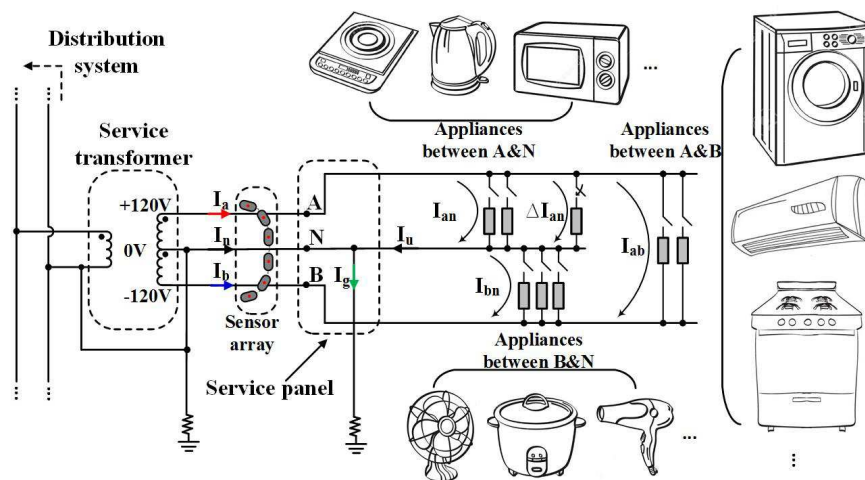
Figure 3.2: Home appliance wire connections and state changing.

The currents measured of laboratory test Case 7 using four Fluke i1000s accurate current clamps are shown in Fig. 3.3. We could see that the features of home appliance state changing as presented above hold and are later used to simplify the non-intrusive home current measurement problem.
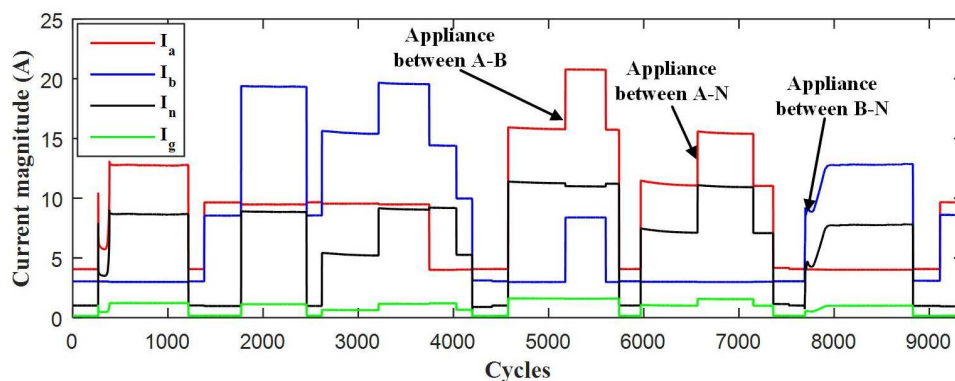
Figure 3.3: CT measured currents of laboratory test Case 7.

3.2.2 Simplification using Extracted Events

As discussed in previous chapters, the trans-impedance matrix $\left[Z_{ij} \right]_{n_s \times 3}$ is the key to build the relationship between sensor measurements and wire currents. However, it consists of unknown wire position variables that need to be determined. The nonlinear equation system of a multi-wire system is shown in (2.31). A total of nine unknown variables including wire positions (x_a, y_a), (x_b, y_b), (x_n, y_n) and wire currents I_a, I_b, I_n need to be solved using sensor measurements V_{si} ($i \in \mathbb{S}_s$). Thus, in existing approaches, at least nine sensors are used to solve the nonlinear equation system [19]. However, by detecting the appliance state changing events and subtracting the sensor measurements at the pre-event and post-event points as shown in (3.1), the changed sensor measurements generated only by the changed appliance currents flowing through two of the three wires can be extracted as shown in (3.2).

$$\left[\Delta V_{si} \right]_{n_s \times 1} = \left[V_{si}^{post} \right]_{n_s \times 1} - \left[V_{si}^{pre} \right]_{n_s \times 1} \tag{3.1}$$

$$= \left[Z_{ij} \right]_{n_s \times 3} \times \left(\left[I_{cj}^{post} \right]_{3 \times 1} - \left[I_{cj}^{pre} \right]_{3 \times 1} \right). \tag{3.2}$$

Take a state changing appliance connected between $A - N$ as an example (e.g., the turn-on event of an electric kettle as described in Subsection 3.2.1 . As shown in Fig. 3.4, phase B current I_b has no impact on the extracted sensor measurements since $\Delta I_b = 0$. Mathematically, for the state changing event of an appliance connected between $A - N$ (denoted by e_{an}), we have

$$\left[\Delta V_{si}^{e_{an}}\right]_{n_s \times 1} = \left[Z_{ij}\right]_{n_s \times 3} \times \begin{bmatrix} \Delta I_{an}^{e_{an}} \\ 0 \\ -\Delta I_{an}^{e_{an}} + \Delta I_{g}^{e_{an}} \end{bmatrix}$$

$$= \left[Z_{ij}\right]_{n_s \times 3} \times \begin{bmatrix} \Delta I_{an}^{e_{an}} \\ 0 \\ -g_{an}^{e_{an}} \times \Delta I_{an}^{e_{an}} \end{bmatrix}. \tag{3.3}$$
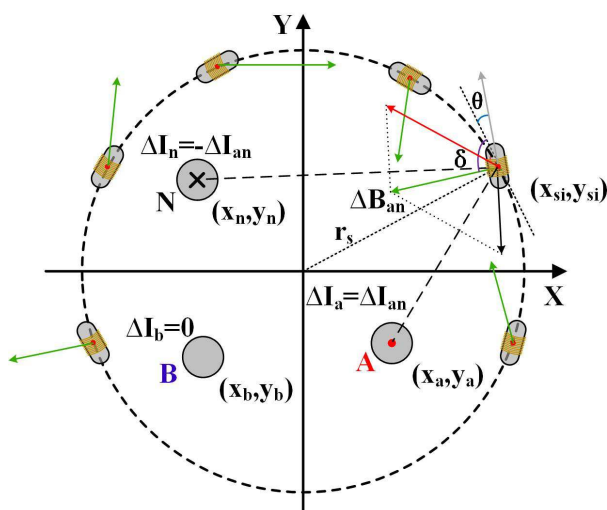
Figure 3.4: Magnetic fields generated by the two wires of an event.

Since each appliance can be connected between either $A - N$, $B - N$, or $A - B$, a total of three types of events can be extracted. Note that the event clustering process proposed in Subsection 3.3 does not assume the wires to which the appliances are connected, since such information is unknown for the non-intrusive home current measurement, i.e., which two of the three wires the appliances are connected cannot be identified through the sensor measurements. However, the events connected between different two wires can be clustered into different types. Besides, the current return ratio (K) may vary slightly when the network impedance parameters change. Although the current return ratio of a home is relatively stable, it can change if the power supply network changes. Therefore, we define a general variable called the current unbalance ratio $g_k^{e_k}, k \in \mathbb{S}_T, e_k \in \mathbb{S}_{E_k}$ to characterize the inequality between neutral and load current changes. The ratio is an unknown variable for

each event and needs to be determined. In general, we have $g_{an}^{e_{an}} \approx g_{bn}^{e_{bn}} \neq 1$ and $g_{ab}^{e_{ab}} \approx 1$ if the changes of network impedance parameters are not significant. The corresponding sensor measurement changes for the three types of events are given by

$$\left[\Delta V_{si}^{e_{an}}\right]_{n_s \times 1} = \left[Z_{ia}, \; -Z_{in}\right]_{n_s \times 2} \times \begin{bmatrix} \Delta I_{an}^{e_{an}} \\ g_{an}^{e_{an}} \times \Delta I_{an}^{e_{an}} \end{bmatrix} \qquad (3.4)$$

$$\left[\Delta V_{si}^{e_{bn}}\right]_{n_s \times 1} = \left[Z_{ib}, \; -Z_{in}\right]_{n_s \times 2} \times \begin{bmatrix} \Delta I_{bn}^{e_{bn}} \\ g_{bn}^{e_{bn}} \times \Delta I_{bn}^{e_{bn}} \end{bmatrix} \qquad (3.5)$$

$$\left[\Delta V_{si}^{e_{ab}}\right]_{n_s \times 1} = \left[Z_{ia}, \; -Z_{ib}\right]_{n_s \times 2} \times \begin{bmatrix} \Delta I_{ab}^{e_{ab}} \\ g_{ab}^{e_{ab}} \times \Delta I_{ab}^{e_{ab}} \end{bmatrix} \qquad (3.6)$$

where $e_{an} \in \mathbb{S}_{E_{an}}$, $e_{bn} \in \mathbb{S}_{E_{bn}}$ and $e_{ab} \in \mathbb{S}_{E_{ab}}$.

As we can see, by extracting appliance state changing events, the equations are greatly simplified and only consist of six unknown variables each. For example, the equation of an event happening between $A - N$ (corresponding to (3.4)) consists of six unknown variables: x_{ca}, y_{ca}, x_{cn}, y_{cn}, $\Delta I_{an}^{e_{an}}$ and $g_{an}^{e_{an}}$. Also, according to (3.3), the extracted sensor measurements of the same type of events are linearly dependent, since the current changes happen on the same set of two wires. For example, denoting the two events happening between $A - N$ as e_{an} and e'_{an}, respectively, we have

$$\left[\Delta V_{si}^{e_{an}}\right]_{n_s \times 1} = \gamma \left[\Delta V_{si}^{e'_{an}}\right]_{n_s \times 1}, \; \forall e_{an}, e'_{an} \in \mathbb{S}_{E_{an}}. \qquad (3.7)$$

where the coefficient γ is a (positive or negative) real number and is given by

$$\gamma = \Delta I_{an}^{e_{an}} / \Delta I_{an}^{e'_{an}}. \qquad (3.8)$$

To establish the trans-impedance matrix $\left[Z_{ij}\right]_{n_s \times 3}$, at least two linearly independent events need to be detected to calculate the wire positions. Any two of the three types of events are linearly independent as shown in (3.9).

$$\text{rank} \begin{bmatrix} \Delta I_{an}^{e_{an}} & 0 & \Delta I_{ab}^{e_{ab}} \\ 0 & \Delta I_{bn}^{e_{bn}} & -g_{ab}^{e_{ab}} \times \Delta I_{ab}^{e_{ab}} \\ -g_{an}^{e_{an}} \times \Delta I_{an}^{e_{an}} & -g_{bn}^{e_{bn}} \times \Delta I_{bn}^{e_{bn}} & 0 \end{bmatrix} = 2. \qquad (3.9)$$

The unknown wire positions hold the key to build the relationship between sensor measurements and wire currents. Evolutionary computation method together with a total of ten coil sensors are used to solve the nonlinear equation system. A more effective way to obtain the wire positions is to solve the combined equation system which consists of different types of events. The number of effective observations provided by sensor measurements should be no less than the number of unknown variables based on the principle of least square [28]. Denote the number of linearly independent event types as n_d. In total, there are six unknown variables of wire positions (i.e., (x_a, y_a), (x_b, y_b) and (x_n, y_n)) need to be determined. Each type of linearly independent event can provide a number of n_s effective observations, i.e., a total of $n_d \times n_s$ effective observations. Since each type of event adds two more unknown current variables (i.e., ΔI_k and g_k, respectively), we have

$$n_d \times n_s \geq 2 \times n_d + 6. \tag{3.10}$$

Dividing both sides of (3.10) by n_d, the minimum number of sensors needed to solve the problem is given by

$$n_s \geq 2 + \frac{6}{n_d} = 5, \text{ if } n_d = 2. \tag{3.11}$$

Thus, if at least two types of events are extracted, five sensors are needed to solve the equation system. Considering the sensor measurement errors, one redundant sensor is added to achieve better measurement accuracy. Therefore, a total of six sensors are installed in the sensing device. To solve the nonlinear equation system of a two-wire system, at least six sensors are needed since there are four unknown wire position variables and two unknown current variables. However, using the event-based problem simplification, the same number of sensors could solve the nonlinear equation system of the North American home three-wire system with one more sensor redundancy. Besides, a less number of sensors means less device cost, less solving algorithm computational complexity, less requirement for the DAQ system and more stable sensing device.

3.3 Event Detection and Clustering

3.3.1 Event Detection using Sensor Measurements

The trans-impedance matrix $\left[Z_{ij}\right]_{n_s \times 3}$ depends only on the wire positions and sensor parameters and keeps constant if the wire and sensing device are not moved. Due to the linearity between sensor measurements and wire currents according to (3.7), appliance state changing events will cause the change of sensor measurements. An example of sensor measurements corresponding to the measured currents as shown in Fig. 3.3 based on laboratory experiments is shown in Fig. 3.5. We could see that the sensor measurements varies with the wire currents when an appliance is turn on or off. The goal is to extract appliance state changing events that related to only two of the three wires using the recorded sensor measurements to simplify the current measurement problem as described in Subsection 3.2.2. To extract the changed sensor measurements related to the appliance state changing events, only the state changing events and the starting and the ending points of them need to be detected. Although some of the appliance types can also be detected using some specific signatures of different appliances similar to non-intrusive load monitoring (NILM) [27], for example, the 3rd harmonic, starting and ending pattern, duration and so on, we only need to extract the appliance state changing events using sensor measurements.
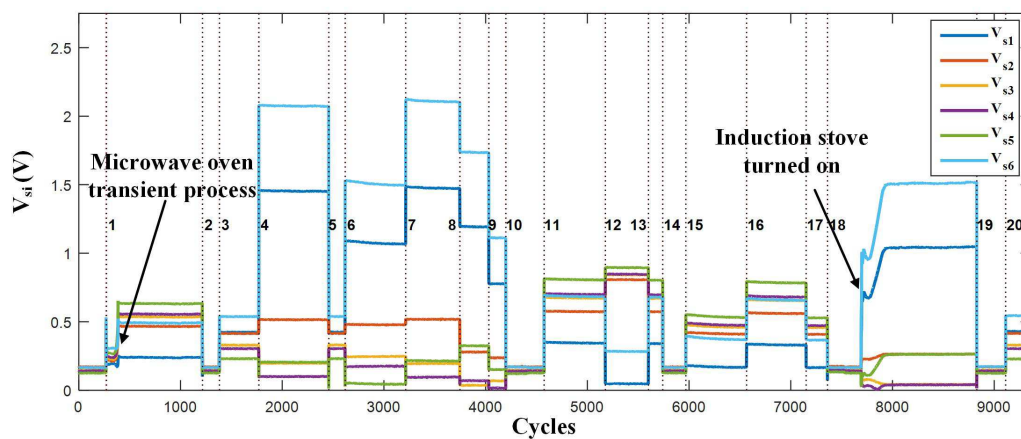
Figure 3.5: Sensor measurement rms values of laboratory test Case 7.
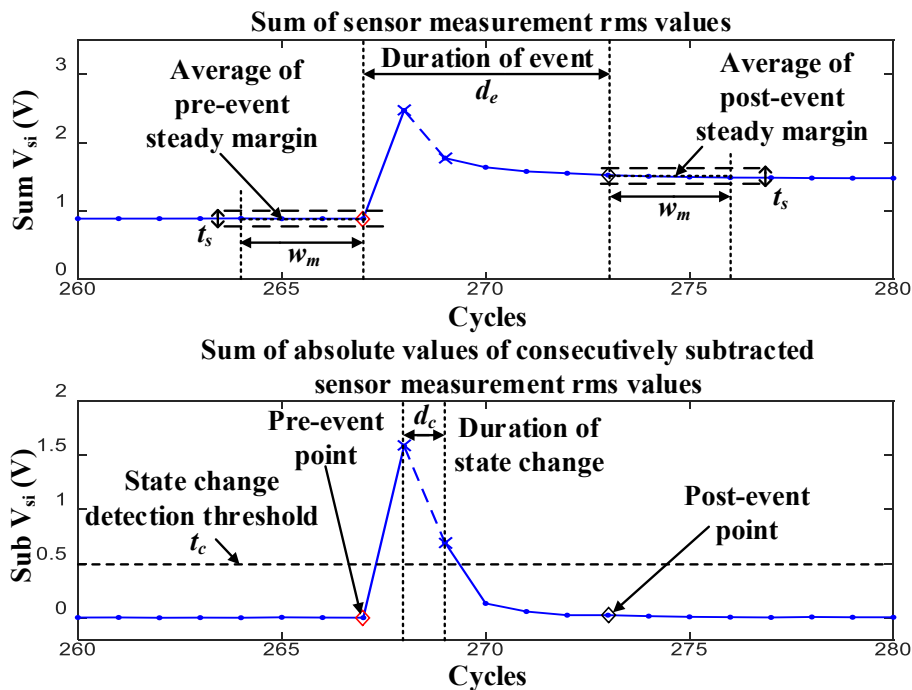
Figure 3.6: An illustration of the event detection method.

An illustration of the event detection method is shown in Fig. 3.6. The sum of the absolute values of consecutively subtracted sensor measurement rms values $Sub\ V_{si}$ as shown in (3.12) are used to detect appliance state changing duration. If there is no appliance state changing event happens, the wire currents remain constant and so as the sensor measurements. Therefore, the sum of absolute values of consecutively subtracted sensor measurement rms values $Sub\ V_{si} \approx 0$ when there is no appliance state changing event happens. However, when an appliance is turned on or off, the wire currents and the sensor measurements will change accordingly, which in turn will cause $Sub\ V_{si}$ to increase dramatically in very short time. The sum of the sensor measurement rms values as shown in (3.13) is used to confirm whether an appliance state changing event happens and determine the event duration.

$$Sub\ V_{si}\ (p) = \sum_{i \in \mathbb{S}_s} ||V_{si}\ (p+1)| - |V_{si}\ (p)||. \qquad (3.12)$$

$$Sum\ V_{si}\ (p) = \sum_{i \in \mathbb{S}_s} |V_{si}\ (p)|. \tag{3.13}$$

With the determined event duration, the changed sensor measurements generated only by the state changing appliance are extracted by subtracting the sensor measurements at pre-event and post-event points. Specifically, if the sum of absolute values of consecutively subtracted sensor measurements rms values $Sub\ V_{si}$ is above the state changing detection threshold t_c, it is considered as a potential event and the duration of state changing d_c is determined by all the consecutively points that are above t_c. The pre-event and post-event steady margins with w_m cycles width constraint are determined if the sum of all the sensor measurement rms values $Sum\ V_{si}$ among the margins are within t_s limit of their average value. The pre-event and post-point points are the last and first data points of the determined steady margins, respectively.

To confirm if an event actually occurs but not some small variations of the sensor measurements, the difference between the sum of the sensor measurement rms values at pre-event and post-event data points $Dif\ V_{si}$ are calculated. The event is only recorded if the difference is greater than a pre-specified threshold t_d considering the impact of sensor measurement noise and appliance current fluctuations. If we use the difference of $Sum\ V_{si}$ between pre-event and post-event points to determine if an event happens or not, we could meet the situation that although an event happens the difference of $Sum\ Vsi$ is small and the event may not be extracted. The length of the event duration is limited with d_e cycles, i.e., the width difference between the pre-event and post-event data points is limited within d_e cycles.

$$Dif\ V_{si} = \sum_{i \in \mathbb{S}_s} ||V_{si,post-event}| - |V_{si,pre-event}||. \tag{3.14}$$

Using the above event detection method, the unstable, small or long-lasting appliance state changing events will no be extracted. An example of the event detection results is shown in Fig. 3.5. As we can see, a total of 20 events are extracted in around nine thousand-cycle recorded sensor measurement data. The determined pre-event and post-event data points along with the sum of sensor measurement rms values and the sum of absolute values of consecutively

subtracted sensor measurement rms values of recorded sensor measurement data are shown in Fig. 3.7. Here, the transient process of microwave oven and the turn-on event of the induction stove are not extracted due to their unstable and long-lasting state changes. All the other appliance state changing events are extracted, with their IDs given in Fig. 3.5.
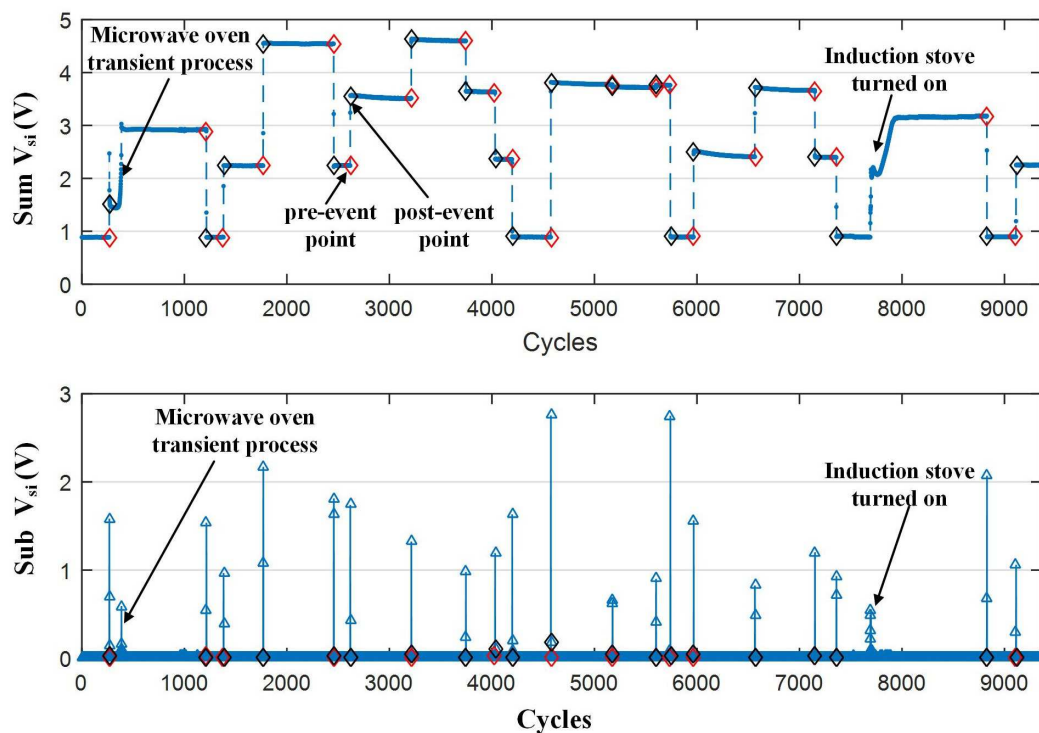
Figure 3.7: Event detection results of laboratory test Case 7.

The parameters used for event detection method as discussed above are shown in Table 3.1. The parameter setting is validated through extensive laboratory and field tests to be effective.

Table 3.1: Event detection method parameters.

Event detection	
t_d	0.5 V
t_c	0.05 V
t_s	1 %
w_m	3 cycles
d_e	8 cycles

3.3.2 Event Clustering using Cosine Similarity

Using the event detection method discussed in Subsection 3.3.1, the appliance state changing events can be extracted by subtracting the data measured at pre-event and post-event data points. The extracted appliance state changing events IDs are shown in Fig. 3.8. Based on our analysis in (3.7) and (3.8) the extracted sensor measurements ΔV_{si} of the same type of events should be linearly dependent and share the same or opposite phase directions. In particular, if two events are of the same type, the coefficient γ in (3.8) is a positive or negative real number. The extracted sensor measurements ΔV_{si} of two different appliance state changing events happen at different two of the three wires should be linearly independent, which means different sensor measurement patterns of ΔV_{si} exist for different types of events. However, the sensor operation circuits may not be exactly the same, which means the phase shifts of the operation circuits can be slightly different. Besides, the power supply system frequency may not be exactly 60 Hz, which in turn will cause the phase angles of the wire currents and the sensor measurements to continuously shift. For example, the same turn-on events of an appliance may have different phase angles of the extracted wire currents and the sensor measurements caused by the phase shift problem. Thus, it is necessary to synchronize ΔV_{si} in order to eliminate the effect of the phase shift problem.
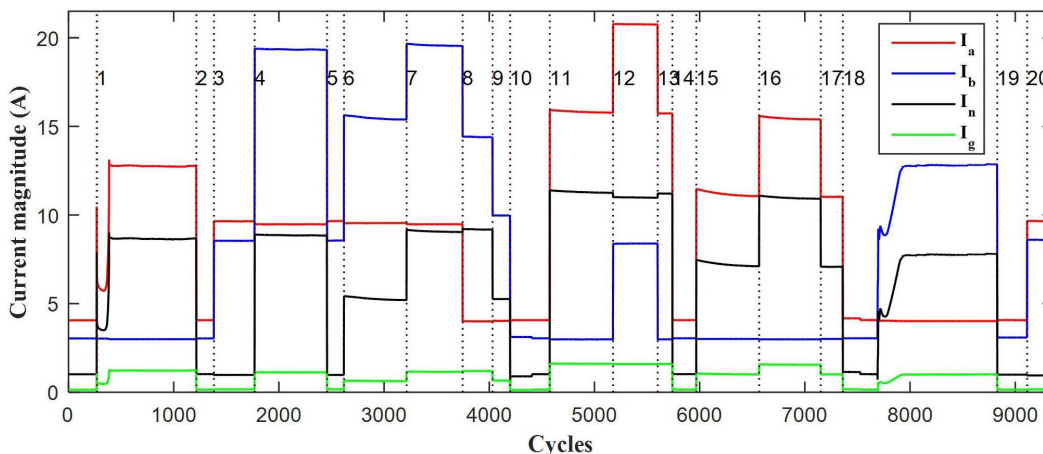
Figure 3.8: Detected events IDs of laboratory test Case 7.

The changed currents in phasor domain of the event 5 in laboratory test Case 7 are shown in Fig. 3.9. We could see that this state changing event happens between $B - N$, the changed current in A is almost zero and a small portion of changed neutral current flows to the ground as discussed in Subsection 2.2.3. The changed current phase angles of B and N are opposite and the changed current phase angles of N and G are the same. However, we cannot tell if the appliance is turn on or off since the wire current phase angles continuously change due to phase shift problem caused by power frequency changes.
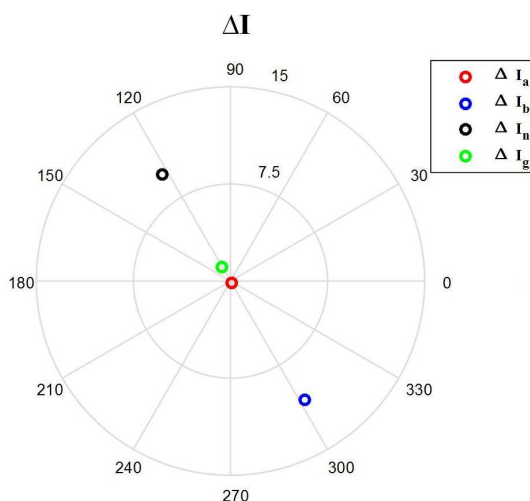
Figure 3.9: Changed currents of laboratory test Case 7 (event 5).

The corresponding changed sensor measurements of the event 5 in laboratory test Case 7 are shown in Fig. 3.10. We could see that the phase angles of the sensor measurements are nearly the same as the current phase angles but with small differences due to the small differences among the sensor operation circuits. Specifically, the sensor measurement of an event with largest magnitude is selected to be the reference vector and is assigned with $0°$ or $180°$ phase angle depending on whether the pre-synchronized phase angle is less than $180°$ or not. The remaining sensor measurements are synchronized to the reference vector with the same or opposite phase angles and unchanged magnitudes.
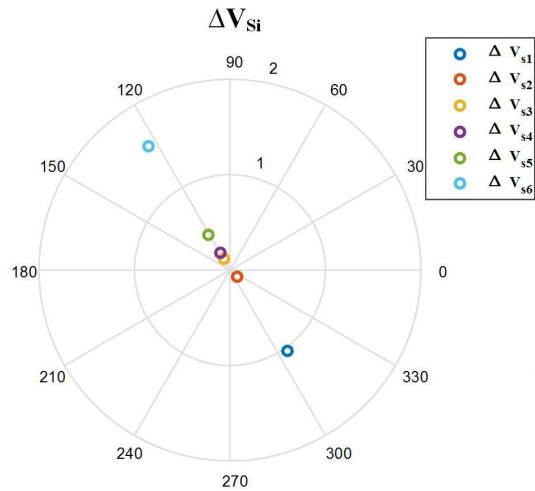
Figure 3.10: Changed sensor measurements of laboratory test Case 7 (event 5).

As the processes discussed above, the 6−th sensor measurement ΔV_{s6} of event 5 in laboratory test Case 7 is selected to be the reference vector since its magnitude is the largest compared with the rest of the sensor measurements and assigned with 0° phase angle since the pre-synchronized ΔV_{s6} phase angle is less than 180°. The rest of the changed sensor measurements are then synchronized to the reference vector with result shown in Fig. 3.11.
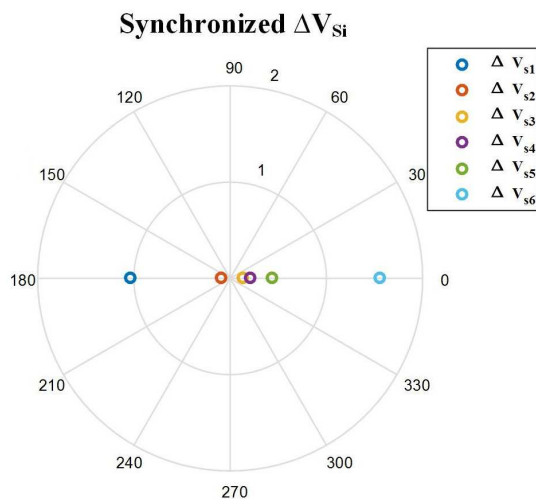
Figure 3.11: Synchronized changed sensor measurements of laboratory test Case 7 (event 5).

For different types of events, the patterns of extracted sensor measurements ΔV_{si} are different, which could be used to differentiate events of different types. The extracted sensor measurements of three representative events of three types are shown in Fig. 3.12. We could see that the three representative sensor measurement patterns are different between each other. The goal of event clustering is to classify the extracted sensor measurements of events into different groups using the distinctive patterns of different types of events.
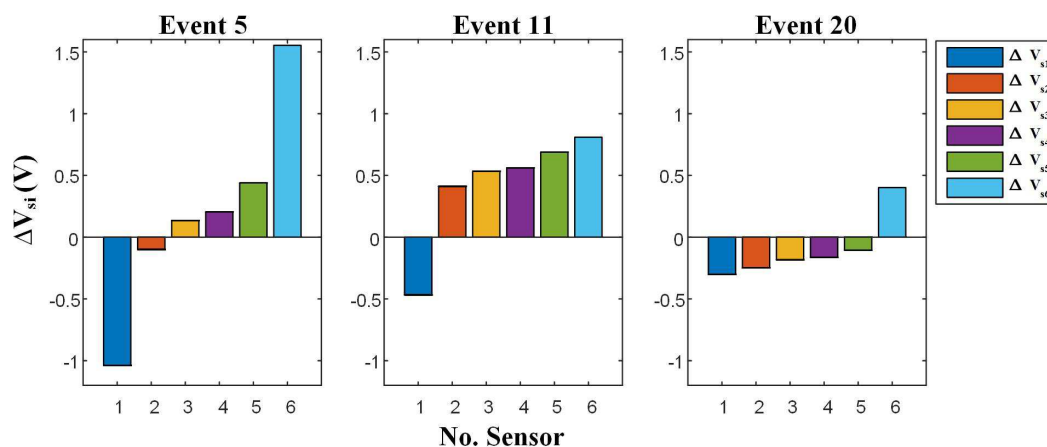
Figure 3.12: Extracted sensor measurement patterns of different events.

The three representative events shown in Fig. 3.12 happen between $B - N$, $A - N$ and $A - B$, respectively, with the changed current magnitudes shown in Fig. 3.13. We could see that when an event happens between one of the two hot wires and the neutral wire, i.e., between $A - N$ or $B - N$, the changed current magnitudes are not equal with a portion of the neutral current flows through the ground wire due to the neutral-ground bond at the service panel. The changed current magnitudes of events that happen between two hot wires, i.e., between $A - B$ are equal. However, the extracted sensor measurement patterns can only differentiate events happening between different two wires but can not allocate the events to exactly which two of the three wires. Thus, we can only cluster the extracted sensor measurements of events into three types but cannot know exactly which event happens between which two of the three electric wires.
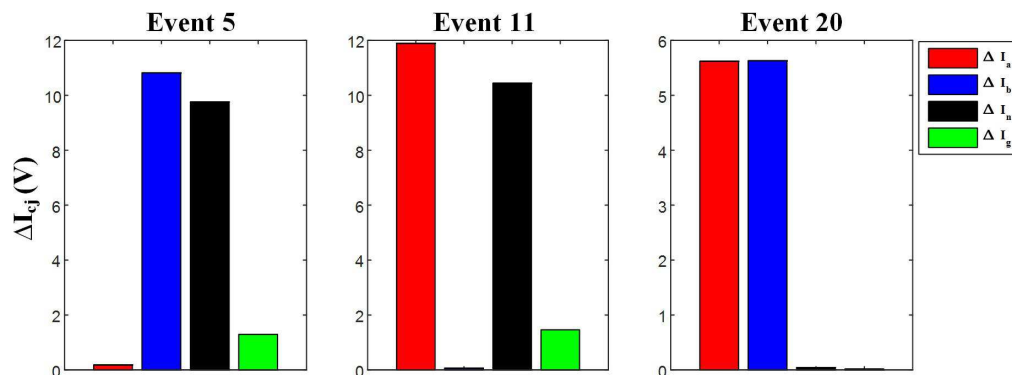
Figure 3.13: Changed currents of different events.

Therefore, the extracted sensor measurements generated by appliances connected between the same two of the three wires should be clustered as on type of events. The extracted sensor measurements generated by appliances connected between different two wires should be differentiated. Cosine similarity measures the similarity between two vectors according to the angle between them. Given two vectors of attributes, P and Q, the cosine similarity $\cos(\theta)$, is represented using a dot product and magnitudes as

$$similarity = \cos(\theta) = \frac{P \cdot Q}{||P|| \, ||Q||} = \left| \frac{\sum_{i=1}^{n} P_i Q_i}{\sqrt{\sum_{i=1}^{n} (P_i)^2} \sqrt{\sum_{i=1}^{n} (Q_i)^2}} \right|. \qquad (3.15)$$

The resulting similarity ranges from -1 meaning exactly opposite, to 1 meaning exactly the same, with 0 indicating orthogonality (decorrelation), and in-between values indicating intermediate similarity or dissimilarity. An illustration of cosine similarity is shown in Fig. 3.14. The cosine similarity $\cos(\theta_{V_{T1,e1}, V_{T1,e2}})$ between vectors $V_{T1,e1}$ and $V_{T1,e2}$ equals to 1, which means the two vectors share the same direction. The cosine similarity $\cos(\theta_{V_{T2,e1}, V_{T2,e2}})$ between vectors $V_{T2,e1}$ and $V_{T2,e1}$ is -1 since the directions of the two vectors are opposite. One property of cosine similarity is that the cosine similarities of two opposite vectors and another vector are equal in magnitudes. For example, the cosine similarity $\cos(\theta_{V_{T2,e1}, V_{T3,e1}})$ between vectors $V_{T2,e1}$ and $V_{T3,e1}$

and the cosine similarity $\cos(\theta_{V_{T2,e2},V_{T3,e1}})$ between vectors $V_{T2,e2}$ and $V_{T3,e1}$ are equal in magnitudes, i.e., $\cos(\theta_{V_{T2,e1},V_{T3,e1}}) + \cos(\theta_{V_{T2,e2},V_{T3,e1}}) = 0$.
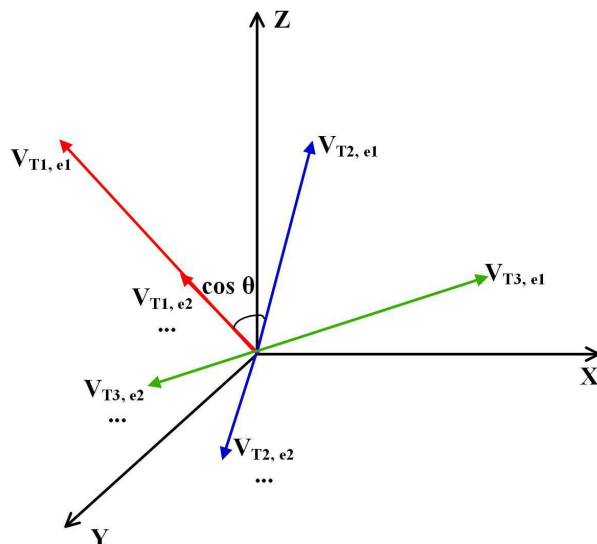
Figure 3.14: Illustration of cosine similarity.

The cosine similarity is well suited for the event clustering task if we take the extracted sensor measurements of an event as a vector. However, due to the fact that the turn on and off events of the appliances connected between the same two wires could lead to opposite current and sensor measurement phase angles and the phase shift problem cause by the unstable power frequency, the extracted sensor measurements generated by appliances connected between the same two wires could have opposite directions similar to the two vectors $V_{T2,e1}$ and $V_{T2,e2}$ as shown in Fig. 3.14. Besides, the extracted sensor measurements of appliances connected between the same two wires are linear dependent but could have different magnitudes since the changed currents can be different as shown in (3.7) and (3.8) similar to the two vectors $V_{T1,e1}$ and $V_{T1,e2}$. Thus, the extracted sensor measurement vectors of appliances connected between the same two wires share the same or opposite directions with magnitudes in proportion to the changed current magnitudes, i.e., the cosine similarity equals to 1 or -1. For the extracted sensor measurement vectors of events happening between different two of the three wires, the space angles are not $0°$ or $180°$, leading to the cosine similarity not equal to 1 or -1.

Considering fact that the angles between the extracted sensor measurement vectors of the events happening between the same two wires could be the same or opposite, the absolute value of cosine similarity is used as the degree to cluster the extracted events. Consider two arbitrary events e and e', the cosine similarity degree between them is given by

$$D_{e,e'} = \left| \frac{\sum\limits_{i \in \mathbb{S}_s} \Delta V_{si}^e \Delta V_{si}^{e'}}{\sqrt{\sum\limits_{i \in \mathbb{S}_s} (\Delta V_{si}^e)^2} \sqrt{\sum\limits_{i \in \mathbb{S}_s} (\Delta V_{si}^{e'})^2}} \right|, \ \forall e, e' \in \mathbb{S}_E \qquad (3.16)$$

where $\mathbb{S}_E = \mathbb{S}_{E_{an}} \cup \mathbb{S}_{E_{bn}} \cup \mathbb{S}_{E_{ab}}$ is the set of all events. For two events with the same type, the cosine similarity between them should be close to 1. Take two events happening between $A - N$ (e_{an} and e'_{an}) as an example. By substituting (3.7) and (3.8) into (3.16), we have

$$D_{e_{an},e'_{an}} = \left| \gamma / \sqrt{\gamma^2} \right| = 1, \ e_{an}, e'_{an} \in \mathbb{S}_{E_{an}}. \qquad (3.17)$$

On the other hand, the cosine similarity degree between two events with different types are not close to 1. Therefore, a total of three groups of events can be clustered by using cosine similarity. An example is shown in Fig. 3.15 based on the sensor measurements in Fig. 3.5. We could see that a total of 20 events are correctly clustered in to three types with $\{e_5, e_4, e_{19}, e_6, e_{10}, e_7, e_9\}$ as type S_{E_1}, $\{e_{11}, e_{14}, e_2, e_{15}, e_{18}, e_{16}, e_{17}, e_1\}$ as type S_{E_2} and $\{e_{20}, e_3, e_{13}, e_{12}, e_8, \}$ as type S_{E_3} compared with current measurement as shown in Fig. 3.8. Worth mentioning, the reason why S_{E_1}, S_{E_2} and S_{E_3} are used to represent the clustered groups not $S_{E_{an}}$, $S_{E_{bn}}$, $S_{E_{ab}}$ is that the extracted sensor measurements generated by an appliance is connected between which two of the three wires is unknown. The events of the same type are further sorted with a descending order of the sum of the absolute values of the extracted sensor measurements $\sum_{i \in \mathbb{S}_s} |\Delta V_{si}|$. The events with larger current changes will get higher priority for later wire position identification as the extracted sensor measurements with large magnitudes are considered to be measured more accurately compared with events with smaller extracted sensor measurement magnitudes.
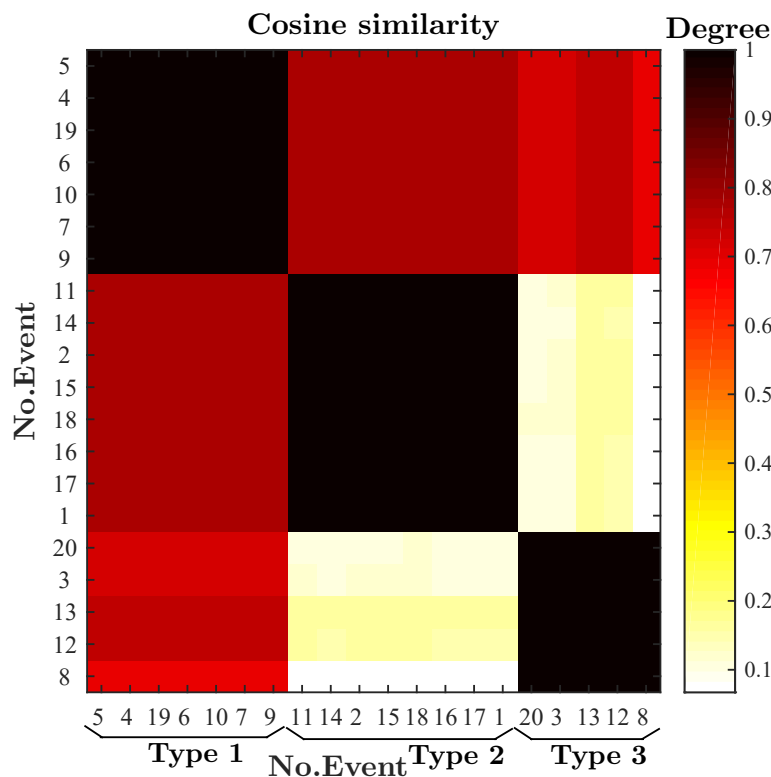
Figure 3.15: Event clustering of extracted events.

3.4 Wire Position Identification

3.4.1 Nonlinear Least Square Optimization Problem

The trans-impedance matrix $\left[Z_{ij}\right]_{n_s \times 3}$ between sensor measurements and wire currents is critical for real-time current measurement. However, $\left[Z_{ij}\right]_{n_s \times 3}$ consists of unknown wire positions. To achieve non-intrusive current measurement, the unknown wire positions need to be determined. The high-order nonlinear nonconvex equation system as shown in (2.31) can be used to solve the unknown wire positions directly. However, it requires at least a total of nine sensors. After the event detection and clustering process as described in Subsection 3.3.1 and Subsection 3.3.2, the equation systems consist of three different types of events can be got as shown in (3.4), (3.5) and (3.6). Solving each of the equation system requires at least a total of six sensors and could

only get two of the three wire positions at one time. Besides, due to the sensor measurement errors, the left and right sides of the high-order nonlinear equation system are actually not equal. Traditional high-order nonlinear equation system solving method like Newton Raphson method, Trust-region method and so on are not suitable for the wire position solving task.

A more effective way to solve the unknown wire positions is to build the combined equation system consisting of different types of events. As shown in (3.11), a total of five sensors are sufficient to solve the equation system. The wire positions solving task is modelled as an NLLS optimization problem, which minimizes the least square value between extracted sensor measurements ($\Delta V_{si}^{e_k}$) and calculated sensor measurements ($\Delta V_{bi}^{e_k}$) as shown in (3.18), where $\mathbb{S}_T = \{E_{an}, E_{bn}, E_{ab}\}$ is the set of event types.

$$\min \sum_{i \in \mathbb{S}_S, k \in \mathbb{S}_T, e_k \in \mathbb{S}_{E_k}} \left(\Delta V_{si}^{e_k} - \Delta V_{bi}^{e_k}\right)^2. \tag{3.18}$$

The calculated sensor measurements for different types of events $\Delta V_{bi}^{e_k}$ ($k \in \mathbb{S}_T$) are obtained in (3.19), (3.20) and (3.21), respectively. The changed current $\Delta I_k^{e_k}$ and current unbalance ratio $g_k^{e_k}$ of events are unknown variables to be solved. The current unbalance ratios $g_{ab}^{e_{ab}}$ for extracted sensor measurements of appliances connected between $A - B$ are 1 since $\Delta I_a^{e_{ab}} = \Delta I_b^{e_{ab}}$. However, which two of the three wires are connected cannot be determined using the extracted sensor measurement patterns. Thus, the current unbalance ratio $g_k^{e_k}$ is taken as an variable for all of the extracted events. The nine unknown wire position variables $x_a, y_a, x_b, y_b, x_n, y_n$ are included in the tans-impedance matrix elements Z_{ij} as shown in (2.32).

$$\Delta V_{bi}^{e_{an}} = (Z_{ia} - g_{an}^{e_{an}} \times Z_{in})\Delta I_{an}^{e_{an}}, \forall e_{an} \in \mathbb{S}_{E_{an}}, \forall i \in \mathbb{S}_s. \tag{3.19}$$

$$\Delta V_{bi}^{e_{bn}} = (Z_{ib} - g_{bn}^{e_{bn}} \times Z_{in})\Delta I_{bn}^{e_{bn}}, \forall e_{bn} \in \mathbb{S}_{E_{bn}}, \forall i \in \mathbb{S}_s. \tag{3.20}$$

$$\Delta V_{bi}^{e_{ab}} = (Z_{ia} - g_{ab}^{e_{ab}} \times Z_{ib})\Delta I_{ab}^{e_{ab}}, \forall e_{ab} \in \mathbb{S}_{E_{ab}}, \forall i \in \mathbb{S}_s. \tag{3.21}$$

To achieve better identification performance, several electrical and geometrical constraints are added. In particular, the wire coordinates are limited by the physical size of the electric conduit (r_c) and wire (r_w) as shown in (3.22) since the wire centers are less than the electric conduit radius minus the wire radius.

$$\sqrt{(x_{cj})^2 + (y_{cj})^2} \leq r_c - r_w, \forall j \in \mathbb{S}_c. \tag{3.22}$$

The distance between any two wires should be no less than the wire diameter $2r_w$ and smaller than the subtraction of wire diameter from electric conduit diameter $2r_c$ as shown in (3.23).

$$2r_w \leq \sqrt{(x_{cj_1} - x_{cj_2})^2 + (y_{cj_1} - y_{cj_2})^2} \leq 2r_c - 2r_w, \forall j_1, j_2 \in \mathbb{S}_c, j_1 \neq j_2. \tag{3.23}$$

The magnitudes of changed currents are limited by the maximum current of home appliances (ΔI_{max}) as shown in (3.24).

$$|\Delta I_k^{e_k}| \leq \Delta I_{max}, \forall k \in \mathbb{S}_T, \forall e_k \in \mathbb{S}_{E_k}. \tag{3.24}$$

The boundary of the calculated sensor measurements ΔV_{bi} is given by the voltage range of the operation circuits (V_{op}) as show in (3.25).

$$|\Delta V_{bi}^{e_k}| \leq V_{op}, \forall i \in \mathbb{S}_s, \forall k \in \mathbb{S}_T, \forall e_k \in \mathbb{S}_{E_k}. \tag{3.25}$$

The current unbalance ratio $g_k^{e_k}$ is a positive number with an upper bound g_{max} as shown in (3.26).

$$0 < g_k^{e_k} < g_{max}, \forall k \in \mathbb{S}_T, \forall e_k \in \mathbb{S}_{E_k}. \tag{3.26}$$

The wire positions solving task is formulated as an NLLS problem with optimization goal as shown in (3.18) and electrical and geometrical constraints from (3.19) to (3.26).

3.4.2 Solving Wire Positions

The wire position identification problem formulated in Subsection 3.4.1 is non-linear and nonconvex in nature. To solve this problem in a more effective way, we use AMPL to formulate the problem and then, apply KNITRO to solve it.[28]. A PC configured with a 2.40-GHz Intel Core i7-4700MQ CPU and 8GB RAM is used for the wire position identification. The NLLS parameters of the constraints are shown in Table 2.1. Depending on the test wire types, the wire radius limit r_w is set to be 1.8 mm if aluminum bars are used as electric wires and 3 mm if electric service wires are used. A total of 12 events out of the 20 extracted events, with 4 for each type, are used to solve NLLS optimization.

Table 3.2: NLLS parameters.

NLLS	
r_c	18 mm
r_w	1.8 or 3 mm
V_{op}	9 V
ΔI_{max}	20 A
g_{max}	5

An example of the wire positions solved in laboratory experiments are shown in Fig. 3.16 and are compared with the reference positions. The solved wire positions are $(-0.82, -13.5)$, $(7.6, -14.2)$ and $(0, -8.2)$ mm and the reference wire positions are $(0, -8)$, $(-8, -13.9)$ and $(8, 13.9)$ mm. Since which two of the three wires are connected for the extracted events is unknown, which solved wire position is A, B or N is also unknown. The three solved wire positions are compared with the reference ones with geometrical errors 0.2, 0.36 and 0.49 mm, respectively. We could see that the solved wire positions are accurate since there may also exist small errors for the reference wire positions. In the process of solving the wire positions, the unknown event currents are also solved although they are not useful for the real-time current measurement process. The solved event currents are compared with the extracted event currents as shown in Fig. 3.17.
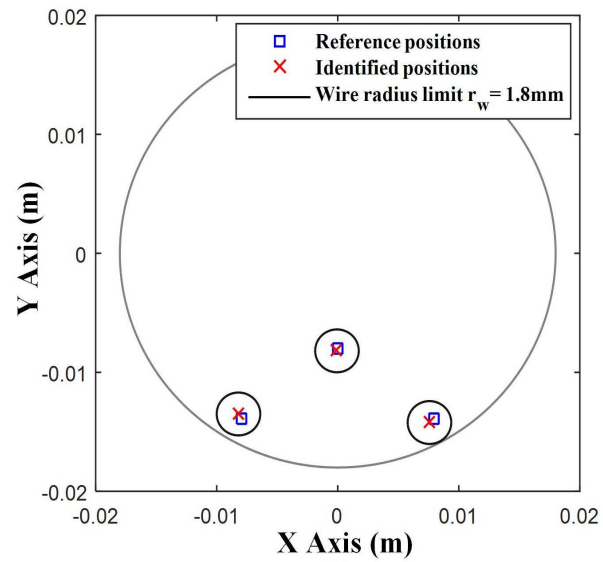
Figure 3.16: Solved wire positions of laboratory test Case 7.
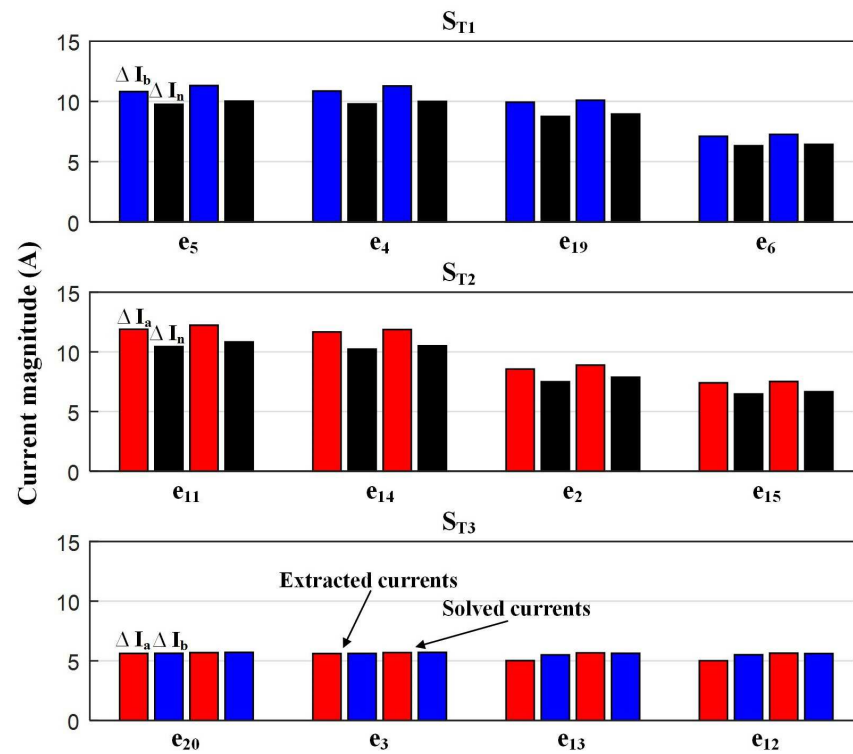
Figure 3.17: Solved event currents of laboratory test Case 7.

The relative errors of solved event currents are shown in Table 3.3. We could see that most of the event currents are solved within 5% relative error. The two event e_{13} and e_{12} are solved with around 10% relative errors, which is caused by the small saturation of the A current clamp since the maximum measurement peak current is 20A.

Table 3.3: Solved event currents accuracy of laboratory test Case 7.

S_{T1}			S_{T2}			S_{T3}		
ID	$\Delta I_b(\%)$	$\Delta I_n(\%)$	ID	$\Delta I_a(\%)$	$\Delta I_n(\%)$	ID	$\Delta I_a(\%)$	$\Delta I_b(\%)$
5	4.6	2.7	11	2.8	3.8	20	1.2	1.4
4	3.9	2.1	14	1.8	2.8	3	1.4	1.6
19	1.8	2.3	2	3.9	5.0	13	13.1	2.3
6	2.2	1.7	15	1.5	2.9	12	12.5	1.9

3.4.3 Real-Time Current measurement

After solving the unknown wire positions from the NLLS optimization problem. The solved wire positions together with the sensor electrical and geometrical parameters are used to build the trans-impedance matrix $\left[Z_{ij}\right]_{n_s \times 3}$ between sensor measurements and wire currents. Based on the calculated trans-impedance matrix $\left[Z_{ij}\right]_{n_s \times 3}$, real-time currents are obtained by matrix computation (2.35). The calculated currents are compared with the CT measured reference currents as shown in Fig. 3.18. The absolute current measurement errors are shown in Fig. 3.19. The average current measurement absolute errors are 0.39A, 0.25A and 0.22A for for A, B and N, respectively. As we can see, the absolute errors are below 1A. The average relative errors of the three measured wire currents are 4.55%, 3.25% and 6.54% for A, B and N, respectively. Since the current clamp itself could bring 1% relative measurement errors and could saturate when measured current peak value is over 20A, satisfactory and accurate current measurement result is achieve as the relative errors of the two hot wires of the worst laboratory Case 7 are within 5%. Due to the small magnitude of the neutral current, the relative error is slightly larger than 5%.
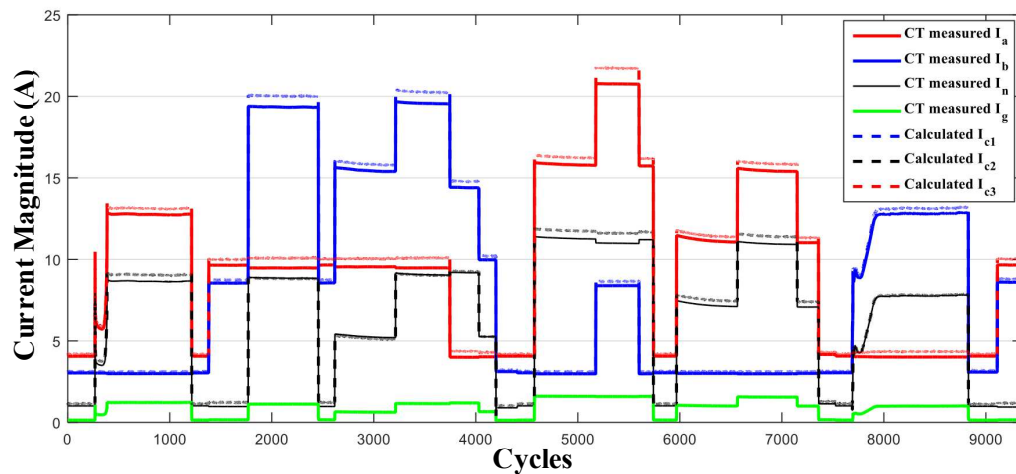
Figure 3.18: Current measurement results of laboratory test Case 7.
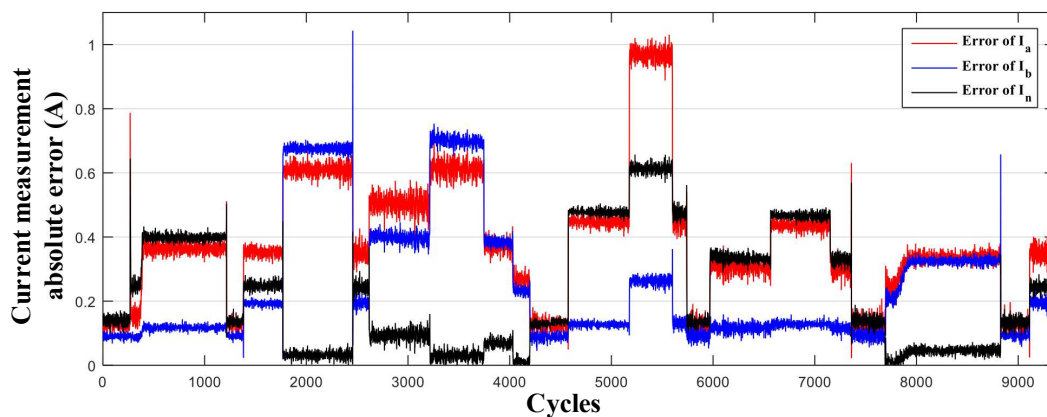
Figure 3.19: Absolute errors of measured currents for laboratory test Case 7.

3.5 Summary

The proposed event-based current measurement method for North American homes is presented in this chapter. Based on the unique observations of the North American homes, the non-intrusive home current measurement problem can be greatly simplified using the appliance state changing events. Only six coil sensors are installed in the sensing device to capture the mixed magnetic fields generated by the three wires after simplifying the problem using the properties of appliance state changing events. The small number of coil sensors

can reduce the sensing device cost, the computational complexity of the wire position solving algorithm and the requirement of the data acquisition system.

Using the appliance state changing event detection method, the sensor measurements that correspond to only two of the three wires that the appliances are connected can be extracted. The extracted sensor measurements are then clustered into three types using cosine similarity since the appliances can be connected between either two of the three wires. The wire position identification is formulated as an NLLS problem with geometrical and electrical constraints added to achieve better optimization results. The NLLS problems is formulated in AMPL using KNITRO as solver to solve the three wire positions. Then, real-time current measurement can be achieved by simple matrix computation with the trans-impedance matrix built using the solved wire positions and known sensor parameters. The laboratory test Case 7 is used as an example to show the whole event-based home current measurement processes.

Chapter 4

Experimental Results

4.1 Overview

This chapter shows the experimental results of the proposed event-based non-intrusive home current measurement method. The proposed event-based home current measurement method together with the sensing device have been validated by extensive laboratory experiments and field tests. The laboratory experiments are shown in Section 4.2. The laboratory experiment test bed design and implementation are presented. A total of two types of conductors are used in laboratory experiments to test the proposed method. The first one uses Aluminum bars as wires inserted in a 3D printed wire holder with reference wire positions. The second type of laboratory experiment uses electric service wires to further validate the method. Real home appliances and the resistive box are used to generate the appliance state changing events. The field test results are shown in Section 4.3. The sensing device is installed at the overhead service entrance point of a residential house in Edmonton, AB, Canada and the whole sensing system is validated in the double-blind test. The customer turned on and off the home appliances randomly and the first 10-min recorded sensor measurement data is used to fulfill the event detection, event clustering and wire positions solving task. Then the currents are measured in real time and compared with the CT measured reference currents for hours. Extensive laboratory and field test results show that the proposed method can achieve accurate real-time non-intrusive home current measurement. A summary of this chapter is given in Section 4.4.

4.2 Laboratory Experiments

4.2.1 Laboratory Experiment Test Bed

The designed and implemented laboratory experiment test bed is illustrated in Fig. 3.1. Two $120V$ 3-phase power sources are used to supply power to the appliances used. The same two phases (A) of the power sources are connected to two transformers connected in series to generate $+120V$, $-120V$ and $0V$ voltages same as the single-phase three-wire North American home power supply system. The neutral wire and a much longer ground wire are connected to the connecting point of the two transformers and bonded at the service transformer so that part of the unbalanced current will flow through the ground wire back to the transformers. The two hot wires are connected to the rest ports of the two transformers respectively. The maximum phase current is limited by the transformer capacity (20A). The currents I_a, I_b, I_n and I_g are measured using Fluke i1000s accurate current clamps as reference values.

Some commonly used home appliances such as microwave oven, induction stove, electric fan, electric kettle and so on are connected to the $120V$ voltages and an adjustable resistive load is connected to the $240V$ voltage instead of the high-power electric appliances like stove, air conditioner and refrigerator. Load changes are accomplished by turning on and off the appliances. Since some appliances have different operation mode, the currents also vary when the operation mode changes. The sensing device and current clamps are connected to the NI-DAQ instrument through BNC connectors. The sensor measurements and reference currents are acquired by the NI-DAQ instrument and continuously recorded by a laptop using LabVIEW data acquisition software. The first type of laboratory test uses long and straight Aluminum bars as wires inserted in a 3D printed wire holder with known reference hole coordinates to validate the correctness of the solved wire positions. The second type of laboratory test uses real electric service wires with unknown reference positions to further test the proposed method.
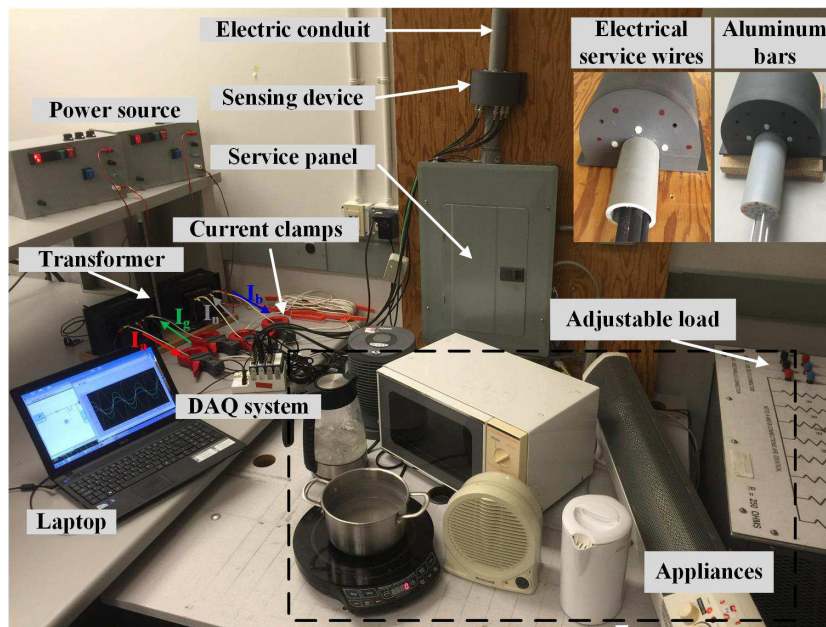
Figure 4.1: Laboratory experiment test bed.

4.2.2 Aluminum Bar Test

The first type of laboratory experiment uses three Aluminum bars as wires inserted in a 3D printed wire holder with a total of 21 known reference wire positions as shown in Fig. 4.2. The sensor parameters x_s, y_s, θ_s and g_s used are shown in Table 2.2, while the parameters used for event detection and solving NLLS are shown in Table 3.1 and Table 3.2, respectively. The aim of using ideal Aluminum bars as wires is to compare the solved wire positions with the reference ones so as to validate the correctness of the wire position solving algorithm.

A total of 15 cases with different wire positions and real appliances are tested. The average current of the 15 cases are $I_a \approx 9A$, $I_b \approx 7.5A$ and $I_n \approx 6A$, respectively. A total of 12 events, with 4 for each type, are used for all the cases to solve the NLLS optimization problem to obtain the wire positions. On average, the wire positions are solved in 0.1750 second CPU time using the state-of-art NPL algorithm formulated in AMPL with KNITRO as solver.
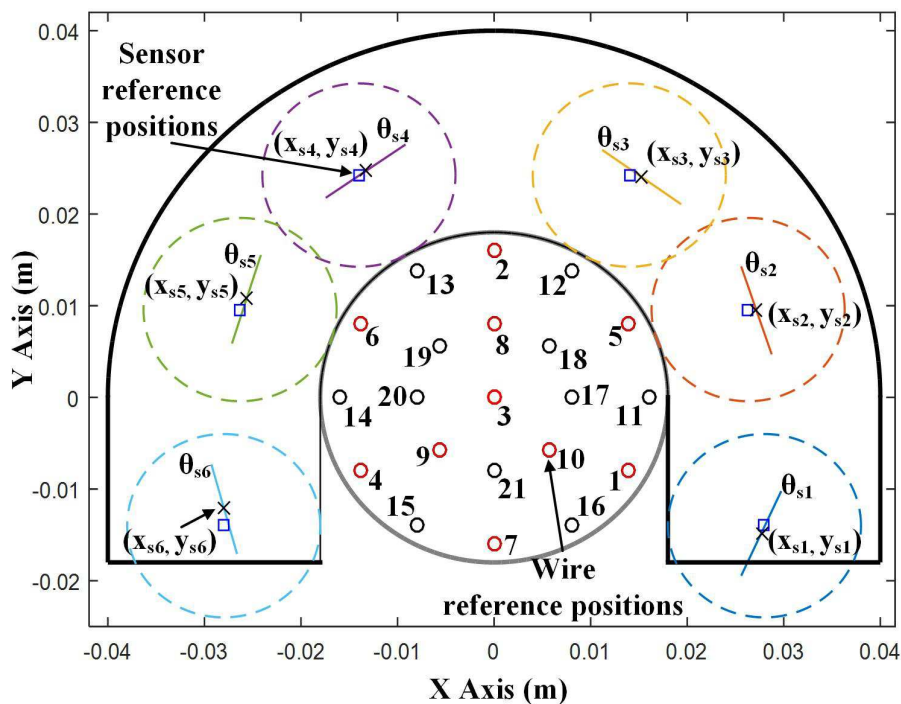
Figure 4.2: Layout of laboratory experiment using Aluminum bars.

The laboratory experiment test Case 7 is used to illustrate the proposed event-based non-intrusive home current measurement method in Chapter 3. The wire positions solved of laboratory experiment test Case 7 as an example are compared with the reference wire positions as shown in Fig. 3.16. This case (i.e., Case 7) corresponds to the worst case we found during the laboratory experiments (with the largest measurement errors). The three wires are gathered with positions $A - 21$, $B - 15$ and $N - 16$ as defined in Fig. 4.2. We can see that, even for the this worst case, the wire positions are solved with high accuracy within $0.5mm$ geometrical errors. Based on the solved wire positions, real-time currents are obtained by matrix computation. The calculated currents are compared with the reference currents in Fig. 3.18. The absolute current measurement errors are shown in Fig. 3.19. As we can see, the absolute errors are below $1A$ even though the current clamp of A is saturated a little when the current is over $20A$.

The accuracy of the current measurement results of all the 15 cases in laboratory experiments is show in Table 4.1. The average absolute errors of measured currents are within $0.2A$ for most of the cases, and the average relative errors for the two hot wire currents I_a and I_b are within 4% in general. Due to smaller magnitude, I_n is measured with higher but less than 8% average relative error. All the laboratory experiment results indicate that accurate current measurements can be achieved by the proposed method for various combinations of wire positions.

Table 4.1: The accuracy of current measurements of laboratory experiment using Aluminum bars.

Cases	Positions	Absolute Error (A)			Relative Error %		
		I_a	I_b	I_n	I_a	I_b	I_n
1	$8, 9, 10$	0.13	0.09	0.12	1.38	1.41	1.87
2	$3, 7, 1$	0.11	0.10	0.18	1.29	1.29	3.35
3	$2, 6, 1$	0.05	0.03	0.04	0.87	0.72	1.50
4	$2, 3, 5$	0.13	0.11	0.15	1.46	1.18	2.61
5	$4, 2, 1$	0.13	0.07	0.06	1.42	1.18	1.70
6	$3, 15, 16$	0.07	0.11	0.16	0.86	1.34	4.12
7	$21, 15, 16$	0.39	0.25	0.22	4.55	3.24	6.54
8	$4, 9, 1$	0.06	0.09	0.11	0.87	2.19	2.15
9	$17, 15, 16$	0.05	0.05	0.12	0.65	1.11	3.57
10	$10, 20, 15$	0.15	0.15	0.13	1.69	1.87	2.59
11	$17, 21, 16$	0.24	0.24	0.17	2.71	3.90	7.27
12	$14, 19, 9$	0.10	0.09	0.19	1.07	1.23	5.78
13	$15, 19, 10$	0.08	0.09	0.16	0.91	1.12	5.73
14	$19, 2, 18$	0.27	0.15	0.14	2.97	2.33	7.16
15	$18, 9, 16$	0.06	0.10	0.03	0.80	1.56	1.19

4.2.3　Electrical Service Wire Test

The second type of laboratory experiment uses electric service wires connected to the service panel as conductors. The same parameters used for event detection method and solving NLLS are used. A number of 12 extracted events, with 4 for each type are used to solve the wire positions. The solved wire position of the four representative cases are shown in Fig. 4.3. The solved wire currents of Case 1 are compared with the reference ones as shown in Fig. 4.4.
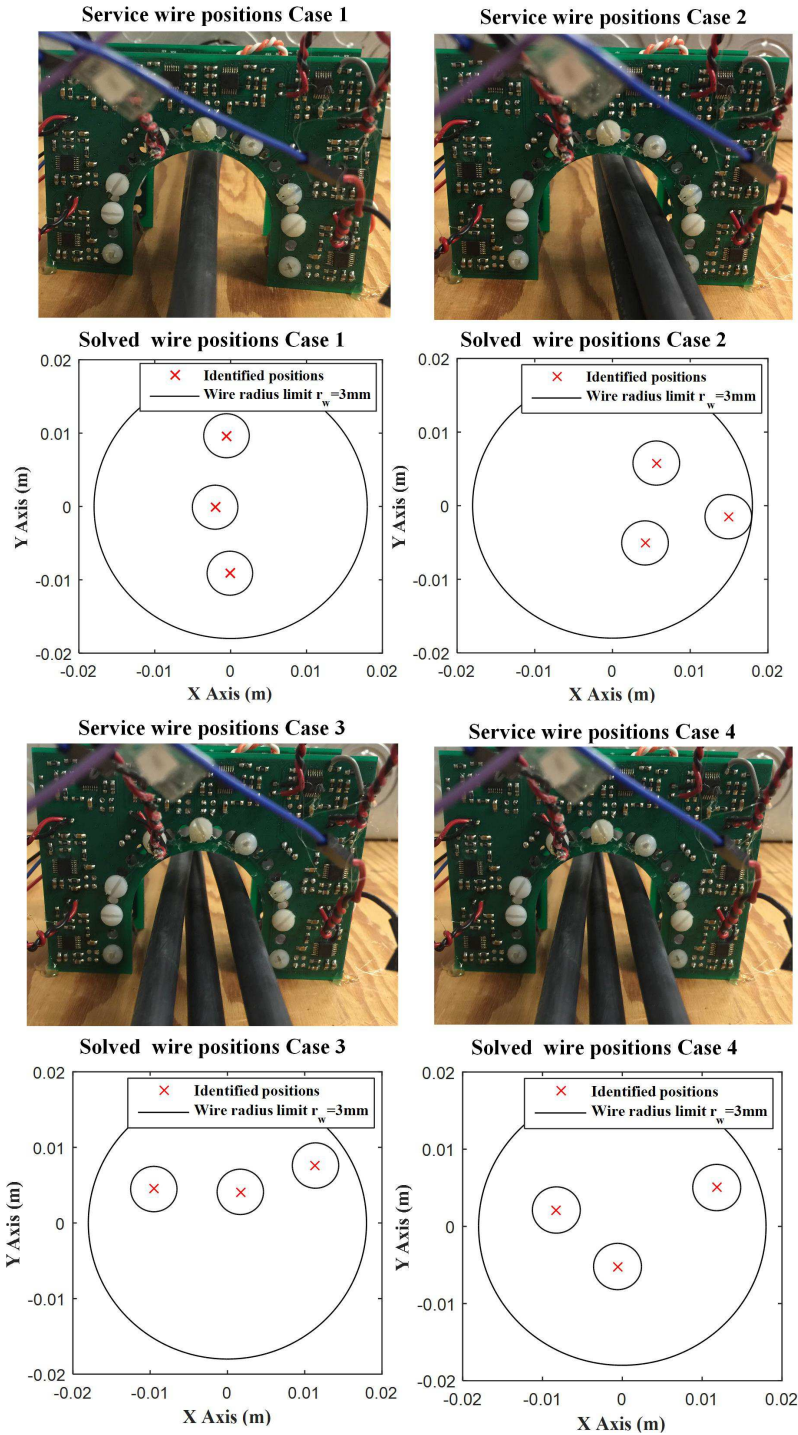
Figure 4.3: Service wire positions and solved wire positions of representative cases in laboratory experiment.
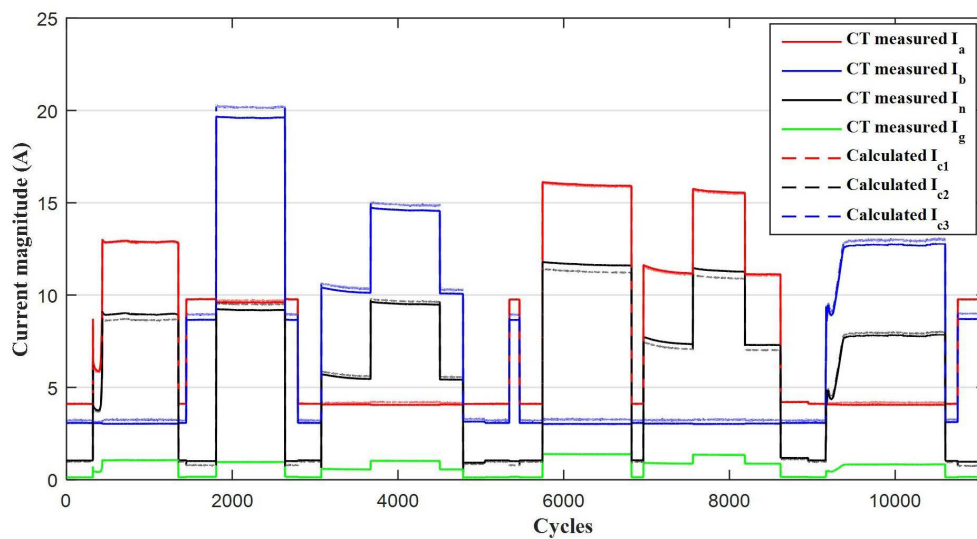
Figure 4.4: Current measurement results of electric service wire test Case 1.

The accuracy of the current measurement results of the 4 representative cases in laboratory experiment using electric service wires is shown in Table 4.2. Due to the fact that the electric service wires are not ideally straight as the Aluminum bar, the measurement errors are slightly larger than the measurement results using Aluminum bars as wires. However, due to the rigidness of the electric service wires, the degree of the wire curvature is too small to have a big impact on the measurement accuracy. We could see that the average absolute errors of the measured three phase currents are within $0.5A$ and most of the cases are solved within 5% relative errors for the two hot wires. Due to the smaller magnitude, the neutral current is solved with larger but within 8% relative errors.

Table 4.2: The accuracy of current measurements of laboratory experiment using electric service wires.

Cases	Absolute Error (A)			Relative Error %		
	I_a	I_b	I_n	I_a	I_b	I_n
1	0.07	0.24	0.21	1.21	4.43	5.41
2	0.05	0.07	0.11	0.88	1.18	3.06
3	0.24	0.28	0.28	2.53	3.87	5.24
4	0.50	0.34	0.35	5.59	3.46	7.49

4.3 Field Tests

4.3.1 Sensing System Installation

To further validate the proposed event-based non-intrusive home current measurement method, the sensing system is installed and tested at a residential house at Edmonton, AB, Canada. The field test is conducted with the sensing device installed at the over head service entrance point as shown in Fig. 4.5 (a). The sensing device is powered using a $12V$ portable battery and the sensor measurements are captured using NI DAQ system and recorded in a PC with LabVIEW data acquisition software. Due to the limited installation space and the potential interference problem generated by the wires around the service panel, the overhead service entrance point is taken as a better installation spot than the incoming conduit of the home service panel. The reference values of currents are measured using three Fluke i1000s accurate current clamps in the home main service panel as shown in Fig. 4.5 (b). Since more than one grounding wires exist at the home service panel, the ground wire current is not measured using CT. The reference currents are recorded using another NI data DAQ instrument and recorded using another PC.
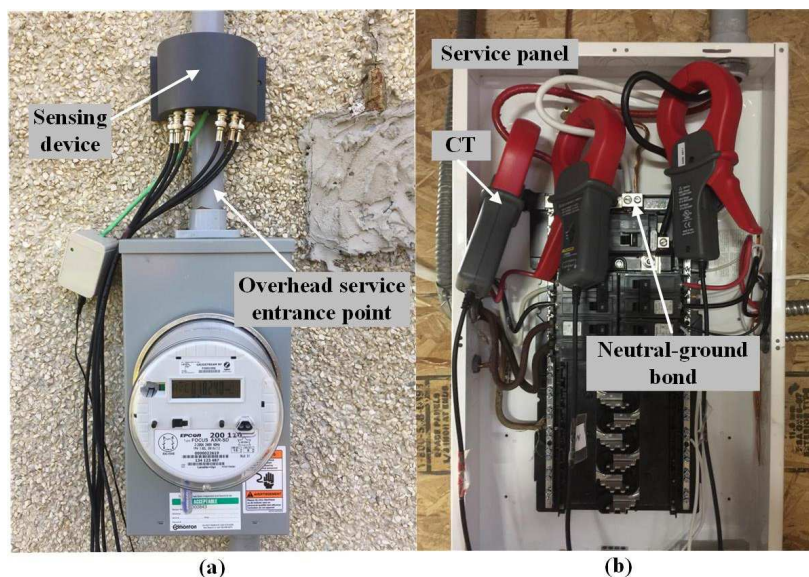
Figure 4.5: Field test installation: (a) Sensing device at overhead service entrance point; (b) Reference currents measured by CTs at service panel.

4.3.2 Current Measurement Results

The sensor measurements and CT measured currents are recorded using two NI DAQ systems cycle by cycle with resolution 256 points per cycle. Since there are multiple ground wires from the home service panel to the ground rod, only the two hot wire and neutral wire currents are measured. The customer turned on and off the home appliances randomly to generate the appliance state changing events. A 10−min long sensor measurement data is recorded and the 60 Hz component is used for event detection, event clustering and solving wire positions. The extracted appliance state changing events IDs are labeled as shown in Fig. 4.6. A total of 18 appliance stage changing events are extracted in 10 minutes. We could see from the figure that due to the sensor measurement fluctuations caused by some magnetic field interferences, some of the appliance state changing events are not extracted since the event detection method only extract stable sensor measurement changes.
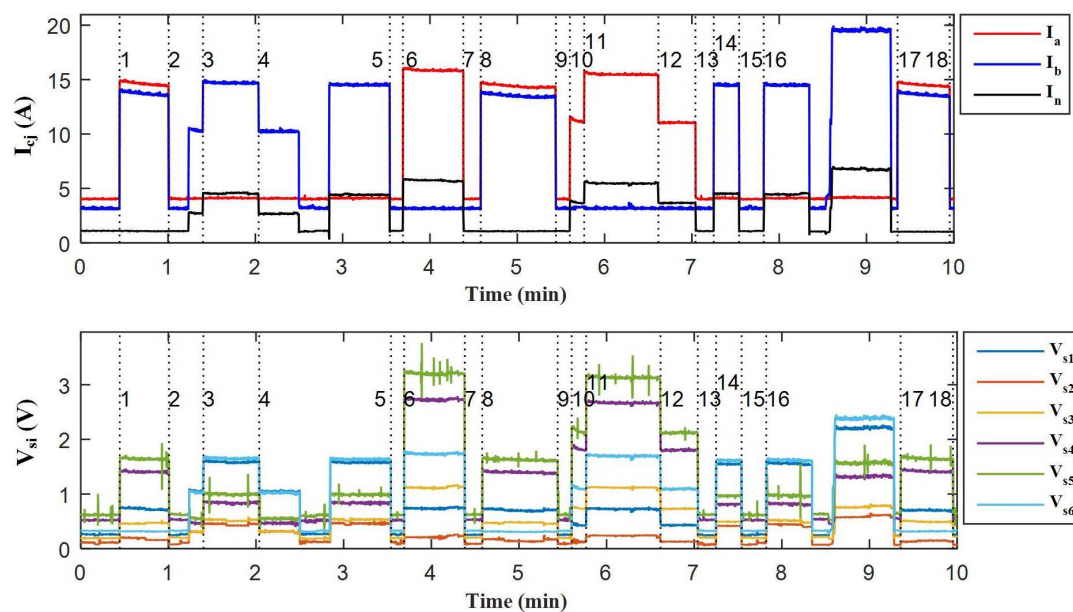
Figure 4.6: Recorded sensor measurements and CT measured currents (10 min).

The changed currents of three representative events (e_7, e_5 and e_1) are shown in Fig, 4.7. We could see that, for the $A - N$ and $B - N$ type events, a large portion (over 50%) of the unbalanced current flows through the ground wire back to the service transformer. The cause of the large ground current is diagnosed using the stray voltage troubleshooting strategy in reference [24]. Since the calculated customer contribution to the NEV is noticeably higher and the K ratio is very small (around 0.4), a bad neutral conductor may be the cause of the large ground current. The corresponding extracted sensor measurement patterns of the representative three events are shown in Fig. 4.8.
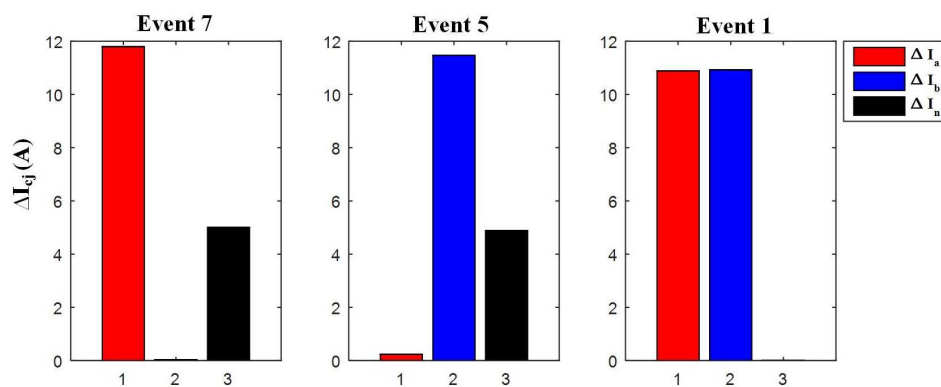
Figure 4.7: Changed currents of different events in field test.
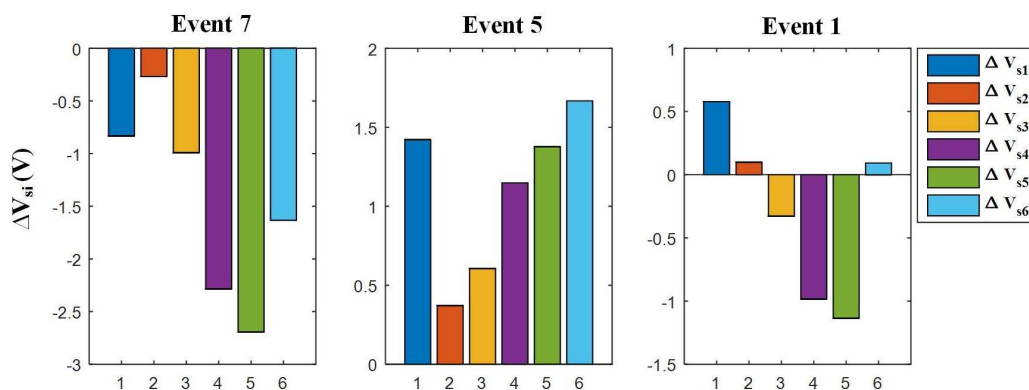
Figure 4.8: Extracted sensor measurement patterns of different events in field test.

The event clustering result using cosine similarity is shown in Fig. 4.9. We could see that the 18 extracted events are cluster into three different groups ($\{e_7, e_6, e_{10}, e_{13}, e_{11}, e_{12}\}$, $\{e_5, e_{15}, e_{16}, e_{14}, e_3, e_4\}$ and $\{e_1, e_8, e_{17}, e_2, e_{18}, e_9\}$). The appliance state changing events of the same type are sorted with the sum of the absolute values of extracted sensor measurements descending so that the events that correspond to appliances with larger power are used to solve the NLLS optimization problem. A total of 12 events, with 4 of each type, i.e., $\{e_7, e_6, e_{10}, e_{13}\}$, $\{e_5, e_{15}, e_{16}, e_{14}\}$ and $\{e_1, e_8, e_{17}, e_2\}$ are used to solve the wire positions. The NLLS parameters are same as ones used at laboratory experiments except that the wire radius limit r_w is set to $3mm$ since most residential houses use service entrance wires with at least size 3 AWG ($5.827mm$ diameter). Based on the proposed method, the wire positions are solved with 2.141 seconds CPU time.
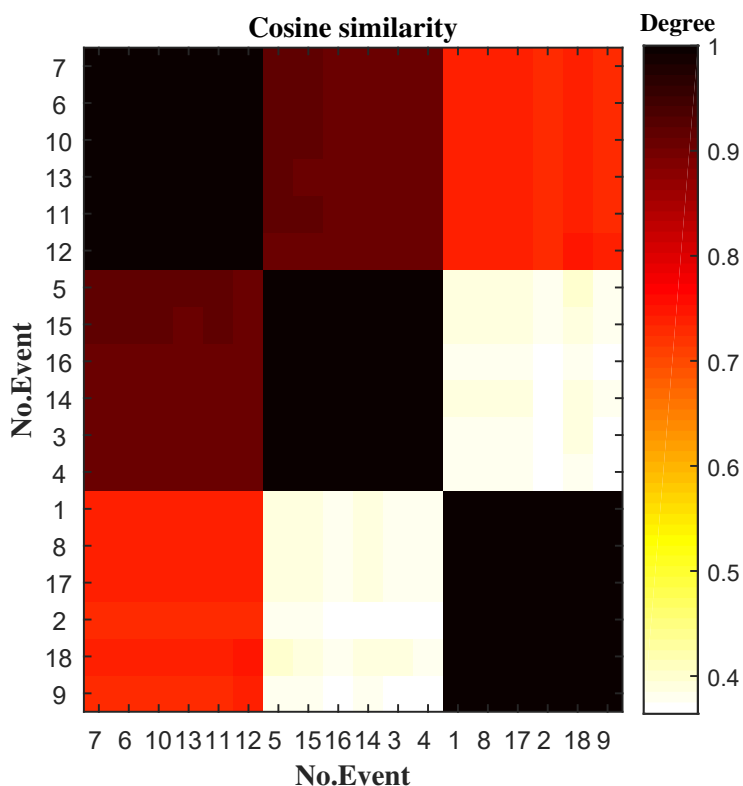
Figure 4.9: Event clustering result of field test.

The identified wire positions are shown in Fig. 4.10. Since the wires are enclosed in the incoming conduit at over head service entrance point, there are no reference wire positions to compare with. The accuracy of currents measured use the trans-impedance matrix built by the solved wires positions will validate the accuracy of solved wire positions indirectly.
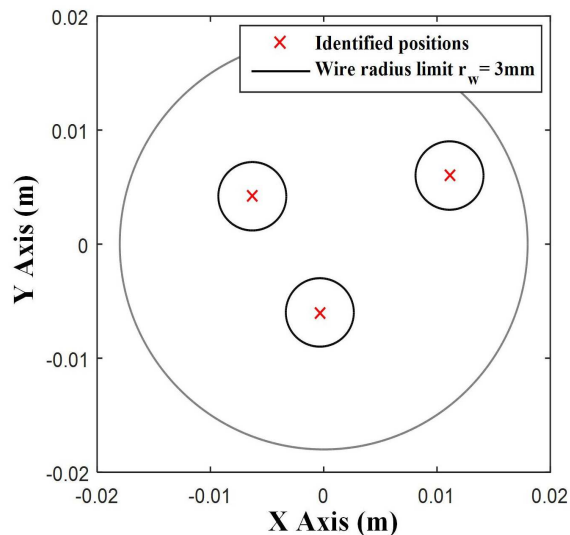
Figure 4.10: Solved wire positions in field test.

After solving the wire positions, the reference currents and sensor measurements data are continuously recorded by two laptops from 6 : 00 p.m. to 8 : 00 p.m. The calculated wire wire currents are compared with the CT measured reference currents as shown in Fig. 4.11. A average of 1 second data is used to present the results. We could see that from around 7 : 00 p.m. to 7 : 30 p.m., I_a and I_b change frequently, which is cause by the stove used in kitchen for cooking. The average relative errors are 0.68%, 2.14% and 6.35% for I_a, I_b and I_n, respectively. The current measurement absolute errors are shown in Fig. 4.12, with average values of $0.032A$, $0.169A$ and $0.073A$ for I_a, I_b and I_n, respectively. Since the currents are measured accurately, the solved wire positions are validated. Based on the field test results, we can conclude that accurate home current measurements can be achieved based on our proposed method.
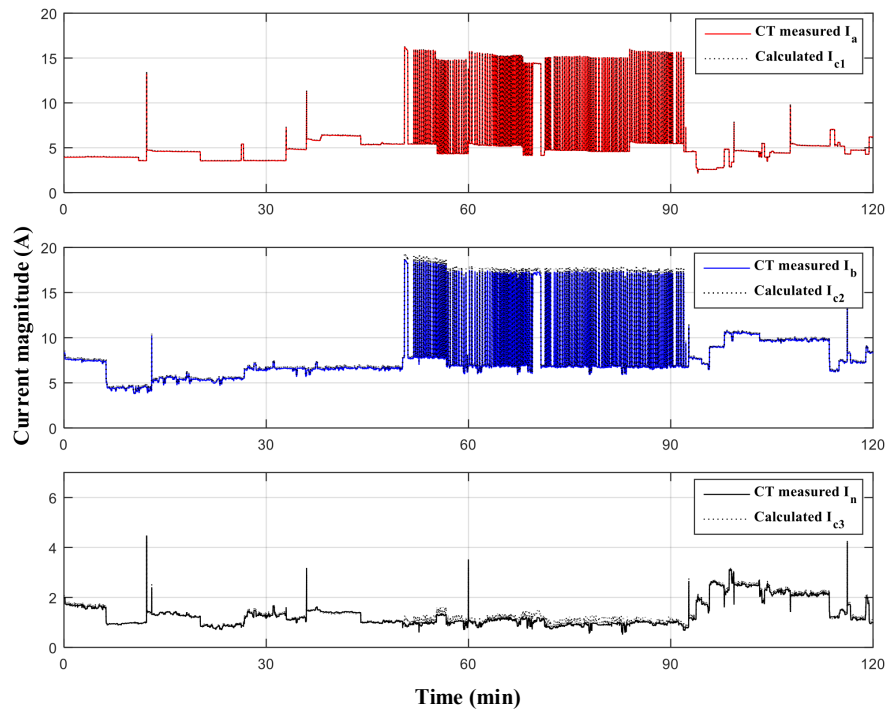
Figure 4.11: Current measurement results of field test.
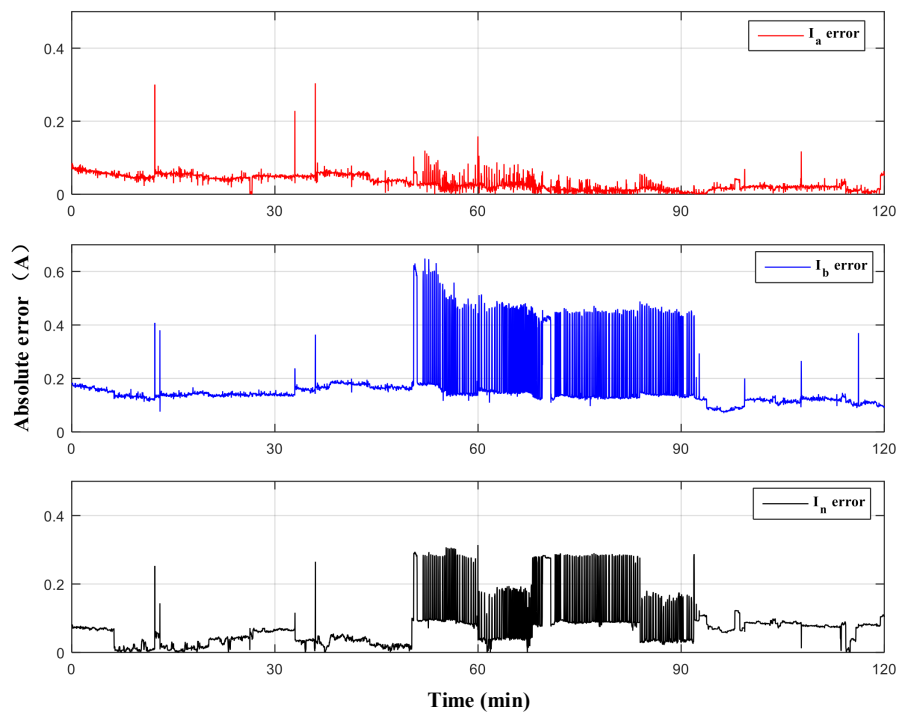
Figure 4.12: Current measurement absolute errors of field test.

4.4 Summary

This chapter presents the laboratory and field test results of the proposed event-based non-intrusive home current measurement method. Two types of conductors are used as wires and tested in Laboratory. The first one uses Aluminum bars inserted in 3D printed wire holders with reference positions as wires to validate the accuracy of solved wire positions from NLLS optimization problem. The second type usescc electric service wires at the incoming conduit of service panel. The grounding wire are connected with the neutral wire at the transformer side and bonded at the service panel to imitating the grounding system of North American homes. The test results show that the measurement accuracy of the two hot wires are within 5% relative errors for most of the cases. Due to smaller magnitude, the neutral wire current is solved with larger but within 8% relative errors. The field test is taken at a residential house in Edmonton, AB, Canada. The sensor measurements are first recorded for 10 minutes and used for event detection, event clustering and solving wire positions. Then the sensor measurement and reference current data is recorded for 2 hours. The wire currents are calculated using the sensor measurement data and trans-impedance matrix built using solved wire positions and compared with the reference currents. The two hot wire currents are solved with average 0.68%, 2.14% and 6.35% for I_a, I_b and I_n, respectively. The extensive laboratory and field test results validated the proposed method. Satisfactory measurement accuracy is achieved.

Chapter 5

Investigations of Underground Service Entrance Point Measurement

5.1 Overview

This chapter presents the studies of the non-intrusive home current measurement using sensor array at the underground service entrance point. As discussed in Subsection 2.2.1, there are two service entrance methods for North American homes including overhead service entrance method and underground service entrance method. The field measurement results of the proposed method at the overhead service entrance point of a residential home are validated and shown in Section 4.3. For underground service entrance method, service entrance cable (USEB cable) commonly consists of two conductors as hot wires and one stranded bare neutral wrapper in insulation cover is most commonly used. The features of USEB service entrance cable are presented in Section 5.2. The laboratory test results of USEB cable is shown in Section 5.3. The large current measurement errors of USEB cable indicate that the magnetic field generated by the neutral strands needs further investigations. Thus, the equivalent conductor models are built and laboratory tests of the USEB cable neutral strands are done as shown in Section 5.4. And Section 5.5 gives the summary of the whole chapter.

5.2 USEB Service Entrance Cable

It is confirmed from a sales manager at EECOL electric store at Edmonton, AB, Canada that USEB cable is the most commonly used cable type for home underground service entrance. The basic configuration of USEB cable is shown in Fig. 5.1. We could see that the USEB cable consists of two Aluminum conductors as hot wires and twisted copper strands closely wrapping the two hot wires as neutral wire. The USEB cable is enclosed in the raceway from the service transformer pad to the service end such as electric meter and when it reached the service end, the neutral strands are twisted into one conductor as shown in Fig. 2.6.
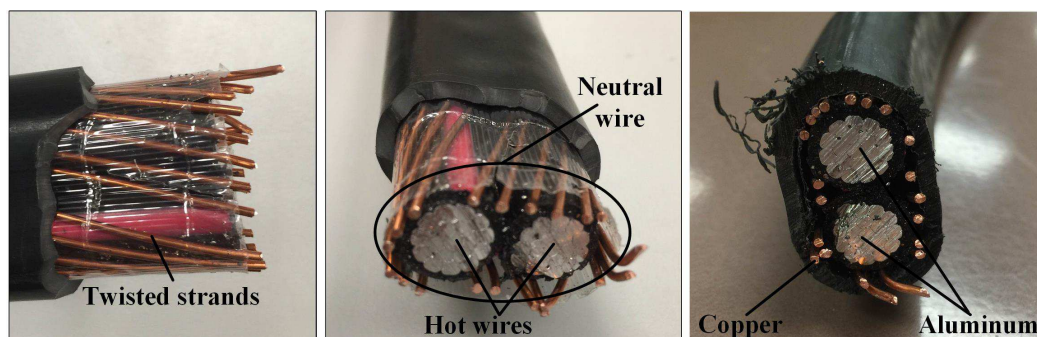
Figure 5.1: USEB cable configuration.

Some clever designs are used to reduce the magnetic field emissions of many equipments that can generate their own magnetic field. One of the methods is to combine two wires with opposite current directions to cancel the magnetic disturbances. The best way is to combine the two wires in a twisted pair as shown in Fig. 5.2. It is found in our previous field tests that the sensor measurement signals at the underground service entrance point are much smaller than the ones measured at overhead service entrance point. The small magnetic field strength generated by the USEB cable can be explained by its own wire configuration. As we can see, the two hot wires with opposite current directions are quite close, which in turn causes severe magnetic field cancellation. Besides, the two hot wires are closely wrapped with the twisted neutral strands, which further cancels the magnetic field emissions although only the neutral strands are twisted.
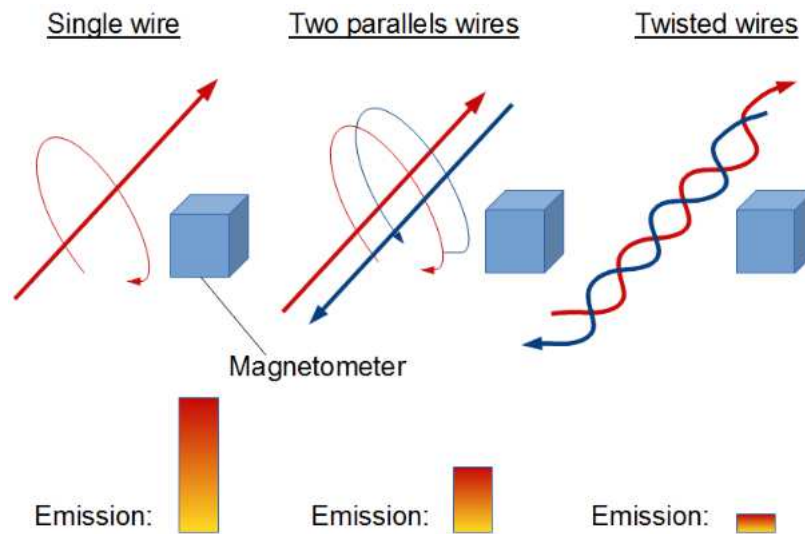
Figure 5.2:   Magnetic field strength of single wire, two parallel wires and twisted wires.

5.3   USEB Cable Laboratory Test

Laboratory test is done to check the measurement accuracy of USEB cable using the proposed method. The USEB cable is energized and connected to the home appliances. The three-phase currents are measured using CTs and the USEB cable is enclosed in the electric conduit. The current and sensor measurement data is recorded for around 15 seconds. The same proposed event-based non-intrusive home current measurement processes including event detection, event clustering, wire position solving and real-time current measurement are used to test the USEB cable. The recorded sensor measurements and CT measured currents of USEB cable are shown in Fig. 5.3. We could see that the sensor measurement values are small (less than 1.5V) due to its configuration. The wire position solving algorithm is used to solve the USEB cable wire positions with the wire radius limit r_w set to 3mm. The solved wire positions of USEB cable are shown in Fig. 5.4. We could see that the solved three wire positions are quite close to each other, which in turn causes magnetic field cancellation. Besides, the three wire positions are solved at the boundaries of the wire radius limit.
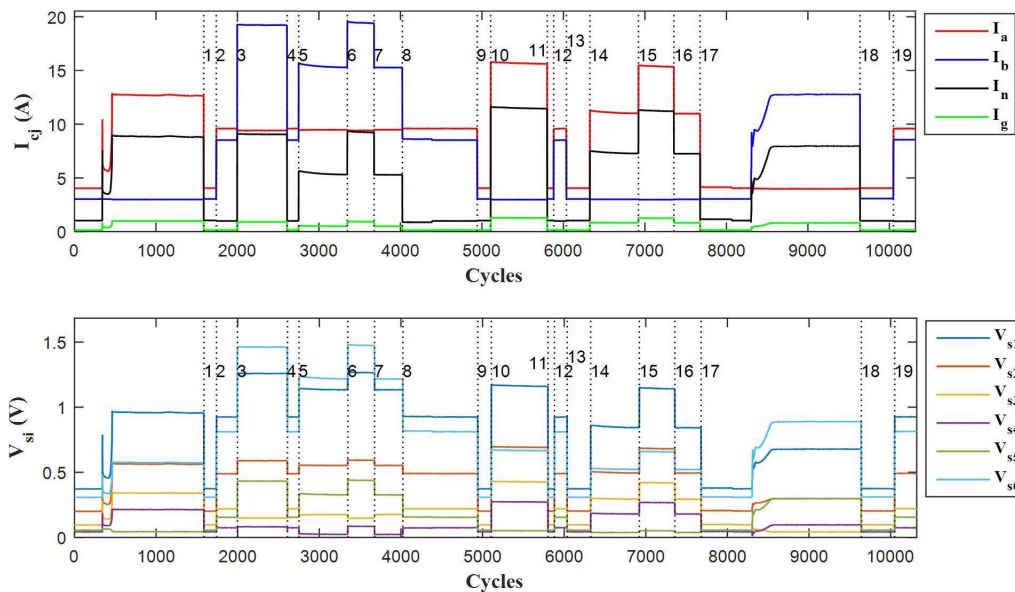
Figure 5.3: Recorded sensor measurements and CT measured currents of USEB cable laboratory test.
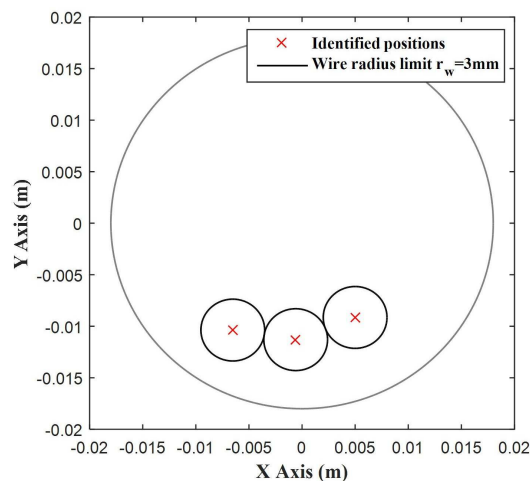
Figure 5.4: Solved wire positions of USEB cable in laboratory test.

The current measurement results of USEB cable laboratory test is shown in Fig. 5.5. The measurement accuracies are 5.28%, 21.71% and 29.86% relative errors and 0.42A, 0.88A and 0.87A absolute errors for I_a, I_b and I_n, respectively. The large measurement errors indicate that the magnetic field generated by the neutral stands needs further investigations.
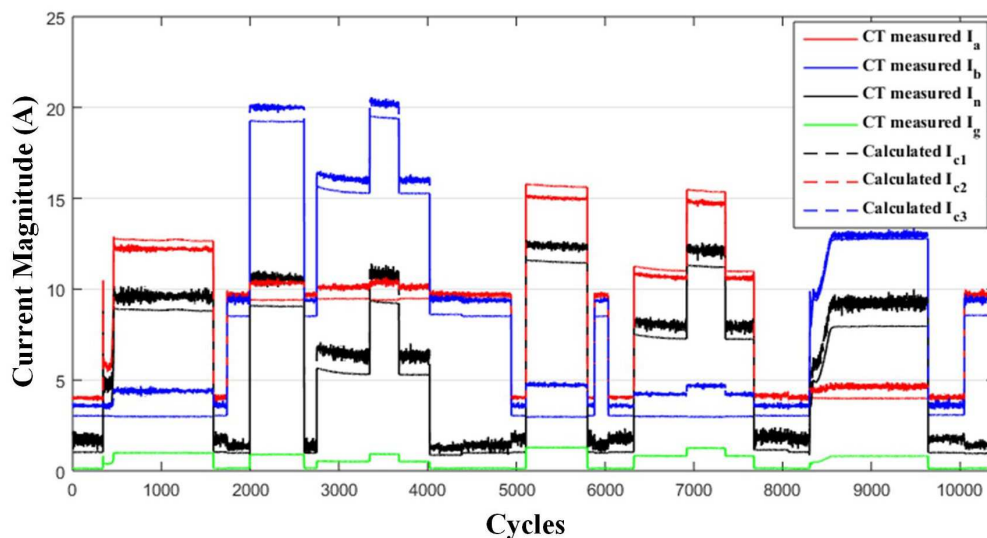
Figure 5.5: Current measurement results of USEB cable laboratory test.

5.4 Neutral Strands Equivalent Model

The measurement results in Section 5.3 shows that the trans-impedance matrix built using the proposed method is not accurate enough. In previous laboratory and field tests, the neutral wire is an isolated single conductor. Since the neutral wire of USEB cable consists of many twisted copper strands, the equivalent model of the neutral wire between sensor measurements and wire currents should be investigated. The trans-impedance matrix $\left[Z_{ij}\right]_{n_s \times 3}$ is built based on biot-savart law, which is valid on a single long and straight current at a point in space as shown in (2.32). The isolated wires can be treated as a single conductor and are validated through extensive laboratory and field tests as show in previous chapters. The two hot wires of the USEB cable are two isolated conductors. Whether the USEB cable neutral strands can be treated as one isolated conductor is investigated first. Then, the equivalent two-conductor model is built and used to fit the magnetic field generated by the USEB cable neutral strands. The equivalent single-conductor and two-conductor models are used to fit the sensor measurements generated only by the neutral strands and tested in laboratory experiments. The solved equivalent current is compared with the CT measured one to check the accuracies of the equivalent models.

5.4.1 Equivalent Single-Conductor Model

Whether the USEB cable neutral strands can be treated as one isolated conductor is investigated first. As shown in Fig. 5.6, the position of neutral strands equivalent single conductor is defined as (x_n, y_n). The calculated sensor measurements V_{bn} of the equivalent single conductor at position (x_n, y_n) with equivalent current I_{ne} is shown in (5.1). The trans-impedance matrix of the equivalent neutral wire $\left[Z_{ni}\right]_{n_s \times 1}$ can be calculated based on the single-conductor model as shown in (5.2) .
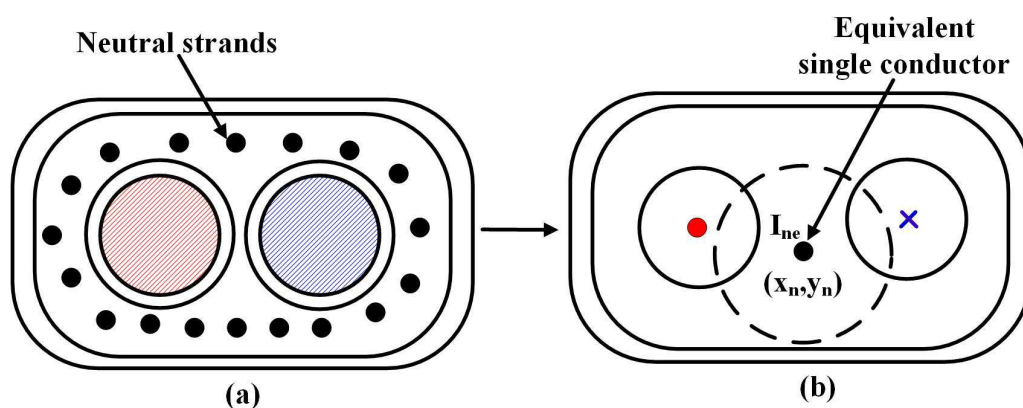
Figure 5.6: (a) USEB cable configuration illustration; (b) Neutral strands equivalent single-conductor model.

$$\left[V_{bni}\right]_{n_s \times 1} = \left[Z_{ni}\right]_{n_s \times 1} \times I_{ne}. \tag{5.1}$$

$$Z_{ni} = g_{si} \frac{\mu_0}{2\pi r_{si}} \frac{p_i \cdot (x_{si} - x_n) + q_i \cdot (y_{si} - y_n)}{(x_{si} - x_n)^2 + (y_{si} - y_n)^2} \quad \forall i \in \mathbb{S}_s. \tag{5.2}$$

where, $p_i = x_{si} \cos \theta_{si} - y_{si} \sin \theta_{si}$, $q_i = y_{si} \cos \theta_{si} + x_{si} \sin \theta_{si}$ and $r_{si} = \sqrt{x_{si}^2 + y_{si}^2}$.

To get the trans-impedance matrix $\left[Z_{ni}\right]_{n_s \times 1}$, the equivalent wire position (x_n, y_n) needs to be solved, and the equivalent current I_{ne} is also unknown. The solving task is modeled as a NLLS optimization problem and solved using NPL algorithm formulated in AMPL with KNITRO as solver. There are a total of 3 unknown variables x_n, y_n and I_{ne} and each measurement we have n_s equations to solve the equation system. In theory, as long as $n_s \geq 3$, the equation system can be solved. The optimization goal is to find the minimum least square value

between sensor measurements V_{sn} and calculated values V_{bn} as shown in (5.3). Some constraints added to achieve better optimization performance are the equivalent single-conductor model (5.4), maximum limit of calculated sensor measurement values (5.5), physical limit of wire position (5.6) and maximum limit of calculated neutral current (5.7). The NLLS parameters are shown in Table 3.2 except that the wire radius limit r_w changes for different wire types. If the solved equivalent current I_{ne} is accurate comparing with the CT measured neutral current I_n, the single-conductor model is fit for the USEB cable neutral strands.

$$\min \sum\nolimits_{i \in \mathbb{S}_S} \left(V_{sni} - V_{bni} \right)^2 \tag{5.3}$$

$$\text{s.t.} \begin{cases} \forall i \in \mathbb{S}_s & \begin{cases} V_{bni} = Z_{ni} \times I_{ne} & \text{(5.4)} \\ |V_{bni}| \leq V_{op} & \text{(5.5)} \end{cases} \\ \sqrt{(x_n)^2 + (y_n)^2} \leq r_c - r_w & \text{(5.6)} \\ |I_{ne}| \leq I_{max}. & \text{(5.7)} \end{cases}$$

5.4.2 Experiment Results of Single-Conductor Model

The solving algorithm based on single-conductor model is validated using Aluminum bar as wire first. The Aluminum bar is inserted into the 3D printed wire holder with reference positions and energized with single current around $11A$ (I_n). The sensor measurements are recorded in several seconds and the average 60 Hz components are used as input V_{sn} of the solving algorithm. The wire radius limit r_w is set to $1.8mm$ since the Aluminum bar is used as wire. A total of 10 cases with the Aluminum bar at different reference positions are measured. The solved wire positions are compared with the reference positions of the wire holder as shown in Fig. 5.7.

The solved equivalent wire currents (I_{ne}) and positions (x_n, y_n) of the 10 cases are compared with the reference currents measured by CT (I_n) and the reference positions of the 3D printed wire holder. The relative errors of the solved currents and the position differences between the solved wire positions and the reference ones are show in Table 5.1. We could see that the solved

currents of all cases are within 0.6% relative errors and the wire position differences are within 0.25 mm. Therefore, the single-conductor model solving algorithm is validated through the laboratory Aluminum bar test.
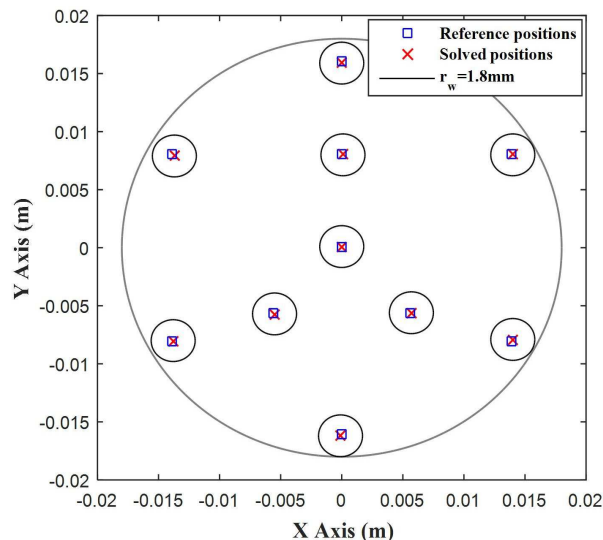
Figure 5.7: Single-conductor model solving algorithm validation using Aluminum bars.

Table 5.1: Solved currents and wire positions errors of Aluminum bar single-conductor model solving algorithm laboratory test.

Cases	1	2	3	4	5	6	7	8	9	10
Relative Error %	-0.57	-0.07	-0.30	0.11	-0.29	0.17	0.40	-0.15	-0.04	-0.37
Position Error mm	0.18	0.10	0.10	0.06	0.14	0.19	0.22	0.10	0.16	0.07

Then, the USEB neutral wire is energized with single current around $11A$ (I_n) and the other two hot wires are unenergized. The sensor measurements are recorded for several seconds and the average 60 Hz components are used as input V_{sn} of the solving algorithm. The same parameters of NLLS are used to solve the equivalent wire positions except that the wire radius limit is set to $8mm$ since each hot wire is at least $5.827mm$ diameter and there is an insulation cover for each hot wire. A total of 16 cases are measured with the USEB cable either rotated or moved.

The solved current errors of the 16 cases of USEB cable neutral strands laboratory test using single-conductor model solving algorithm is shown in Table 5.2. We could see that the solve current relative errors could reach around 5% while all the current relative errors of Aluminum bar test are within 0.6%. Considering the sensor measurements used to solve the wire currents are generated by three wires, a more accurate equivalent model of the USEB neutral strands is needed to achieve better measurement accuracy.

Table 5.2: Solved current errors of USEB cable neutral strands single-conductor model solving algorithm laboratory test.

Cases	1	2	3	4	5	6	7	8
Relative Error %	2.28	2.44	1.36	-2.58	-1.80	0.02	-2.45	-4.53
Cases	9	10	11	12	13	14	15	16
Relative Error %	-1.62	0.36	1.68	-0.55	1.89	0.05	-3.99	0.07

5.4.3 Equivalent Two-Conductor Model

The equivalent single-conductor model of USEB cable neutral strands is shown in (5.1). Using more than one conductor to build the equivalent model of USEB cable neutral stands, the calculated sensor measurements V_{bn} is shown in (5.8). The equivalent conductors (x_{nj}, y_{nj}) are denoted as $\mathbb{S}_n$ with number of equivalent single conductors n_n and the equivalent currents are denoted as I_{nej} as shown in Fig. 5.8.

$$\left[V_{bni}\right]_{n_s \times 1} = \sum_{j \in \mathbb{S}_n} \left[Z_{ni,j}\right]_{n_s \times 1} \times I_{nej}. \tag{5.8}$$

The equivalent neutral current I_{ne} is then the sum of the currents of equivalent conductors I_{nej} as shown in (5.9).

$$I_{ne} = \sum_{j \in \mathbb{S}_n} I_{nej}. \tag{5.9}$$

The elements $Z_{ni,j}$ of trans-impedance matrix $\left[Z_{ni,j}\right]_{n_s \times 1}$ is shown in (5.10).
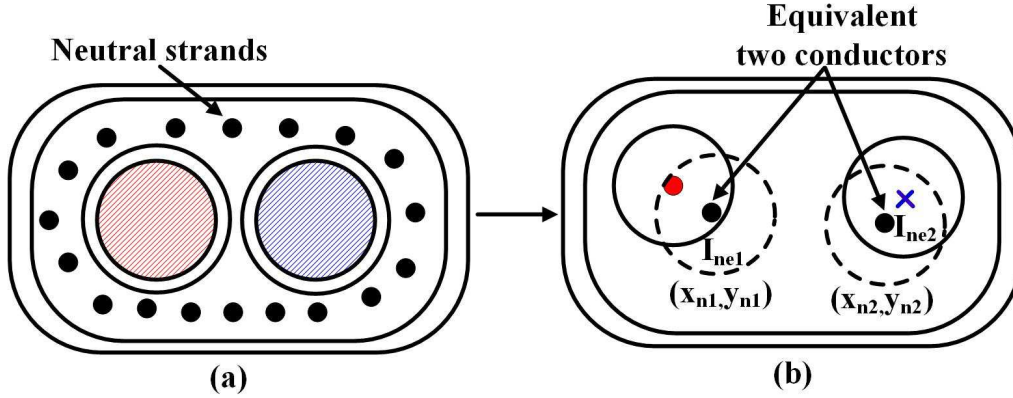
Figure 5.8: (a) USEB cable configuration illustration; (b) Neutral strands equivalent two-conductor model.

$$Z_{ni,j} = g_{si} \frac{\mu_0}{2\pi r_{si}} \frac{p_i \cdot (x_{si} - x_{nj}) + q_i \cdot (y_{si} - y_{nj})}{(x_{si} - x_{nj})^2 + (y_{si} - y_{nj})^2} \quad \forall i \in \mathbb{S}_s, \forall j \in \mathbb{S}_n. \quad (5.10)$$

where, $p_i = x_{si} \cos \theta_{si} - y_{si} \sin \theta_{si}$, $q_i = y_{si} \cos \theta_{si} + x_{si} \sin \theta_{si}$ and $r_{si} = \sqrt{x_{si}^2 + y_{si}^2}$.

Comparing (5.8) with (5.1), we could see that the trans-impedance matrix $\left[Z_{ni} \right]_{n_s \times 1}$ between calculated sensor measurements and equivalent neutral current I_{ne} is the sum of trans-impedance matrix $\left[Z_{ni,j} \right]_{n_s \times 1}$ of equivalent single conductors as shown in (5.11). However, if the currents of equivalent single conductors are not equal, a gain factor $\dfrac{I_{nej}}{I_{ne}}$ is needed.

$$\left[Z_{ni} \right]_{n_s \times 1} = \sum_{j \in \mathbb{S}_n} \begin{cases} \left[Z_{ni,j} \right]_{n_s \times 1}, & if I_{nej_1} = I_{nej_2}, \forall j_1, j_2 \in \mathbb{S}_n, j_1 \neq j_2 \\ \left[Z_{ni,j} \right]_{n_s \times 1} \times \dfrac{I_{nej}}{I_{ne}}, & if I_{nej_1} \neq I_{nej_2}, \forall j_1, j_2 \in \mathbb{S}_n, j_1 \neq j_2 \end{cases}$$
$$(5.11)$$

Therefore, if we use equivalent two-conductor model ($n_n = 2$) to solve the equivalent conductor positions and currents of the USEB cable neutral strands, we need at least five sensors since there are four unknown geometrical variables $(x_{n1}, y_{n1}, x_{n2}, y_{n2})$ and one unknown current variable if the two equivalent currents are equal ($I_{nej1} = I_{nej2}$). If the two equivalent currents are no equal, i.e., $I_{nej1} \neq I_{nej2}$, at least six sensors are needed to solve the equivalent positions and currents. Further increase the number of equivalent conductors will add

two unknown position variables each, which will in turn increase the solving algorithm computational complexity and the number of sensors. Thus, only the equivalent two-conductor model is tested in laboratory experiment.

The solving task of the USEB cable neutral strands equivalent conductor positions and currents is modeled as a NLLS optimization problem and solved using NPL algorithm formulated in AMPL with KNITRO as solver. The optimization goal is to find the minimum least square value between sensor measurements V_{sn} and calculated values V_{bn} as shown in (5.12). The calculated V_{bni} is the sum of the calculated sensor measurements of all equivalent conductors as shown in (5.13). The calculated sensor measurement magnitudes are limited within the operational circuit output maximum voltage as shown in (5.14). The positions of every equivalent conductors are limited in the electric conduit as shown in (5.15) and the equivalent currents are limited within the maximum home appliance current as shown in (5.16). The positions of equivalent conductors are not overlapped with each other as shown in (5.17). Since the USEB cable is symmetrical, it is reasonable to take the two equivalent currents as equal when we use the two-conductor equivalent model. The currents of the two equivalent conductors ($n_n = 2$) are equal in magnitudes for simplification as shown in (5.18).

$$\min \sum_{i \in \mathbb{S}_S} \left(V_{sni} - V_{bni} \right)^2 \tag{5.12}$$

$$\text{s.t.} \begin{cases} \forall i \in \mathbb{S}_s & \begin{cases} V_{bni} = \sum_{j \in \mathbb{S}_n} Z_{ni,j} \times I_{nej} & \text{(5.13)} \\ |V_{bni}| \leq V_{op} & \text{(5.14)} \end{cases} \\ \forall j \in \mathbb{S}_n & \begin{cases} \sqrt{(x_{nj})^2 + (y_{nj})^2} \leq r_c - r_w & \text{(5.15)} \\ |I_{nej}| \leq I_{max} & \text{(5.16)} \end{cases} \\ \forall j_1, j_2 \in \mathbb{S}_n, j_1 \neq j_2 & \begin{cases} \sqrt{(x_{nj_1} - x_{nj_2})^2 + (y_{nj_1} - y_{nj_2})^2} \geq 2r_w & \text{(5.17)} \\ I_{nej_1} = I_{nej_2} & \text{(5.18)} \end{cases} \end{cases}$$

5.4.4   Experiment Results of Two-Conductor Model

Laboratory experiments are done to test the accuracy of USEB neutral strands equivalent two-conductor model[1]. The sensor measurements v_{sn} (six sensors) correspond only with the neutral stands are recorded for several seconds the average value of the 60 Hz components are used as input to solve the NLLS optimization problem. To further test the model accuracy, the current flows through the neutral strands is increased from $1.4A$ to $11.2A$ using resistive box and the USEB cable is placed at three different positions as three measurement cases. The solved equivalent current I_{ne} is compared with the CT measured reference current I_n to check the two-conductor model accuracy.

The solved equivalent conductor positions of the 3 cases are shown in Fig. 5.9, 5.10 and 5.11, respectively. Both single-conductor and two-conductor models are used to solve the equivalent positions and the solved equivalent current I_{ne} accuracies are compared. The USEB cable neutral strands equivalent single-conductor wire position is solved with wire radius limit set to $8mm$, while r_w is set to $3mm$ when two-conductor model is used. The solved equivalent conductor positions using sensor measurements generated by the neutral strands at different current levels are all shown in the same figure. We could see that the solve equivalent conductor positions are almost the same at different current levels.

(a)   (b)
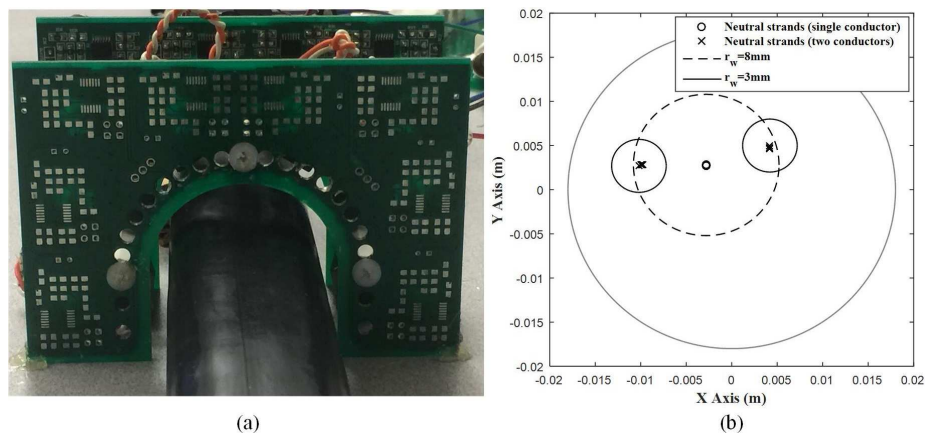
Figure 5.9: USEB cable laboratory experiment Case 1: (a) USEB cable position; (b) Solved reference wire positions.

---

[1]The algorithm validation using Aluminum bars is not done since the USEB neutral two-conductor model test could reach within 1.5% accuracy
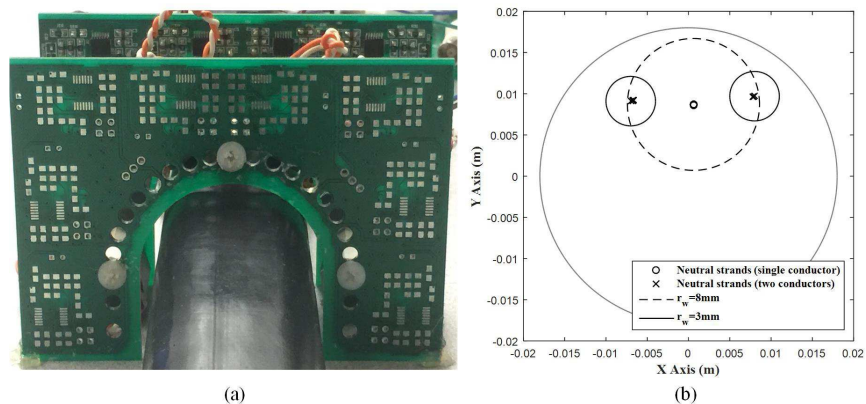
Figure 5.10: USEB cable laboratory experiment Case 2: (a) USEB cable position; (b) Solved reference wire positions.
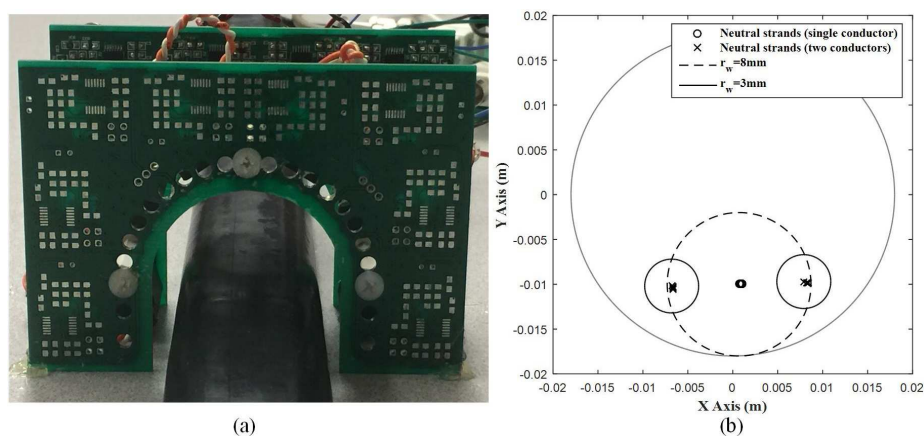
Figure 5.11: USEB cable laboratory experiment Case 3: (a) USEB cable position; (b) Solved reference wire positions.

The solved equivalent neutral currents (I_{ne}) of USEB cable using the equivalent models are compared with the CT measured currents (I_n) and the relative errors are calculated and shown in Table 5.3. We could see that the equivalent two-conductor model achieves better measurement accuracy for the neutral strands than the single-conductor model within 1.5% relative error for all the three cases. The current measurement accuracy of the neutral strands using two-conductor model are at the same level as the Aluminum bar test as shown in Table 5.1.

Table 5.3: Current measurement relative errors of USEB cable equivalent model.

Cases	Wires	Current magnitude				
		1.4A	2.8A	5.6A	8.4A	11.2A
1	Nuetrual - single conductor	0.79	0.88	1.30	1.65	1.93
1	Nuetrual - two conductors	−1.26	−1.12	−0.68	−0.33	−0.05
2	Neutral - single conductor	2.28	2.46	2.94	3.32	3.59
2	Neutral - two conductors	−1.11	−0.81	−0.32	0.07	0.33
3	Neutral - single conductor	0.73	0.83	1.2	1.53	1.79
3	Neutral - two conductors	−1.32	−1.10	−0.68	−0.27	0.03

Table 5.4 shows the model accuracy versus the neutral current measurement accuracy of three different tests. The wire positions solving algorithm of single-conductor model is validated using Aluminum bar within around 0.5% accuracy as shown in Table 5.1. Laboratory experiment results using Aluminum bars show that the neutral current is measured around 5% and 0.2A relative and absolute errors in Table 4.1. The accuracy of USEB neutral single-conductor model could reach around 4% as shown in Table 5.2. The USEB cable neutral current is measured with around 30% relative error and 1A absolute error using single-conductor model as shown in Section 5.3. The accuracy of USEB neutral two-conductor model is within 1.5% as shown in Table 5.3. The USEB cable current measurement results using two-conductor model is unavailable. We could see from Table 5.4 that the current measurement accuracy is quite sensitive to the model accuracy. To achieve accurate USEB cable current measurement, more accurate model of the neutral strands is needed.

Table 5.4: Model accuracy versus neutral current measurement accuracy.

Tests	Model accuracy	Relative error	Absolute error
Aluminum bar single-conductor model	0.5%	5%	0.2 A
USEB neutral single-conductor model	4%	30%	1 A
USEB neutral two-conductor model	1.5%	NAN	NAN

5.5 Summary

This chapter presents the studies of non-intrusive home current measurement using sensor array at the underground service entrance point. The USEB cable is the most commonly used wiring method at North American home underground service entrance. The USEB cable configuration with two isolated hot wires closely placed in parallel and a number of neutral strands wrap the hot wires can cancel the magnetic field strengths, which in turn cause the sensor measurement magnitudes small. To achieve accurate current measurement of the USEB cable, the trans-impedance matrix built using the wire physical positions between the sensor measurements and wire currents needs to be determined accurately. The two isolated wires of the USEB cable can be treated as two separate conductors same as previous tests. However, an accurate equivalent model of the USEB cable neutral strands is needed to achieve accurate current measurement. The equivalent single-conductor and two-conductor models are built to fit the sensor measurements generated by the neutral strands. Laboratory experiments are done to check the accuracy of the equivalent models. The USEB cable neutral is energized with single current and the sensor measurements correspond only with the neutral strands are recorded and used to solve the equivalent conductor positions. The single-conductor and two-conductor models are both used for the USEB neutral strands and the two-conductor model has better measurement accuracy within 1.5% relative errors at all current levels. Since the current measurement accuracy is quite sensitive to the model accuracy, more accurate equivalent model of the USEB cable neutral strands is needed.

Chapter 6

Conclusion and Future Work

6.1 Thesis Conclusions and Contributions

This thesis presents the studies of non-intrusive current measurement using sensor array in North American homes. The major conclusions and contributions of this thesis are summarized as follows:

- An overview is made to summarize the existing current sensing technologies. The technical challenges of non-intrusive current measurement especially in multi-wire system are discussed. The overview lays the foundation for the research presented in this thesis, which is to measure the North American home currents using sensor array non-intrusively, effectively and accurately.

- The North American home power supply system including service entrance methods, service panel, home appliance wiring and grounding are investigated and modeled. The home grounding current and neutral-ground bond at the service panel, which may lead to NEV problem are further investigated using measured residential current data. A smart, low-cost, user-friendly and easy-to-implement sensing device is designed and implemented. The mathematical models of sensed magnetic field generated by single-wire and multi-wire systems are built. The wire currents can be calculated by decoupling the mixed magnetic field using the solved wire positions.

- A novel event-based non-intrusive home current measurement method using sensor array is proposed. The key idea is to extract information from appliance state changing events captured by sensor measurement changes. The event detection method could extract stable, large and quick appliance state changing events. The events are clustered according to the wire connections using cosine similarity since each detected event only corresponds to two wires between which the appliance is connected. Wire position identification is formulated as a NLLS problem, which is effectively solved by the state-of-the-art NLP algorithm. Extensive mathematical analysis and experimental results show that, six sensors are sufficient for the proposed method without any other supplementary devices.

- Laboratory and field tests are done to validate the proposed event-based non-intrusive home current measurement method. Laboratory experiment using Aluminum bars as wires inserted in a 3D printed wire holders with reference positions validates the wire position solving algorithm. The current measurement accuracies of the two hot wires in Aluminum bar and service wire tests are within 5% relative errors and the neutral current is measured within 8% relative error due to small magnitude. Field test with the sensing device installed at the overhead service entrance point shows satisfactory measurement accuracy has been achieved with the relative errors of the three wires 0.68%, 2.14% and 6.35%, respectively.

- The underground service entrance point current measurement is studied. The USEB cable with special configuration can cancel the magnetic field emission severely, which coincide with our previous field test results. The equivalent single-conductor and two-conductor models are built to solve the equivalent wire positions of the USEB cable neutral strands. Laboratory experiments show that the two-conductor model fits the sensor measurements better.

6.2   Suggestions for Future Work

This thesis work can be extended in the following aspects:

- A more stable machinery structure of the sensing device can be designed to fix the device better. A solar cell or other power methods can be used to replace the storage battery used to power the device to make the device self-sufficient. The sensor measurement signals can be transfered wirelessly using a communication device to replace the NI DAQ instrument. Smaller coil sensors with same measurement accuracy level can be used to further reduce the size of the device.

- More studies of the USEB neutral strands generated magnetic field and strands are suggested. The wire positions of the USEB cable are quite close to each other, which in turn causes severe magnetic field cancellation and brings difficulty in solving the wire positions and magnetic field decoupling. To measure the USEB cable wire currents, the neutral strands equivalent model should be accurate and simple. A too complicated neutral strands model will make the wire position solving algorithm with high computational complexity and the number of sensors large.

- How to reduce the static and dynamic magnetic field interferences to the sensing device when it is placed at a environment with background magnetic field requires more investigations and tests.

- The applications of the sensing device to other types of conduits and cables.

Bibliography

[1] M. R. Alam, M. B. I. Reaz, and M. A. M. Ali, "A review of smart homes – past, present, and future," *IEEE Trans. Syst. Man Cybern. Part B Cybern.*, vol. 42, no. 6, pp. 1190–1203, Nov. 2012.

[2] J. Sharood, G. Bailey, D. Carr, J. Turner and D. Peachey "Appliance retrofit monitoring device with a memory storing an electronic signature," US Patent 6 934 862, Aug. 2005.

[3] Z. Wang and G. Zheng, "Residential appliances identification and monitoring by a nonintrusive method," *IEEE Trans. Smart Grid*, vol. 3, no. 1, pp. 80–92, Mar. 2012.

[4] M. Erol-Kantarci and H. T. Mouftah, "Wireless sensor networks for cost-efficient residential energy management in the smart grid," *IEEE Trans. Smart Grid*, vol. 2, no. 2, pp. 314–325, June 2011.

[5] Z. Chen, L. Wu, and Y. Fu, "Real-time price-based demand response management for residential appliances via stochastic optimization and robust optimization," *IEEE Trans. Smart Grid*, vol. 3, no. 4, pp. 1822–1831, Dec. 2012.

[6] S. Ziegler, R. Woodward, H. -C. Iu and L. Borle, "Current Sensing Techniques: A Review," *IEEE Trans. Sensors J.*, vol. 9, no. 4, pp. 354–376, April 2009.

[7] J. Libove and J. Singer, "Apparatus for measuring voltages and currents using non-contacting sensors," US Patent 5 473 244, Dec. 1995.

[8] X. Sun, Q. Huang, Y. Hou, L. Jiang and P. W. T. Pong, "Noncontact operation-state monitoring technology based on magnetic-field sensing

for overhead high-voltage transmission lines," *IEEE Trans. Power Del.*, vol. 28, no. 4, pp. 2145–2153, Oct. 2013.

[9] J. Lenz and S. Edelstein, "Magnetic sensors and their applications," *IEEE Trans. Sensors. J.*, vol. 6, no. 3, pp. 631–649, June 2006.

[10] J. Bull and N. Jaeger and F. Rahmatian, "A new hybrid current sensor for high-voltage applications," *IEEE Trans. Power Del.*, vol. 20, no. 1, pp. 32–38, Jan. 2005.

[11] K. Draxler, R. Styblikova, J. Hlavacek and R. Prochazka, "Calibration of rogowski coils with an integrator at high currents," *IEEE Trans. Instrum. Mea.*, vol. 60, no. 7, pp. 2434–2438, July. 2011.

[12] K. -L. Chen and N. Chen, "A new method for power current measurement using a coreless hall effect current transformer," *IEEE Trans. Instrum. Meas.*, vol. 60, no. 1, pp. 158–169, Jan. 2011.

[13] C. -T. Liang, K. -L. Chen, Y. -P. Tsai and N. Chen, "New electronic current transformer with a self-Contained power supply," *IEEE Trans. Power Del.*, vol. 30, no. 1, pp. 184–192, Feb. 2015.

[14] G. D'Antona, L. Di Rienzo, R. Ottoboni and A. Manara, "Processing magnetic sensor array data for AC current measurement in multiconductor systems," *IEEE Trans. Instrum. Meas.*, vol. 50, no. 5, pp. 1289–1295, Oct. 2001.

[15] E. Olson and R. Lorenz, "Effective use of miniature multipoint field-based current sensors without magnetic cores," *IEEE Trans. Ind. Appl.*, vol. 46, no. 2, pp. 901–909, Mar. 2010.

[16] J. Zhang, Y. Wen, and P. Li, "Nonintrusive current sensor for the two-wire power cords," *IEEE Trans. Magn.*, vol. 51, no. 11, pp. 1–4, Nov. 2015.

[17] M. Bourkeb, C. Joubert, R. Scorretti, O. Ondel, H. Yahoui, L. Morel, L. Duvillaret, C. Kern, and G. Schmitt, "Device for measuring currents in the conductors of a sheathed cable of a polyphase network," WO Patent 2013 068 360 A1, May 2013.

[18] AVO International Limited, "Megger FlexiClamp 200 User Guide," [Online]. Available: http://www.biddlemegger.com/biddle-ug/ Flexiclamp 200 UG.pdf.

[19] L. Meng, P. Gao, M. Haji, and W. Xu, "Magnetic sensor array-based ac current measurement for multiconductor cables using evolutionary computation method," *IEEE Trans. Instrum. Meas.*, vol. 64, no. 10, pp. 2747–2758, Oct. 2015.

[20] P. Gao, S. Lin, and W. Xu, "A novel current sensor for home energy use monitoring," *IEEE Trans. Smart Grid*, vol. 5, no. 4, pp. 2021–2028, July 2014.

[21] L. Di Rienzo and Z. Zhang, "Spatial harmonic expansion for use with magnetic sensor arrays," *IEEE Trans. Magn.*, vol. 46, no. 1, pp. 53-58, Jan. 2010.

[22] M. Earley, J. Sargent "National electrical code," National fire protection association, 2011 Edition.

[23] H. Holzman, "Morden residential wiring," 9th Edition, 2011.

[24] W. Xu, J.R. Acharya, R. Torquato, and J. Yong "A method to determine stray voltage sources – Part I: Concept and theory," *IEEE Trans. Power Del.*, vol. 30, no. 2, April 2015.

[25] R. Torquato, J.R. Acharya and W. Xu "A method to determine stray voltage sources – Part II: Verification and applications," *IEEE Trans. Power Del.*, vol.30, no. 2, April 2015.

[26] R. Fourer, D. M. Gay, and B. W. Kernighan. *AMPL: A Modeling Language for Mathematical Programming*. Cengage Learning, 2002.

[27] Z. Wang and G. Zheng, "Residential appliances identification and monitoring by a nonintrusive method," *IEEE Trans. Smart Grid*, vol. 3, no. 1, pp. 80–92, Mar. 2012.

[28] R. Fourer, D. M. Gay, and B. W. Kernighan. *AMPL: A Modeling Language for Mathematical Programming*. Cengage Learning, 2002.